

SIGNAL FROM NOISE: INSIGHTS INTO VOLCANIC SYSTEM PROCESSES
FROM AMBIENT NOISE CORRELATIONS

Sara Hanson-Hedgecock

A dissertation submitted to the faculty of the University of North Carolina at Chapel Hill in partial fulfillment of the requirements for the degree of Doctor of Philosophy in the Department of Geological Sciences.

Chapel Hill

2013

Approved by

Dr. Jonathan Lees (Committee Chair)

Dr. Drew Coleman

Dr. José Rial

Dr. Kevin Stewart

Dr. Gordana Vlahovic

ABSTRACT

SARA HANSON-HEDGECOCK: Signal From Noise: Insights Into Volcanic System
Processes From Ambient Noise Correlations
(Under the direction of Jonathan Lees)

This first section of dissertation concerns the imaging of the crust and upper most mantle structure of the mid-Miocene volcanic provinces of the Northwestern United States using ambient noise tomography. Chapter 1 introduces the complex tectonic history of the northwestern United States and describes the development of volcanism from the ignimbrite sweep that occurred with the extension of the Basin and Range province, initiation and evolution of the mid-Miocene volcanism of the Steens/Columbia River flood basalts, and mirror-image volcanic tracks of the High Lava Plains, Oregon and Yellowstone-Snake River Plains. Chapter 2 describes in detail the concepts and methods for determining the 3D shear velocity structure in the crust and uppermost mantle from ambient noise correlations. Chapter 3 contains the text and supplementary materials of Hanson-Hedgecock *et al.* [2012] published in the Geophysical Research Letters that describes the application of the ambient noise methods to the imaging of the Western United States.

The second section of this work discusses the results of measuring velocity changes associated with three episodes of increased eruptive activity at Tungurahua in 2010 using ambient noise correlations. The third section of this work discusses the results of using the H/V ratio to measure the level of equipartition of the ambient noise wavefield at Tungurahua in 2010.

ACKNOWLEDGEMENTS

I would like to thank Hiroyuki Kumagai for establishing the Japanese JICA program as well as the authorities and staff of the Instituto Geofísico Escuela Politécnica Nacional (IGEPN) for sharing data and providing support. I also wish to thank Dr. Lees for his teaching, guidance, patient understanding, and encouragement during my time as a graduate student. I would not be finishing my dissertation without his advice, support and coaching. Many thanks are given to my committee for their forbearance and to my friends and family whose friendly encouragement was invaluable during this undertaking. Saving the best for last, I wanted to thank my Mother whose great support and guidance knows no bounds.

TABLE OF CONTENTS

Abstract	ii
Acknowledgements.....	iii
List of Figures	ix
List of Tables.....	xvi
Chapter 1	1
Tectonics and Volcanism in the Western United States.....	1
1.1. Introduction	1
1.2. Tectonic Setting	1
1.3. Volcanism in the Northwestern United States	5
1.4. High Lava Plains, Oregon (HLP)	6
1.5. Yellowstone-Snake River Plains (YSRP)	8
1.6. Problem Statement	9
Chapter 2	11
Methods	11
2. Methods	11
2.1. Background: Obtaining the empirical Green's function from diffuse field correlations theory	12
2.2. Background: Applications to seismic noise	15
2.3. Methods: Data	16
2.4. Methods: Processing ambient noise records to obtain the empirical Green's function (EGF).....	17

2.5.	Methods: Determination of phase velocities from EGFs	21
2.6.	Methods: Fundamental mode Raleigh wave maps from ambient noise tomography.....	22
2.7.	Inversion for Shear Velocity and Shear Model Parameterization.....	23
2.8.	Dispersion misfit	25
2.9.	Shear wave velocity model uncertainty.....	26
Chapter 3		27
3.	Abstract	27
3.1.	Introduction	28
3.2.	Data and Methods	29
3.3.	Phase velocity models from ambient noise tomography	30
3.4.	Shear wave velocity model.....	30
3.5.	Results and Discussion	31
3.6.	Owyhee Plateau Anomaly	31
3.7.	High velocity mid-crustal anomaly beneath the SRP	32
3.8.	Low velocities in the lower crust beneath Yellowstone	34
3.9.	High Lava Plains low velocity zone.....	34
3.10.	Acknowledgements.....	35
3.11.	References	36
3.12.	Figures, Hanson-Hedgecock <i>et al.</i> , 2011	39
3.13.	Auxiliary Materials for Constraints on the causes of the mid- Miocene volcanism in the Pacific Northwest US from ambient noise tomography.....	42
3.14.	Introduction:	42
3.15.	Text S1 Methods:	43

3.16.	S1.1 Inversion for Shear Velocity and Shear Model Parameterization.....	43
3.17.	S1.1.2 Dispersion misfit.....	44
3.18.	S1.1.3 Shear wave velocity model uncertainty	45
3.19.	S1.2 Yellowstone Recovery Tests.....	45
3.20.	S1.3 References.....	46
Chapter 4		59
4.	Introduction	59
4.1.	Background: Monitoring Volcanoes Using Relative Velocity Changes	60
4.2.	Geologic Setting of Tungurahua Volcano.....	64
4.3.	Eruptive Episodes at Tungurahua in 2010	65
Chapter 5		69
5.	Data	69
5.1.	Calculation of noise correlation functions (CFs)	70
5.2.	Measuring temporal velocity changes at Tungurahua Volcano	71
5.3.	Dilation Correlation Coefficient Method (DCC).....	73
5.4.	Procedures for measuring dV/V at Tungurahua	75
Chapter 6		77
6.	Results: Correlation functions	77
6.1.	Autocorrelation Functions—Individual Stations Clockwise from North.....	79
6.2.	Cross-Correlation Functions—Near Vent Crossing Station Pairs 82	
6.3.	Cross-Correlation Functions—North Flank (W-E) Crossing Station Pairs.....	83

6.4.	Cross-Correlation Functions—South Flank (W-E) Crossing Station Pairs.....	85
6.5.	Cross-Correlation Functions—East and West Flank (N-S) Crossing Station Pairs.....	86
6.6.	Results Figures: Velocity change, dV/V , and maximum correlation coefficient, X_{\max} , for 6hrs and 1, 5, 7 and 10 day stacks	87
6.7.	Results: Relative velocity change, dV/V	90
Chapter 7		97
7.	Discussion: Comparison of dV/V results with volcanic activity during 2010 at Tungurahua Volcano.....	97
7.1.	Active Episode 1: January 5 th to March	98
7.2.	1 st Quiescent Period: March 20 th to May 26 th	99
7.3.	Active Episode 2: May 26 th to June 18 th with moderate activity through July.....	99
7.4.	2 nd Quiescent Period: August to mid-November	100
7.5.	Active Episode 3: mid-November to December 27 th	101
7.6.	Discussion: Possible causes of dV/V changes at Tungurahua	101
7.7.	Conclusions	103
Chapter 8		105
8.	Background and Methods	105
8.1.	Background: Equipartition of a diffuse wavefield.....	105
8.2.	Background: Testing equipartition and S-to-P energy density ratio	106
8.3.	Background: H/V Ratio and equipartition	108
8.4.	Methods: Data and initial processing	111
8.5.	Methods: H/V Ratio	112
Chapter 9		114

Spectrogram and H/V Results.....	114
9. Results 114	
9.1. Spectrograms and spectral content of the ambient noise wavefield	114
9.2. Results Figures: Spectrograms	117
9.3. Frequency dependent H/V ratio and temporally varying peak H/V ratio.....	123
9.4. Stations BMAS, BULB, BPAT (see Figure 40-Figure 42).	123
9.5. BBIL and BRUN (see Figure 43 and Figure 44)	125
9.6. H/V Figures	126
Chapter 10	134
Discussion and Conclusions.....	134
10. Discussion	134
10.1. Spectral content of the ambient noise wavefield.....	134
10.2. H/V and equipartition at Tungurahua.....	134
10.3. H/V and site effects.....	136
10.4. Conclusions	138
Bibliography.....	140

LIST OF FIGURES

- Figure 1. Collision of the Pacific-Farallon ridge with the North American plate in cross-section, from Atwater [1970]. With the Pacific plate fixed, ridge normal spreading occurs at 5 cm/year and movement of the North American plate is oblique, indicated as out of page. A-B. is the configuration during the early Tertiary, C shows the collision of the trench and Pacific-Farallon ridge, and D shows the current plate configuration in central California. Movement along the San Andreas Fault zone starts between C and D. 3
- Figure 2 Volcanic and tectonic elements of the western United States: (A) Distribution of volcanic rocks younger than 17 Ma, by age and composition (Luedke and Smith, 1984), illustrates the tremendous volcanic activity east of the Cascade Range in the northern extent of the Basin and Range province. (B) Some tectonic elements (after Jordan et al., 2004) superimposed on the map of Luedke and Smith (1984). Solid brown line outlines the Basin and Range province. Volcanic fields younger than 5 Ma illustrate the continuing activity in the Cascade Range and along the High Lava Plains (HLP; brown field) and the eastern Snake River Plain (ESRP). Short curves along the HLP and ESRP are isochrons (ages in Ma) for the migrating silicic volcanism along each volcanic trace. Flood basalt activity was fed from dike systems in the northern Nevada rift (NNR), Steens Mountain (SM), the western Snake River Plain (WSRP) and the Chief Joseph (CJ) and Cornucopia (C) dike swarms of the Columbia River Basalt Group. These dikes occur near the western border of Precambrian North America as defined by the $87\text{Sr}/86\text{Sr}$ 0.706 line (large dot-dash line). Northwest-trending fault systems—Olympic-Wallowa lineament (OWL), Vale (V), Brothers (B), Eugene-Denio (ED) and McLoughlin (Mc)—are shown by the short-dashed lines. Additional features include Newberry Volcano (NB), Owyhee Plateau (OP), Juan de Fuca Plate, San Andreas fault zone (SAFZ), and Mendocino triple junction (MTJ). CA—California; ID—Idaho; OR—Oregon; NV—Nevada; UT—Utah; WA—Washington; WY—Wyoming.[source: Meigs et al., 2009] 7
- Figure 3 Geometry of the paths taken by the waves generated by scatterer, s , to the receivers 1 and 2. [from Sneider, 2004]. The signal recorded at the two stations is the superposition of the plane waves generated by the randomly positioned scatterers. 12
- Figure 4 Map of station locations, shown as colored circles. Stations included come from the networks, XC-High Lava Plains seismic experiment (orange-yellow), TA-Earthscope/USArray Transportable Array (dark blue), BK-Berkeley Digital Seismic Network (BDSN), University of California, Berkeley (light blue); HW-Hanford Washington Seismic Network, Pacific Northwest National Laboratory (green-blue); LB- Leo Brady Network, Sandia National Laboratory (brown); LI- Laser Interferometer Gravitational-Wave experiment (LIGO), Caltech/USGS, Southern

California Seismic Network (blue-green); IU- IRIS/USGS Network, USGS Albuquerque Seismological Laboratory (lime green); NN-Western Great Basin/Eastern Sierra Nevada, University of Nevada, Reno (yellow); XA-Central Oregon Locked Zone Array, EarthScope Flex Array (magenta); US-US National Seismic Network, ANSS Backbone of the USGS/NEIC and USGS/ASL and Earthscope Project of IRIS (red).....	17
Figure 5(a) Daily, stacked, cross-correlation waveforms from 5 receiver pairs. The empirical Green's function was obtained from the time derivative of the average (symmetric) cross-correlation. (b) locations of the station pairs in (a). (c) Signal to noise ratio (SNR) as a function of period for the stacked x-correlations. The average SNR for all cross-correlation pairs is shown in red. Stacking ~3yrs of waveforms enhances the SNR of the resulting x-correlation. Phase velocity measurements from cross-correlations of station pairs with SNR>15 at a given period were used as input for the surface wave tomography	20
Figure 6 Results of the 1-D best fit shear inversion. A) The multi-colored lines with black labels show the sensitivity kernels to shear wave structure as a function of depth for the periods used in this study (8s-40s). The IASP91 shear wave model (yellow line and stars), best fit 1-D shear model (magenta dashed line and squares), and simplified 1-D starting model (blue dot-dashed line and hexagons) are plotted. B) Dispersion curves are plotted for the average phase velocities across the study area with error bars showing the standard error (black dots and error bars), IASP91 predicted phase velocities (yellow stars), best fit 1-D simplified shear model (magenta squares), and predicted phase velocities for the starting model (blue hexagons).....	25
Figure 7. Hazards of Tungurahua Volcano. (Top left) Ash and pumice fall deposit buries a cinderblock house; (Top right) Pyroclastic flow field; (Bottom left) Avalanche and lahar channel cutting through ash, pumice and pyroclastic flow deposits; (Bottom right) Ash plume expelled by Tungurahua (hidden by the white clouds) in July 2009. (Source: S. E. Hanson-Hedgecock).....	61
Figure 8. (a) Simplified geologic map and (b) contour map of Tungurahua Volcano. Marked features include the Tungurahua II avalanche scarp (bold line with teeth), QA, Quebrada Achupashal; QC, Quebrada Confesionario; QM, Quebrada Mandur; QMT, Quebrada Motilones; QLP, Quebrada La Piramide; QPU, Quebrada Palma Urcu; QR, Quebrada Rea, [source: Hall et al., 1999]	65
Figure 9. Map of station locations for the IGEPN broadband seismic array at Tungurahua Volcano, Ecuador deployed in 2010. Topographic contour spacing is every 50 meters. (Source: Keehoon Kim)	69

Figure 10. Individual and 1 year stacked autocorrelation functions at station BRUN for 2010. Colors are amplitude normalized to the mean trace amplitude; red is positive and blue is negative amplitude. The rms amplitude AGC is applied to the traces in a 4s window. Vertical, solid, dark red lines indicate that no CF is calculated for that time period due to a gap in the seismic record. The lower left hand window shows the individual ACF traces calculated from 6hrs records of ambient noise, the lower right window, outlined in black, is the 1-yr stacked ACF that is used as the reference trace in calculating dV/V , with depth calculated- assuming a constant $V_p=2.5\text{km/s}$ and the top window shows the RSAM calculated for each 6hr record at BRUN (blue, dashed line and axis) and the correlation coefficient (green, solid line and axis) calculated between the unstretched reference trace (lower right) and each individual CF trace (lower left). Dashed light gray bars indicate the start and end of the three periods of increased volcanic activity.....	79
Figure 11. Individual and 1 year stacked autocorrelation functions at station BULB for 2010. Annotation is the same as for Figure 10.	80
Figure 12. Individual and 1 year stacked autocorrelation functions at station BPAT for 2010. Annotation is the same as for Figure 10.	80
Figure 13. Individual and 1 year stacked autocorrelation functions at station BMAS for 2010. Annotation is the same as for Figure 10.	81
Figure 14. Individual and 1 year stacked autocorrelation functions at station BBIL for 2010. Annotation is the same as for Figure 10.	81
Figure 15. Individual and 1 year stacked cross-correlation functions at station pair BULB-BMAS, crossing nearest to the vent, for 2010. Annotation is the same as for Figure 10.	82
Figure 16. Individual and 1 year stacked cross-correlation functions at station pair BRUN-BMAS, crossing near to the vent, for 2010. Annotation is the same as for Figure 10.....	82
Figure 17. Individual and 1 year stacked cross-correlation functions at station pair BRUN-BPAT, crossing near to the vent, for 2010. Annotation is the same as for Figure 10.....	83
Figure 18. North flank crossing individual and 1 year stacked cross-correlation functions at station pair BBIL-BRUN for 2010. Annotation is the same as for Figure 10.	83
Figure 19. North flank crossing individual and 1 year stacked cross-correlation functions at station pair BULB-BRUN for 2010. Annotation is the same as for Figure 10.	84

Figure 20. North flank crossing individual and 1 year stacked cross-correlation functions at station pair BBIL-BULB for 2010. Annotation is the same as for Figure 10.	84
Figure 21. South flank crossing individual and 1 year stacked cross-correlation functions at station pair BBIL-BPAT for 2010. Annotation is the same as for Figure 10.	85
Figure 22. South flank crossing individual and 1 year stacked cross-correlation functions at station pair BMAS-BPAT for 2010. Annotation is the same as for Figure 10.	85
Figure 23. East flank crossing individual and 1 year stacked cross-correlation functions at station pair BULB-BPAT for 2010. Annotation is the same as for Figure 10.	86
Figure 24. West flank crossing individual and 1 year stacked cross-correlation functions at station pair BBIL-BMAS for 2010. Annotation is the same as for Figure 10.	86
Figure 25. (top to bottom panel), % dV/V for 6hrs and 1, 5, 7 and 10 days (thick black line) and band-passed filtered from 0.5 to 4Hz (wide-band) averaged over all stations and station pairs with 1σ standard deviation bars (thin dashed line). Also plotted are dashed gray bars indicating the three episodes of increased volcanic activity	87
Figure 26. (top to bottom panel), Average Xmax, corresponding to the dV/V curves for 6hrs, and 1, 5, 7 and 10 days (thick black line) and band-passed filtered from 0.5 to 4 Hz (wide-band) averaged over all stations and station. Annotation is the same as for Figure 25	87
Figure 27. (top to bottom panel), % dV/V for 6hrs and 1, 5, 7 and 10 days (thick black line) and band-passed filtered from 0.5 to 2 Hz (low frequency) averaged over all stations and station pairs with 1σ standard deviation bars (thin dashed line). Also plotted are dashed gray bars indicating the three episodes of increased volcanic activity.	88
Figure 28. (top to bottom panel), Average Xmax, corresponding to the dV/V curves for 6hrs, and 1, 5, 7 and 10 days (thick black line) and band-passed filtered from 0.5 to 2Hz (low-frequency) averaged over all stations and station. Annotation is the same as for Figure 27	88
Figure 29. (top to bottom panel), % dV/V for 6hrs and 1, 5, 7 and 10 days (thick black line) and band-passed filtered from 2 to 4 Hz (high frequency) averaged over all stations and station pairs with 1σ standard deviation bars (thin dashed line). Also plotted are dashed gray bars indicating the three episodes of increased volcanic activity	89

Figure 30.(top to bottom panel), Average X_{max} , corresponding to the dV/V curves for 6hrs, and 1, 5, 7 and 10 days (thick black line) and band-passed filtered from 0.5 to 2Hz (low-frequency) averaged over all stations and station. Annotation is the same as for Figure 29Results: Velocity changes, dV/V	89
Figure 31.% dV/V for 1- (thick solid black line) and 7 day-stacks (dashed red line) averaged over all stations and station pairs with 1σ standard deviation bars (thin dashed line). Prior to calculation of dV/V the CFs were filtered in the bands (a) 0.5-4Hz (wide-band), (b) 0.5-2Hz (low frequency), and (c) 2-4Hz (high frequency) Also plotted are dashed gray bars indicating the three episodes of increased volcanic activity.....	93
Figure 32. (top panel) % dV/V for 1- (thick solid black line) and 7 day-stacks (dashed red line) averaged over all stations and station pairs with 1σ standard deviation bars (thin dashed line). Also plotted are significant eruptions noted in the text (yellow stars) and gray bars that indicate the three episodes of increased volcanic activity. RSAM (2nd panel, dashed line), number of LPs (3rd panel, dot-dashed line) and number of eruption tremor waveforms (4th panel, horizontal bars) recorded per day are plotted in the three panels below the top, respectively. CFs were band-passed filtered in 0.5-4Hz (wide-band) prior to calculation of dV/V	97
Figure 33 Depth dependence, measured as a function of the shear wavelength λ_s , of energy ratios for equipartitioned elastic waves calculated for a homogeneous elastic half-space. The depth kernels are calculated for the shear to compressional deformation energy ratio (Bottom) and the vertical to horizontal kinetic energy ratio (Top). (source: Margerin et al., 2009)	108
Figure 34. Map of station locations for the IGEPN broadband seismic array at Tungurahua Volcano, Ecuador deployed in 2010. Topographic contour spacing is every 50 meters. (Source: Keehoon Kim)	112
Figure 35. Spectrogram for BULB, calculated from each 6-hour ambient noise record for the two horizontal components, East-West (E, top panel), North-South (N, middle panel), and vertical (Z, bottom panel) component at Tungurahua Volcano in 2010. The horizontal axis indicates the day in 2010, the vertical axis the frequency, and the colors represent the smooth amplitudes of the power spectra in decibels (Db).	118
Figure 36. Spectrogram for BPAT, calculated from each 6-hour ambient noise record for the two horizontal components, East-West (E, top panel), North-South (N, middle panel), and vertical (Z, bottom panel) component at Tungurahua Volcano in 2010. The horizontal axis indicates the day in 2010, the vertical axis the frequency, and the colors represent the smooth amplitudes of the power spectra in decibels (Db).	119

- Figure 37. Spectrogram for BMAS, calculated from each 6-hour ambient noise record for the two horizontal components, East-West (E, top panel), North-South (N, middle panel), and vertical (Z, bottom panel) component at Tungurahua Volcano in 2010. The horizontal axis indicates the day in 2010, the vertical axis the frequency, and the colors represent the smooth amplitudes of the power spectra in decibels (Db). 120
- Figure 38 Spectrogram for BBIL, calculated from each 6-hour ambient noise record for the two horizontal components, East-West (E, top panel), North-South (N, middle panel), and vertical (Z, bottom panel) component at Tungurahua Volcano in 2010. The horizontal axis indicates the day in 2010, the vertical axis the frequency, and the colors represent the smooth amplitudes of the power spectra in decibels (Db). 121
- Figure 39. Spectrogram for BRUN, calculated from each 6-hour ambient noise record for the two horizontal components, East-West (E, top panel), North-South (N, middle panel), and vertical (Z, bottom panel) component at Tungurahua Volcano in 2010. The horizontal axis indicates the day in 2010, the vertical axis the frequency, and the colors represent the smooth amplitudes of the power spectra in decibels (Db). 122
- Figure 40. H/V at BMAS on Tungurahua Volcano, 2010. (Bottom panel) Frequency dependent H/V: The horizontal axis indicates the day in 2010, the vertical axis the frequency, and the colors represent the H/V amplitude values in decibels (Db). (Top panel) Peak H/V is shown for the wide (0.5-4 Hz) (black line), low frequency (0.5-2 Hz) (blue dashed line) and high frequency (2-4 Hz) (red dotted line) bands. The horizontal axis indicates the day in 2010 and the vertical axis the peak H/V value. 127
- Figure 41. H/V at BULB on Tungurahua Volcano, 2010. (Bottom panel) Frequency dependent H/V: The horizontal axis indicates the day in 2010, the vertical axis the frequency, and the colors represent the H/V amplitude values in decibels (Db). (Top panel) Peak H/V is shown for the wide (0.5-4 Hz) (black line), low frequency (0.5-2 Hz) (blue dashed line) and high frequency (2-4 Hz) (red dotted line) bands. The horizontal axis indicates the day in 2010 and the vertical axis the peak H/V value. 128
- Figure 42. H/V at BPAT on Tungurahua Volcano, 2010. (Bottom panel) Frequency dependent H/V: The horizontal axis indicates the day in 2010, the vertical axis the frequency, and the colors represent the H/V amplitude values in decibels (Db). (Top panel) Peak H/V is shown for the wide (0.5-4 Hz) (black line), low frequency (0.5-2 Hz) (blue dashed line) and high frequency (2-4 Hz) (red dotted line) bands. The horizontal axis indicates the day in 2010 and the vertical axis the peak H/V value. 129

Figure 43. H/V at BBIL on Tungurahua Volcano, 2010. (Bottom panel) Frequency dependent H/V: The horizontal axis indicates the day in 2010, the vertical axis the frequency, and the colors represent the H/V amplitude values in decibels (Db). (Top panel) Peak H/V is shown for the wide (0.5-4 Hz) (black line), low frequency (0.5-2 Hz) (blue dashed line) and high frequency (2-4 Hz) (red dotted line) bands. The horizontal axis indicates the day in 2010 and the vertical axis the peak H/V value.	130
Figure 44. H/V at BRUN on Tungurahua Volcano, 2010. (Bottom panel) Frequency dependent H/V: The horizontal axis indicates the day in 2010, the vertical axis the frequency, and the colors represent the H/V amplitude values in decibels (Db). (Top panel) Peak H/V is shown for the wide (0.5-4 Hz) (black line), low frequency (0.5-2 Hz) (blue dashed line) and high frequency (2-4 Hz) (red dotted line) bands. The horizontal axis indicates the day in 2010 and the vertical axis the peak H/V value.	131
Figure 45. The wide band (0.5-4 Hz) peak H/V at each station located on Tungurahua Volcano, 2010. The bottom panel shows the mean peak H/V averaged over all the stations with 1σ error bar shown (red line). The horizontal axis indicates the day in 2010 and the vertical axis the peak H/V value.	132
Figure 46. The low frequency band (0.5-2 Hz) peak H/V at each station located on Tungurahua Volcano, 2010. The bottom panel shows the mean peak H/V averaged over all the stations with 1σ error bar shown (red line). The horizontal axis indicates the day in 2010 and the vertical axis the peak H/V value.	132
Figure 47. The high frequency band (2-4 Hz) peak H/V at each station located on Tungurahua Volcano, 2010. The bottom panel shows the mean peak H/V averaged over all the stations with 1σ error bar shown (red line). The horizontal axis indicates the day in 2010 and the vertical axis the peak H/V value.	133

LIST OF TABLES

Table 1. Summary of mean dV/V , the 1σ standard deviation, X_{\max} and corresponding RMS ϵ for each stack length of individual CFs used in the calculation (6-hrs and 1, 5, 7 and 10 day stacks) and each filter band (0.5-4 Hz, 0.5-2 Hz, 2-4 Hz) applied to the CFs.	92
---	----

Chapter 1

TECTONICS AND VOLCANISM IN THE WESTERN UNITED STATES

1.1. Introduction

The focus of this work is to develop an understanding of the lithospheric structure and development of the mid-Miocene-to-present intraplate volcanism of the northwest United States within the context of the regions' complex tectonic and magmatic history. The region of interest is bounded to the north by the Siletzia terrane and Blue Mountains province of northern Oregon; to the east by the Cretaceous to Oligocene thrust belts in central Utah and western Wyoming; to the south by the northern Basin and Range Province of Nevada and Utah and includes the Coastal Ranges, Cascades and northern Sierra Nevada of northern California, and extends just west of the Cascades. The mid-Miocene-to-present volcanic provinces that developed within this region include the Steens/Columbia River flood basalts, Yellowstone-Snake River Plains (YSRP) and High Lava Plains (HLP) volcanic tracks, and the arc volcanism of the Cascades from the Washington-Oregon border to northern California.

1.2. Tectonic Setting

Interaction between the Pacific, Farallon and North American tectonic plates plays a dominant role in the timing and location of volcanism and crustal deformation within the western United States from the mid to late Tertiary. Analysis of the magnetic anomaly patterns on the Pacific Plate along the west coast of North America established that a spreading ridge

once existed at the boundary between the Pacific and Farallon tectonic plates [Atwater, 1970; Atwater and Stock 1998]. The magnetic anomalies on the Pacific Plate off the western US represent only half the expected symmetrical pattern produced by a spreading ridge. Indications are that the other half of the anomalies on the old Farallon plate, and the Pacific-Farallon spreading ridge that produced them, has been subducted and consumed at the boundary with the North American plate. The youngest anomalies on the Pacific plate indicate that the Pacific-Farallon trench was active until about 29 Ma south of the Mendocino fracture zone.

Subduction, at a rate of ~7-10 cm/year, along western North America allowed the North American plate to overrun the Farallon plate and Pacific-Farallon ridge, which was spreading at a rate of ~5 cm/year. Along the segment between the Pioneer and Murray fault zones the Farallon plate broke and pieces of the ridge began colliding with the trench, while spreading along the Pacific-Farallon ridge slowed and ceased by ~32 Ma [Atwater, 1970]. As the trench and ridge came into contact the thin and hot lithosphere of the Pacific plate at the Pacific-Farallon ridge cooled and become attached to continental crust, after which oblique motion between the Pacific and North American plate resulted in a new transform plate margin and the formation of the San Andreas fault zone no earlier than ~30 Ma [Atwater, 1970] (see Figure 1). The broken segment of the Farallon was subducted by ~24 Ma and by 20 Ma had cooled and strengthened enough that motion between the Pacific and North American plates could cause deformation along what is now the San Andreas fault zone and folding of the Coastal Range [Crowell, 1968; Atwater, 1970].

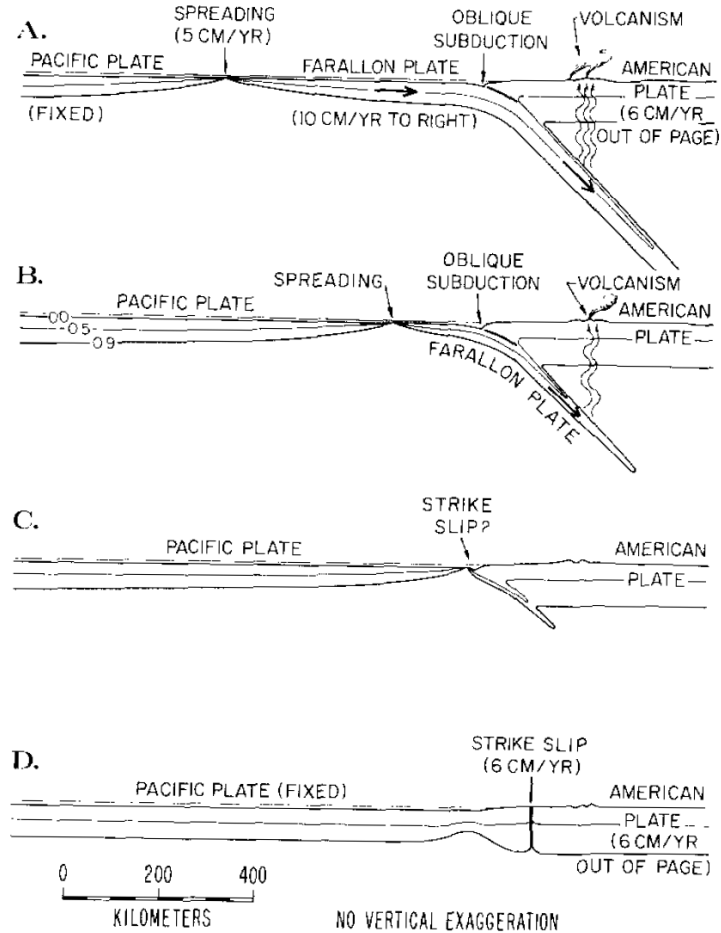


Figure 1. Collision of the Pacific-Farallon ridge with the North American plate in cross-section, from Atwater [1970]. With the Pacific plate fixed, ridge normal spreading occurs at 5 cm/year and movement of the North American plate is oblique, indicated as out of page. A-B. is the configuration during the early Tertiary, C shows the collision of the trench and Pacific-Farallon ridge, and D shows the current plate configuration in central California. Movement along the San Andreas Fault zone starts between C and D.

Strike-slip displacement along the new transform plate boundary, the San Andreas Fault zone, has been on the order of $\sim 315 \pm 10$ km since 23 Ma [Atwater and Stock, 1998]. This movement has translated the Mendocino triple junction northwards to its present position beneath the Sierran-Great Valley block, just north of Sutter Buttes, at $\sim 39.5^\circ$ latitude, by ~ 4 Ma [Atwater and Stock, 1998]. Motion between the Pacific and North American plates is also accommodated by deformation within weak continental lithosphere of the Basin and Range.

The NW oblique displacement has resulted in a margin normal extension of up to ~2 cm/year and the opening of the Basin and Range province [Atwater, 1970; Atwater and Stock, 1998, McQuarrie and Wernicke, 2005]. Basin and Range extension reached southern Oregon by ~22Ma [Scarberry *et al.*, 2009].

This transform motion along the boundary between the North American and Pacific plates has caused a margin normal extension of up to 2 cm/year that resulted in southwest to northeast trending extension within what is now the Basin and Range province [McQuarrie and Wernicke, 2005], which reached southern Oregon by ~22 Ma [Scarberry *et al.*, 2009]. Changes in deformation direction around 8 Ma appear to correlate with increasing westward extension in the northern Basin and Range between the Sierra Nevada and the Colorado Plateau [Atwater and Stock, 1998; McQuarrie and Wernicke, 2005]. From 30-12 Ma the Pacific plate was displaced along an azimuth of N60°W at a rate of ~33mm/year; from 12-8 Ma this rate increased to ~55mm/year, and after 8 Ma plate motion changed to a more northerly direction, N37°W.

North of the San Andreas transform boundary the Juan de Fuca slab, a remnant of the broken up Farallon slab, continues to subduct at a rate of ~5.8 cm/year parallel to the Blanco fracture zone. A net compression NNE of about ~2.5 cm/year results from the interaction of the Juan de Fuca plate and the North American plate that moves parallel the SAF at a rate of 5~.8 cm/year. This oblique convergence and subduction of the Juan de Fuca plate, a remnant of the larger Farallon plate, beneath North America drives continued volcanism in the Cascades from the coast of southern Canada, into Washington and northern California.

1.3. Volcanism in the Northwestern United States

The mid-Miocene volcanic history of the Pacific Northwest is complicated and not fully understood. Cascade arc volcanism initiated parallel to the present arc some ~42 Ma [Madsen *et al.*, 2006] after the accretion of the Siletzia oceanic terrane, which is now found in northern Oregon into Washington. Extensive volcanism within Basin and Range formed in a north to south trending “ignimbrite sweep,” characterized by large-volume eruptions of silicic magmas from centers migrating over much of western North America between 50 and 20 Ma [Lipman *et al.*, 1972].

Cascadia back-arc region, mid-Miocene volcanism began ~17 Ma with the eruption of the voluminous Steens/Columbia River flood basalts (Figure 1). In a time span of ~1.5 Ma, over 200,000 km³ of basalt were erupted from N-S trending dike swarms located within the accreted terranes along the western boundary of Precambrian North America [Camp and Ross, 2004]. The initiation of silicic volcanism at the southwest edge of the Owyhee Plateau (OP) followed the cessation of flood basalt volcanism [Brueseke *et al.*, 2008]. By ~12 Ma, two distinct lineaments of time-progressive silicic volcanism had developed, both originating in the vicinity of the OP: the Yellowstone-Snake River Plain (YSRP) lineament that trend northeast parallel to apparent plate motion after ~12 Ma [Pierce and Morgan, 1992] and the High Lava Plains (HLP) volcanic lineament that trends to the northwest, terminating at present near Newberry volcano [Jordan *et al.*, 2004]. Basaltic eruptive activity that is not time progressive persists into the Holocene along both the HLP and YSRP [Camp and Ross, 2004 and references therein].

1.4. High Lava Plains, Oregon (HLP)

The High Lava Plains (HLP) volcanic track is the northwest trending track of rhyolite volcanism that is the mirror-image of the Yellowstone-Snake River Plains (YSRP) track. The track originated around 12 Ma near the margins of the Owyhee Plateau (OP), like the YSRP track, and is currently thought to end at present at Newberry volcano. The rhyolite volcanism of the HLP is less voluminous, less evolved, and influenced by the Precambrian Craton than the YSRP rhyolite volcanism [Pierce and Morgan, 1992; Savov *et al.*, 2009]. At the younger, westerly end of the HLP track, volcanism is enhanced by the merging of the Cascade arc with the HLP track. The link between the two volcanic provinces is indicated by the isotopic similarity of low-K tholeiites in the Cascades and HLP [Meigs *et al.*, 2009].

Basaltic volcanism occurs along the length of the HLP track, but is not time progressive in contrast to the rhyolitic volcanism [Meigs, *et al.*, 2009]. The basaltic volcanism that occurred concurrent with the HLP track volcanism is dominated by primarily low-K, high-AL olivine tholeiites (HAOT) that is similar to mid-ocean ridge basalt [Hart 1985]. HAOT volcanics are present throughout eastern Oregon [McKee *et al.*, 1983; Hart *et al.*, 1984], along the YSRP track [Leeman, 1982] and are present along with calc-alkaline lavas of Medicine Lake and the Modoc Plateau in the southern Cascades [Hart *et al.*, 1984; Bacon *et al.*, 1997]. Hart *et al.*, [1984] suggests that the basalts are produced by scattered fissure and fissure-controlled eruptions triggered by extensional tectonics of the Great Basin, consistent with the N-S alignment of some individual eruptive centers. The HAOTs are primitive, having a low degree of fractionation and low concentration of large ionic lithophile elements (LILE), which may be consistent with the hypothesize lack of mantle lithosphere beneath the HLP [Till *et al.*, 2013].

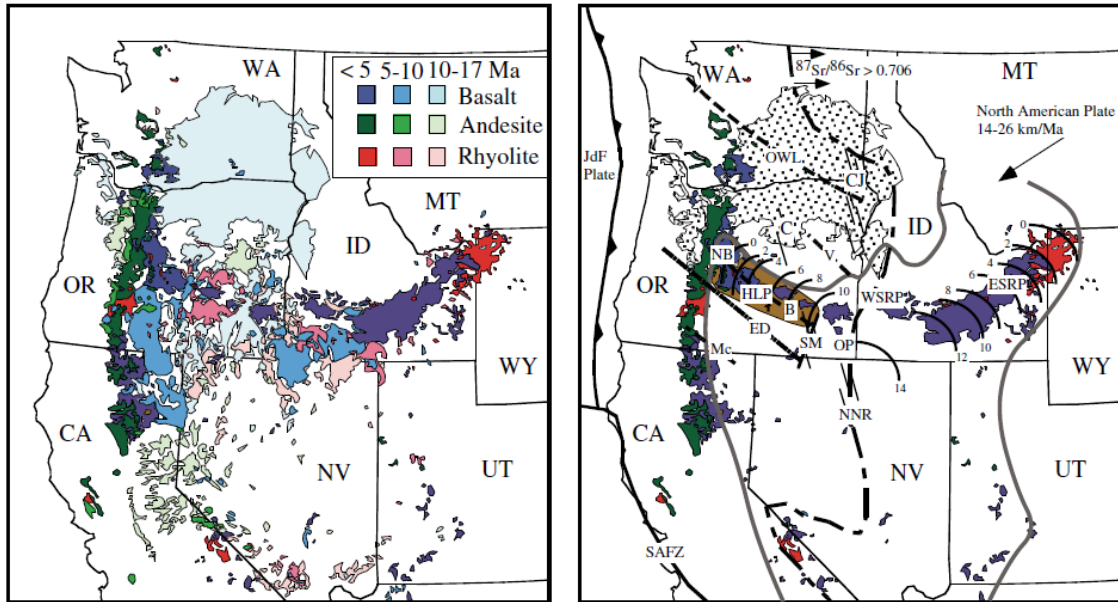


Figure 2 Volcanic and tectonic elements of the western United States: (A) Distribution of volcanic rocks younger than 17 Ma, by age and composition (Luedke and Smith, 1984), illustrates the tremendous volcanic activity east of the Cascade Range in the northern extent of the Basin and Range province. (B) Some tectonic elements (after Jordan *et al.*, 2004) superimposed on the map of Luedke and Smith (1984). Solid brown line outlines the Basin and Range province. Volcanic fields younger than 5 Ma illustrate the continuing activity in the Cascade Range and along the High Lava Plains (HLP; brown field) and the eastern Snake River Plain (ESRP). Short curves along the HLP and ESRP are isochrons (ages in Ma) for the migrating silicic volcanism along each volcanic trace. Flood basalt activity was fed from dike systems in the northern Nevada rift (NNR), Steens Mountain (SM), the western Snake River Plain (WSRP) and the Chief Joseph (CJ) and Cornucopia (C) dike swarms of the Columbia River Basalt Group. These dikes occur near the western border of Precambrian North America as defined by the $^{87}\text{Sr}/^{86}\text{Sr} > 0.706$ line (large dot-dash line). Northwest-trending fault systems—Olympic-Wallowa lineament (OWL), Vale (V), Brothers (B), Eugene-Denio (ED) and McLoughlin (Mc)—are shown by the short-dashed lines. Additional features include Newberry Volcano (NB), Owyhee Plateau (OP), Juan de Fuca Plate, San Andreas fault zone (SAFZ), and Mendocino triple junction (MTJ). CA—California; ID—Idaho; OR—Oregon; NV—Nevada; UT—Utah; WA—Washington; WY—Wyoming. [source: Meigs *et al.*, 2009]

The HLP is dominated, structurally, by the northwest striking faults of the Brothers Fault Zone, the interpreted northern boundary of the Basin and Range extensional province [Lawrence, 1976]. The faults of this zone are only a few kilometers long with throws of a few tens of meters [Lawrence, 1976; Trench *et al.*, 2012]. This is in contrast to the Basin and Range

faults that are tens of kilometers long with throws on the order of kilometers, widely spaced, and bounded by grabens. Extension along this northern boundary is small compared with the central Basin and Range, on the order of 17% since ~16 Ma [Wells and Heller, 1988; Wernicke, 1992].

1.5. Yellowstone-Snake River Plains (YSRP)

The YSRP hot spot track is composed of a series of large calderas and rhyolitic centers that become progressively younger from the McDermitt caldera complex, at ~16.1 Ma, to the Yellowstone caldera, at present. This time progressive trend has been attributed to the North American plate movement over a stationary hotspot (e.g., Pierce and Morgan, 1992). Though there is still much debate regarding the nature of the hotspot; whether it is generated by the upwelling tail of a deep mantle plume [e.g. Draper, 1991; Pierce and Morgan, 1992; Smith and Braile, 1993; Takahashi *et al.*, 1998; Camp and Ross, 2004, Smith *et al.*, 2009; Obrebski *et al.*, 2010; Xue and Allen, 2010] or from shallower upper mantle upwellings and convection [e.g. Lipman *et al.*, 1972; Cross and Pilger, 1982; Carlson and Hart, 1987; Humphreys *et al.*, 2000; and Christiansen *et al.*, 2002; James *et al.*, 2011]

Basalts, similar to the HAOTs of the High Lava Plains, also occur along the Snake River Plains to Yellowstone [Leeman, 1982]. They are found as extensive basaltic lava flows, shield volcanoes, fissure vents and cinder cones that overlay the rhyolitic ignimbrite, lava domes and fall deposits [Greeley, 1982]. DeNosaquo *et al.* [2009] proposed a model for the bimodal volcanism along the YSRP track where magma ascends to a level of neutral buoyancy in the mid-crust. Over time, as basaltic magma continues to be injected into the crust, the crustal conduits become depleted in low temperature melting materials required for production of rhyolitic magmas. When the North American plate moves past the mantle hotspot, removing

the source of heat, the silicic melt solidifies, but basaltic melt can continue to reach the surface. As the hotspot source moves farther away basalt will eventually solidify in the mid-crust forming a mafic sill that is observed by seismic techniques along the Eastern Snake River Plain [Braile *et al.*, 1982; DeNosaquo *et al.*, 2009]

1.6. Problem Statement

The relationship between these volcanic episodes in the Pacific Northwest with each other and with coeval tectonic processes is not well understood and is the subject of ongoing debate. The three major mid-Miocene volcanic provinces are linked by their coeval development, though, the differences in their geologic settings and characteristics of each volcanic province that defy a simple explanation. For example, the YSRP track progresses towards the northeast, parallel to North American plate motion, and is frequently attributed to a deep mantle plume source. However, the HLP track progresses to the northwest over the same time period in a direction that is oblique to the regional plate motion, which implies a different source mechanism for the formation of the HLP.

Previously proposed hypotheses for the genesis of mid-Miocene volcanism in the northwest US include a mantle hotspot source [Pierce and Morgan, 1992; Geist and Richards, 1993; Camp and Ross, 2004; Jordan *et al.*, 2004; Smith *et al.*, 2009]; lithospheric thinning as a result of Basin and Range extension [Cross and Pilger, 1982; Christiansen *et al.*, 2002], asthenospheric flow due to rollback of the subducting Juan de Fuca plate [Carlson and Hart, 1987], back-arc extension [Christiansen and McKee, 1978], and lithospheric delamination [Hales *et al.*, 2005]. Each hypothesis attempts to answer fundamental questions about the mechanisms for generation of melt, generation of large volume intraplate volcanism, the generation of a variety of coeval volcanic products, and the time progressive nature of the

silicic volcanic lineaments (HLP and YSRP). There is a lack of consensus about which hypothesis is best able to resolve these questions.

In the following chapters (Chapter 2-Chapter 3), I describe the use of ambient noise tomography to develop a better model of the crustal and uppermost mantle in the northwest United States and subsurface image of the various volcanic provinces with an emphasis on the High Lava Plains and its connections to the Yellowstone-Snake River Plains track, Steens/Columbia River Flood Basalt province, the Owyhee Plateau, and Basin and Range. Although other seismic methods have been used to examine the structure of the northwestern US [e.g., Bensen *et al.*, 2008; Stachnik *et al.*, 2008; Warren *et al.*, 2008; Gao *et al.*, 2011; Porritt *et al.*, 2011; Yang *et al.*, 2008, 2011; Moschetti *et al.*, 2010a,b; Wagner *et al.*, 2010], the work described in this first section is the first ambient noise tomography study using the increased resolution of the densely spaced stations of the High Lava Plains seismic experiment in addition to the EarthScope/USArray Transportable Array.

Chapter 2

METHODS

2. Methods

Experimental and theoretical studies [e.g. Lobkis and Weaver, 2001; Snieder, 2004; Weaver and Lobkis, 2004; Roux, *et al.*, 2005; Wapenaar, 2004] have shown that the empirical Green's function (EGF) between two receivers can be determined from the cross-correlation of recordings of the diffuse wavefield at those two receiver positions. Using ambient seismic noise records, methods were developed by Bensen *et al.*, [2007; 2008] to measure fundamental mode Rayleigh wave phase and group velocities from the cross-correlation of these seismic records. I use these methods to determine the 2D velocity structure of the High Lava Plains, Oregon (HLP) and surrounding regions from ambient noise recordings at 361 broadband seismic stations deployed across the Pacific Northwest from January 2006 to September 2009. These measurements are then used to construct 3D shear wave velocity models of the crust and uppermost mantle in these regions. In this chapter I describe the theoretical background for ambient noise correlations, phase velocity measurement, and inversion for shear velocity structure and error measurements.

2.1. Background: Obtaining the empirical Green's function from diffuse field correlations theory

Diffuse field correlations have been used, in the field of acoustics, to determine the elastic response of a medium [Lobkis and Weaver, 2001; Sneider, 2004; Weaver and Lobkis, 2004; Roux, *et al.*, 2005; Wapenaar, 2004]. Diffuse fields can be generated by a random distribution of sources or by a random distribution of scatterers [Schuster, 2009]. The generated field is composed of incoherent waves with random phases and amplitudes, propagating in all directions. This implies that from the cross-correlation of the diffuse field at any two stations a coherent wavefront will emerge as a result of the accumulated contributions over a long enough time from waves that propagate along any possible path between and pass through both stations [Sabra, *et al.*, 2005].

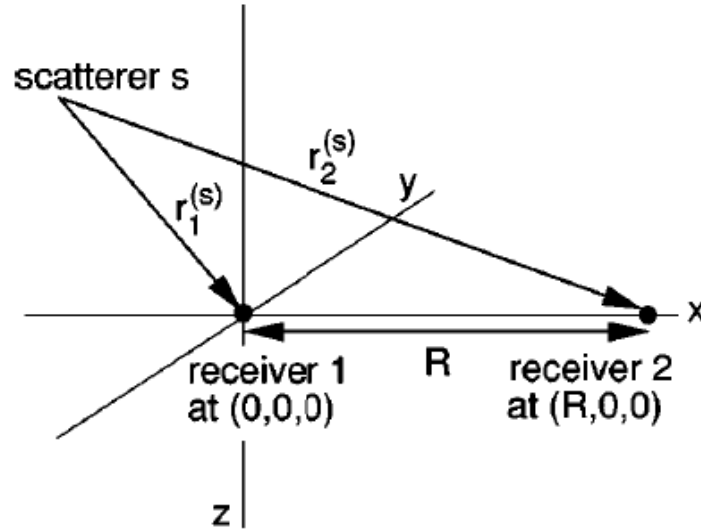


Figure 3 Geometry of the paths taken by the waves generated by scatterer, s , to the receivers 1 and 2. [from Sneider, 2004]. The signal recorded at the two stations is the superposition of the plane waves generated by the randomly positioned scatterers.

Sneider [2004] demonstrated this property for the assumption that the diffuse wavefield recorded at two receivers, $\phi_{1,2}$, can be represented as the superposition of plane waves

generated by a medium of randomly positioned scatterers, s , whose wavepaths pass through both receiver 1 and receiver 2,

$$\phi_{1,2}(t) = \sum_s S_s \left(t - \frac{r_{1,2}^{(2)}}{c} \right) / r_{1,2}^{(s)} \quad (1)$$

where S_s is the scattered waveform and $r_{1,2}^{(s)}$ is the distance from the scatterer to the receivers 1 and 2. The correlation of the waves recorded at the two receivers is defined as

$$C(\tau) \equiv \int_0^T \phi_2(t + \tau) \phi_1(t) dt, \quad (2)$$

where $\phi_2(t + \tau)$ is the field at receiver 2 and time, $t + \tau$, and $\phi_1(t)$ is the field at receiver 1 at time, t . Using the definition of the field in equation (1) the correlation can be written as

$$C(\tau) = \sum_{s,s'} \int_0^T S_s(t) S_{s'} \left(t + \frac{r_1^{(s')} - r_2^{(s')}}{c} + \tau \right) dt / r_1^{(s')} r_2^{(s')} \quad (3)$$

The correlation can be split into two sums, one over the diagonal terms, when $s = s'$ ($C_D(\tau)$) and a sum over the cross terms, when $s \neq s'$, ($C_C(\tau)$).

$$C(\tau) = \underbrace{\sum_s \int_0^T S_s(t) S_s(t + \tau) dt}_{C_D(\tau)} + \underbrace{\sum_{s \neq s'} \int_0^T S_s(t) S_{s'}(t + \tau) dt}_{C_C(\tau)} \quad (4)$$

where the travel time between station 1 and 2, $\frac{(r_1^{(s)} - r_2^{(s)})}{c}$, is included in the τ term. For a fully diffuse wavefield composed of random incoherent waves the position of the scatterers is uncorrelated and the ensemble average of the scattered waves is zero, $\langle S_s(t) S_s(t') \rangle = 0$, for $s \neq s'$ and $\langle S_s(t) S_s(t') \rangle = C_s(t - t')$ for $s = s'$. Given this relationship the time averaged cross-correlation the ensemble average of the second term, which describes the cross terms, $C_C(\tau)$, goes to zero

$$\langle C_C(\tau) \rangle = \sum_{s \neq s'} \int_0^T \langle S_s(t) S_{s'}(t + \tau) \rangle dt = 0 \quad (5)$$

The cross-correlation function (3) then reduces to

$$C(\tau) = \sum_s C_s \left(\tau + \frac{(r_1^{(s)} - r_2^{(s)})}{c} \right) / r_1^{(s)} r_2^{(s)} \quad (6)$$

Transforming the time domain cross-correlation (6) into the frequency domain power spectrum function gives

$$C(\tau) = \sum_s |S_s(\omega)|^2 \frac{\exp[(r_1^{(s)} - r_2^{(s)})/c]}{r_1^{(s)} r_2^{(s)}} \quad (7)$$

The spectral energy density, $|S_s(\omega)|^2$, is assumed constant for the case of a fully diffuse wavefield and (7) is rewritten as,

$$C(\tau) = \overline{|S(\omega)|^2} \sum_s \frac{\exp[(r_1^{(s)} - r_2^{(s)})/c]}{r_1^{(s)} r_2^{(s)}} \quad (8)$$

where $\overline{|S(\omega)|^2} = \frac{1}{N} \sum_s |S(\omega)|^2$, N is the number of scatterers and $\overline{|S(\omega)|^2}$ is the average spectral energy density of the diffuse wavefield.

To calculate the cross-correlation as a function of the distance between the two stations instead of with respect to the distance from each scatterer, (8) is first rewritten as a volume integral weighted by scatterer density, n ,

$$C(\omega) = \overline{|S(\omega)|^2} \int \frac{\exp[(r_1 - r_2)/c]}{r_1 r_2} n \, dx dy dz \quad (9)$$

which Sneider *et al.* [2004] evaluated using the stationary phase approximation [Bleistein, 1984] to rewrite (9) in terms of the distance between the two receivers

$$C(\omega) = 2\pi \overline{|S(\omega)|^2} \frac{c}{-i\omega} \int_{-\infty}^{\infty} \frac{e^{ik(|R-x|-|x|)}}{||R-x|-|x||} n dx \quad (10)$$

The stationary phase approximation is used, for example, to evaluate sinusoid functions with rapidly varying phase functions, such as occurs in case of scattering. These incoherent sinusoids will sum constructively along the receiver line, where $y = z = 0$, and destructively everywhere else in the volume.

Then, ignoring the contribution from the regions where the wavefield interferes destructively, $C(\omega)$ can be rewritten as

$$C(\omega) = 8\pi^2 \overline{|S(\omega)|^2} \left(\frac{c}{-i\omega} \right) \left(-\frac{e^{ikR}}{4\pi R} \int_{-\infty}^0 ndx - \frac{e^{-ikR}}{4\pi R} \int_R^{\infty} ndx \right) \quad (11)$$

where $-\frac{e^{ikR}}{4\pi R}$ is the retarded Green's function, $G_{12}(t)$, for waves propagating between the receiver 1 to 2 and $-\frac{e^{-ikR}}{4\pi R}$ is the advanced Green's function, $G_{12}(-t)$, for waves propagating between receiver 2 to 1. The time derivative of the inverse Fourier transform of (11) gives the sum of the retarded and advanced Green's functions, so that the symmetric Green's function becomes

$$G_{12}(t) = -\frac{d}{dt} \left[\frac{G_{12}(t) + G_{12}(-t)}{2} \right], 0 \leq t \leq \infty \quad (12)$$

2.2. Background: Applications to seismic noise

Shapiro and Campillo [2004] first showed that the Green's function could be extracted from the cross-correlation of vertical component ambient seismic noise. The signal that emerges is composed primarily of fundamental mode Rayleigh waves [Sabra *et al.*, 2005]. Dispersion characteristics, phase and group velocity, of the Rayleigh waves can be measured and tomographic methods used to determine 2-D and 3-D earth structure [Bensen *et al.*, 2007, 2008; Lin *et al.*, 2008 and references therein]. The first ambient noise tomographic images of Rayleigh wave group speeds at periods of 7 to 20 s in southern California were presented by Shapiro *et al.* [2005] and Sabra *et al.* [2005]. These studies were followed by applications of

ANT on both continental and regional scales throughout world including studies in Europe, New Zealand, and South Africa in addition to the US [e.g. Lin *et al.* 2007, 2008; Mochetti *et al.* 2007; Bensen *et al.* 2008; Yang *et al.* 2007, etc.].

2.3. Methods: Data

I determined the 2D and 3D velocity structure of the High Lava Plains and surrounding regions using ambient noise recordings from 361 broadband seismic stations deployed across the Pacific Northwest from January 2006 to September 2009 (Figure 4). Records from the 118 broadband seismometers that comprised the High Lava Plains (HLP) seismic experiment [Eagar *et al.*, 2011] and 243 broadband stations from the EarthScope/USArray Transportable Array (TA) (rows D-Q and columns 1-19) are used. An additional 43 stations from the other regional networks supplement the more extensive TA and HLP stations. The TA stations have a station spacing of ~70km and the HLP stations have a ~20-30 km station spacing. Stations used are located in a region bounded by to the west by the coast of Oregon, just to the east of the Yellowstone-Snake River Plain (YSRP), to north of the Blue Mountains, and to the south by the northern-most extent of the Basin and Range.

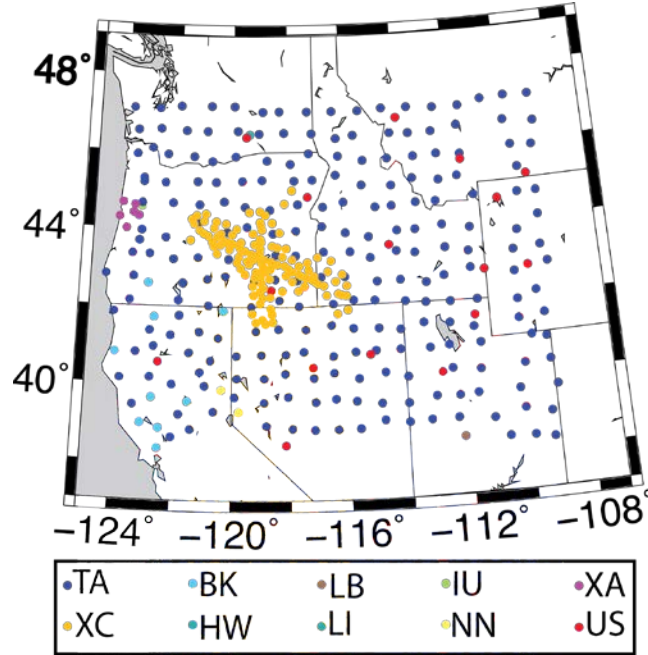


Figure 4 Map of station locations, shown as colored circles. Stations included come from the networks, XC-High Lava Plains seismic experiment (orange-yellow), TA-Earthscope/USArray Transportable Array (dark blue), BK- Berkeley Digital Seismic Network (BDSN), University of California, Berkeley (light blue); HW-Hanford Washington Seismic Network, Pacific Northwest National Laboratory (green-blue); LB- Leo Brady Network, Sandia National Laboratory (brown); LI- Laser Interferometer Gravitational-Wave experiment (LIGO), Caltech/USGS, Southern California Seismic Network (blue-green); IU- IRIS/USGS Network, USGS Albuquerque Seismological Laboratory (lime green); NN-Western Great Basin/Eastern Sierra Nevada, University of Nevada, Reno (yellow); XA-Central Oregon Locked Zone Array, EarthScope Flex Array (magenta); US-US National Seismic Network, ANSS Backbone of the USGS/NEIC and USGS/ASL and Earthscope Project of IRIS (red).

2.4. Methods: Processing ambient noise records to obtain the empirical Green's function (EGF)

The methods of Bensen *et al.* [2007, 2008] were used to process the recordings of ambient noise and determining fundamental mode Rayleigh wave phase velocities. The procedure for processing the ambient noise data to obtain dispersion measurements is a four step process: (1) Preliminary processing of individual station records to enhance the noise signal and remove earthquake signals and instrumental irregularities, (2) cross-correlation and stacking of daily seismic records, (3) measurement of dispersion curves from the empirical

Green's function (EGF), and (4) error analysis and selection of acceptable measurements to be input in tomography.

In the preliminary processing, the instrument response is removed and each daily seismic record is band-passed filtered from 5 to 150s. To reduce the effect of earthquakes that could mask the ambient noise signal, a running-absolute-mean normalization is applied to the data records. This normalization is done by computing the running average of the absolute value of the waveform amplitude in a normalization time window of fixed length, 20s, and weighting the waveform at the center of the window by the inverse of the average.

After the effects of earthquakes are removed, monochromatic sources cause peaks in the amplitude spectrum at certain frequencies, which violates the assumption of a diffuse field that has an equal amplitude contribution at all frequencies [Weaver, 1985]. Peaks in the amplitude spectrum exist at ~15s, ~7.5s and above 50s corresponding to large contribution from the primary and secondary microseism, and Earth "hum" [Rhie and Romanowicz, 2004], respectively [Bensen *et al.*, 2007]. To normalize ("whiten") the amplitude of the separate spectral components the noise signal, in the frequency domain, is inversely weighted by a smoothed version of the amplitude spectrum. This spectral whitening broadens the band of the ambient noise signal in cross-correlation to prevent degradation of the noise signal due to the persistent monochromatic sources [Bensen, *et al.*, 2007].

Cross-correlations are calculated for the daily seismic records between each station pair in the frequency domain (see Figure 5a,b). The daily cross-correlations are then stacked, which improves signal-to-noise ratio (SNR) of the records (Figure 5c). The resulting cross-correlation waveform has both a positive (causal signal) and negative (acausal signal) time lag (Figure 5a). The positive and negative lags represent coherent surface waves travelling in opposite

directions between two stations. Since the stacked cross-correlations represent about 3 years of data, we assume that the distribution of noise source is azimuthally homogenous and we can average the causal and acausal signals to yield the symmetric-signal used in the dispersion measurements. 68,531 inter-station stacked cross-correlations are calculated. The empirical Green's function (EGF) (equation 12) is then obtained from the derivative of the average of the positive and negative lag signals, the 'symmetric signal' of the cross-correlation:

$$G_{12}(t) = -\frac{d}{dt} \left[\frac{C_{12}(t) + C_{12}(-t)}{2} \right], 0 \leq t \leq \infty$$

where $G_{12}(t)$ is the empirical Green's function, $C_{12}(t)$ is the positive lag signal and $C_{12}(-t)$ is the negative lag signal [Lin, *et al.*, 2008].

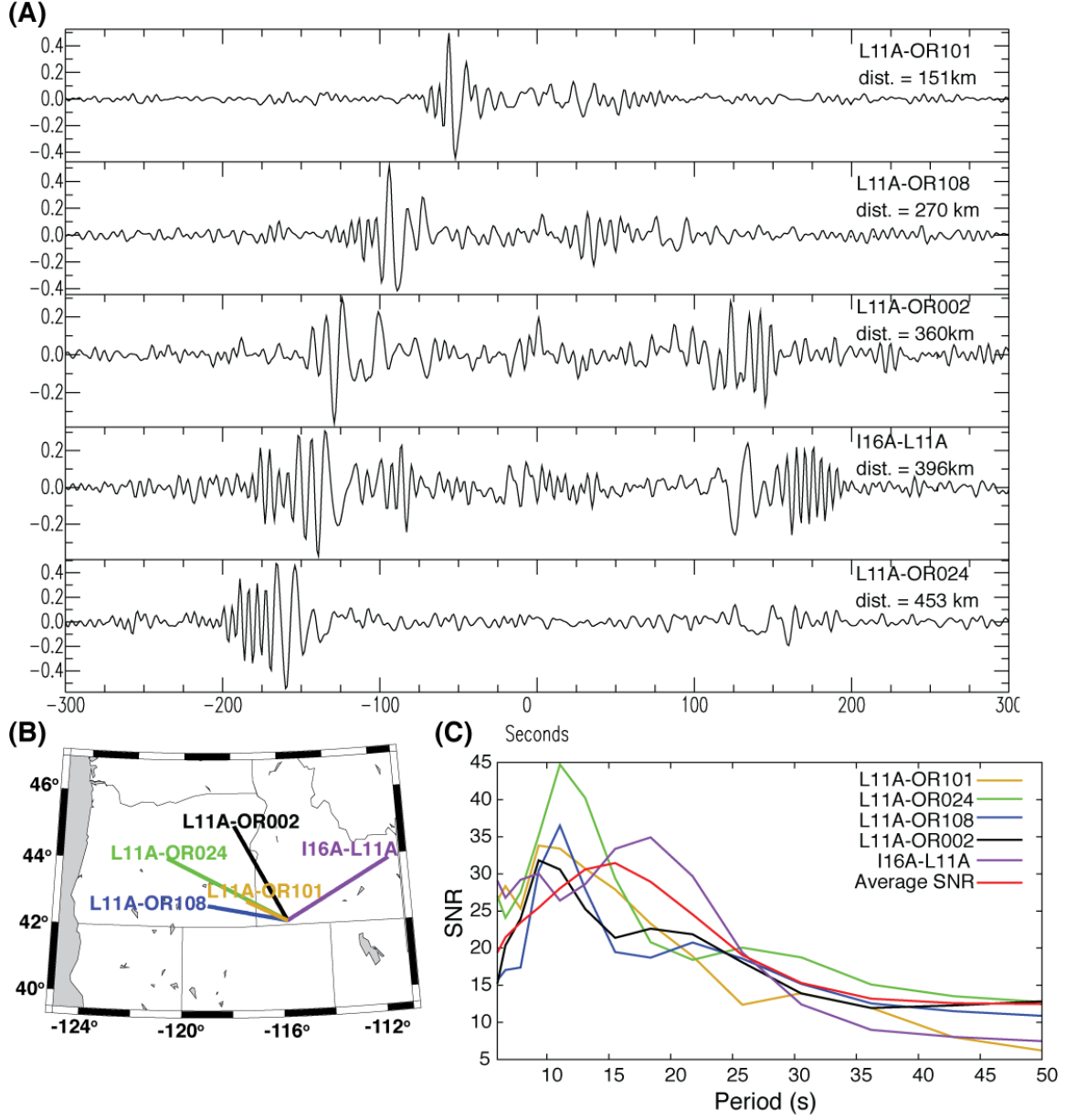


Figure 5(a) Daily, stacked, cross-correlation waveforms from 5 receiver pairs. The empirical Green's function was obtained from the time derivative of the average (symmetric) cross-correlation. (b) locations of the station pairs in (a). (c) Signal to noise ratio (SNR) as a function of period for the stacked x-correlations. The average SNR for all cross-correlation pairs is shown in red. Stacking ~ 3 yrs of waveforms enhances the SNR of the resulting x-correlation. Phase velocity measurements from cross-correlations of station pairs with $\text{SNR} > 15$ at a given period were used as input for the surface wave tomography

2.5. Methods: Determination of phase velocities from EGFs

Phase velocity dispersion measurements are determined from the EGF using frequency-time analysis (FTAN) [Levshin, *et al.*, 2001; Levshin and Ritzwoller, 2001]. In the frequency domain, the EGF signal is passed through a system of relatively narrow-band filters of the form, $F_g(\omega - \omega_o) = e^{-\alpha\left(\frac{\omega - \omega_o}{\omega_o}\right)^2}$, with central frequency, ω_o , that vary from 4 to 50s. The combination of all the filtered signals are treated as a complex function of ω_o and t

$$S(\omega_o, t) = \int_{-\infty}^{\infty} F_g(\omega - \omega_o) S_a(\omega) e^{i\omega t} d\omega \quad (13)$$

where $S(\omega_o, t)$ is the frequency-time representation of the signal, $F_g(\omega - \omega_o)$ are the Gaussian filters, and $S_a(\omega)$ is the spectrum of the signal. The group travel time, t_{max} , is determined from the peak of the envelope function, $|S(\omega_o, t)|$, and the phase is determined from the phase function, $\arg|S(\omega_o, t)| = \arctan(\text{Im}(S(\omega_o, t)) / \text{Re}(S(\omega_o, t)))$. The group velocity is r/t_{max} , where r is the distance between two stations. For a given frequency, ω , the EGF at time, t , the phase function is:

$$\varphi(t) = kr - \omega t + \frac{\pi}{2} - \frac{\pi}{4} + N \cdot 2\pi + \lambda \quad (14)$$

where k is the wavenumber, $\pi/2$ is the phase shift from the negative time-derivative, $-\pi/4$ is the phase shift due to the interference of the assumed homogenous source distribution [Sneider, 2004], λ is the source phase ambiguity term or ‘initial phase’, and $N \cdot 2\pi$ is the intrinsic phase ambiguity of phase measurement. The $N \cdot 2\pi$ is estimated using the average phase velocity curve of Gao, *et al.* [2011] as the reference curve. The phase velocity c is calculated as,

$$c = \frac{\omega}{r} = \frac{r\omega}{\varphi(t_{max}) + \omega t_{max} - \frac{\pi}{4} - N \cdot 2\pi - \lambda} \quad (15)$$

2.6. Methods: Fundamental mode Raleigh wave maps from ambient noise tomography

High quality dispersion measurements used for input into the inversion for phase velocity maps are selected based on three criteria: (1) that the inter-station spacing r is greater than three wavelengths to satisfy far-field approximation, (2) the SNR is greater than 15 at a given period, and (3) each measurement must be coherent with other measurements as measured by its ability to fit a smooth tomographic map. The selected phase velocity measurements are then inverted for phase speed maps and different periods of interest using the method of Barmin, *et al.* [2001]. The method estimates the 2-D isotropic phase velocity model by minimizing a penalty function composed of data misfit, model smoothness, and perturbation to an input reference model, weighted by local path density of the form:

$$(\mathbf{G}(\mathbf{m}) - \mathbf{d})^T \mathbf{C}^{-1} (\mathbf{G}(\mathbf{m}) - \mathbf{d}) + \alpha^2 \|\mathbf{F}(\mathbf{m})\|^2 + \beta \|\mathbf{H}(\mathbf{m})\|^2,$$

where \mathbf{G} is the forward operator computing travel times from a model, \mathbf{d} is the data vector of measured surface wave travel times, and \mathbf{C} is the data covariance matrix assumed here to be diagonal and composed of the square of the measurement standard deviations. $\mathbf{F}(\mathbf{m})$ is the spatial smoothing function, which is controlled by the spatial smoothing width or correlation length, σ , and $\mathbf{H}(\mathbf{m})$ penalizes the model based on path density and azimuthal distribution. The regularization parameters α , β , and σ are user controlled parameters that are determined by trial and error. [Barmin, *et al.* 2001]

Phase velocity maps for periods from 6 to 40s are calculated on a $0.25^\circ \times 0.25^\circ$ grid in two steps. First, an over-smoothed, over-damped model is calculated at each period. The standard deviation of the travel-time residuals is calculated and measurements with residuals greater than three standard deviations from the mean are removed, following the criteria of Bensen *et al.* [2008]. Second, the remaining measurements are used to determine the final phase velocity maps (Chapter 3, Figures S1 and S2).

2.7. Inversion for Shear Velocity and Shear Model Parameterization

The final phase velocity maps at 8, 10, 12, 20, 25, 30, 33 and 40s (Figure S1, S2) are used to invert for the 3-D shear velocity model beneath the HLP and adjoining tectonic provinces. I first calculate the 1-D shear wave velocity model that best fits the average observed phase velocities determined from the final phase velocity maps. The shear velocity, V_s , and density, ρ , for the initial starting model is assigned from IASP91 [Kennett, 1991] and plotted in Figure 6 as the yellow line and stars. The V_p/V_s ratio of the model is kept constant at 1.78, which is set from the previous study of Moschetti *et al.* [2010]. The crust is parameterized with 6 layers of individual thicknesses between 5 and 8km and a total thickness of 35km. The mantle is parameterized with 9 layers that range in thickness between 10 and 50 km (Figure 6). I modified the thickness of each layer so that the corresponding diagonal element of the resolution matrix is greater than 0.1 but less than 0.5. Results of the inversion for the 1-D shear velocity model that best fits the average observed phase velocities are plotted in Figure 6 in magenta dashed lines and squares. The best-fit 1-D shear velocity model contains significantly lower velocities in the upper mantle than the IASP91 model, but is similar to the western United States reference shear velocity model calculated by Moschetti *et al.* [2010].

I used a simplified version of the best-fit 1-D shear model, described above, as the starting model for the many 1-D inversions that go into the final 3-D model. This simplified model and its predicted phase velocities are plotted in Figure 6 as a blue dot-dashed line and hexagons. I adjust the simplified 1-D best-fit shear model for each individual 1-D inversion to account for the Moho depth variations at the grid point in question. The Moho depth at each grid point is determined from a 2-D crustal thickness map made using results from the receiver function studies of Eagar *et al.*, [2011] for the greater HLP region and is supplemented by the EARS catalogue [Crotwell and Owens, 2005]. Continental crust varies from about ~27 to 42

km in thickness, while oceanic crust remains fixed at 10 km thickness. In an attempt to preserve original layer thicknesses as much as possible, and only change the thickness of the layer in which the new Moho is located and in those layers that are immediately adjacent to the Moho-containing layer. The Moho containing layer is split into two sub-layers, with the sub-layer above the Moho added to the layer above it, and the sub-layer below the Moho added to the layer below it. I divide the layer that the thicker sub-layer was added to in half, which keeps the total number of model layers constant. The lower-most crustal velocities are assigned to the layers above the new Moho and uppermost mantle velocities to the layers below the new Moho.

Given the new shear velocity starting model at each grid point, I calculate predicted phase velocities using the method of Saito *et al.* [1988], which are then compared to the observed phase velocities determined from the phase velocity maps at each period for each grid point. I use a linearized inversion technique based on the iterative least-squares approach of Tarantola and Valette [1982] to determine the shear velocity model that minimizes the misfit between the observed and predicted phase velocities [Weerartne *et al.*, 2003]. The 3-D shear wave velocity model is a composite of the 1-D shear wave models at each grid point.

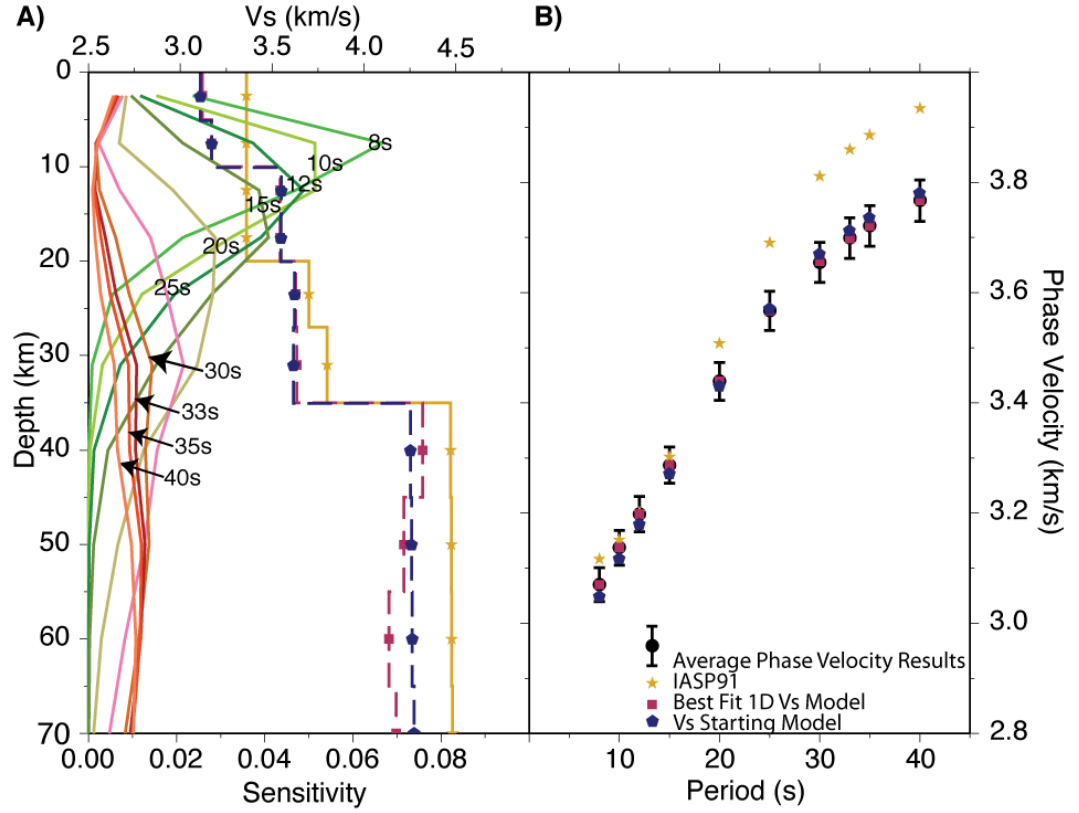


Figure 6 Results of the 1-D best fit shear inversion. A) The multi-colored lines with black labels show the sensitivity kernels to shear wave structure as a function of depth for the periods used in this study (8s-40s). The IASP91 shear wave model (yellow line and stars), best fit 1-D shear model (magenta dashed line and squares), and simplified 1-D starting model (blue dot-dashed line and hexagons) are plotted. B) Dispersion curves are plotted for the average phase velocities across the study area with error bars showing the standard error (black dots and error bars), IASP91 predicted phase velocities (yellow stars), best fit 1-D simplified shear model (magenta squares), and predicted phase velocities for the starting model (blue hexagons).

2.8. Dispersion misfit

I calculate the RMS misfit between the observed phase velocities and those calculated from the shear wave velocity models, averaged over all periods at each grid node. The average RMS misfit over the entire grid is 0.024km/s with a maximum of 0.088km/s. The largest misfits occur in the Columbia Basin and Coastal Ranges/Great Valley region of northern California and occur at the shorter periods (<20s) that are most sensitive to crustal structures.

The very low velocities in these regions likely result from the thick sedimentary cover in the Columbia Basin and Great Valley and the highly deformed crust of the Coastal Ranges.

2.9. Shear wave velocity model uncertainty

I evaluate the sensitivity of our shear wave velocity models to small changes in phase velocity by adding small amounts of noise to each of the phase velocities at each point and recalculating the shear wave velocities using these adjusted values. The Gaussian random noise that is added has a mean of 0 and a standard deviation of $\pm 1\%$ of the observed phase velocity at that period for that grid point. This process is repeated 100 times at each grid point, after which I calculate the standard deviation of the resultant shear wave velocity columns at all depths. Shear velocity uncertainties are plotted in Figure S8 and S9. In general, phase velocity deviations of $\pm 1\%$ produce an average shear velocity uncertainty of ~ 0.02 km/s with a maximum of 0.033 km/s.

Chapter 3

CONSTRAINTS ON THE CAUSES OF MID-MIOCENE VOLCANISM IN THE PACIFIC NORTHWEST US FROM AMBIENT NOISE TOMOGRAPHY

Sara Hanson-Hedgecock¹, Lara S. Wagner¹, Matthew J. Fouch², David E. James²

¹Department of Geological Sciences, University of North Carolina at Chapel Hill, 104 South
Rd., Mitchell Hall, CB #3315, Chapel Hill, NC, 27599-3315, United States;

²Department of Terrestrial Magnetism, Carnegie Institution of Washington, 5241 Broad
Branch Rd., NW, Washington, DC, 20015-1305, United States

3. Abstract

We use data from the 118-station High Lava Plains (HLP) seismic experiment together with other regional broadband seismic data to image the 3D shear wave velocity structure in the Pacific Northwest using ambient noise tomography. This extensive data set allows us to resolve fine-scale crustal structures throughout the HLP area in finer detail than previous studies. Our results show 1) a high velocity cylinder in the crust and average velocities in the upper mantle beneath the Owyhee Plateau; 2) a mid-crustal high velocity anomaly along the Snake River Plain that also extends south into Nevada and Utah; 3) a low velocity anomaly directly beneath Yellowstone throughout the crust; and 4) low velocities beneath the HLP both in the crust and uppermost mantle, possibly indicating very thin or absent mantle lithosphere in the area. These features provide important constraints on possible models for Miocene to recent volcanism in the Pacific Northwest.

3.1. Introduction

The relationship between the various mid-Miocene to present volcanic episodes in the Pacific Northwest with each other and with coeval tectonic processes is not well understood. Extensive mid-Miocene volcanism in the Cascadia back-arc region began ~17 Ma with the eruption of the voluminous Steens/Columbia River flood basalts (Figure 1). In a time span of ~1.5 Ma, over 200,000 km³ of basalt were erupted from N-S trending dike swarms located within the accreted terranes along the western boundary of Precambrian North America [Camp and Ross, 2004]. The initiation of silicic volcanism at the southwest edge of the Owyhee Plateau (OP) followed the cessation of flood basalt volcanism. By ~12 Ma, two distinct tracks of time-progressive silicic volcanism had developed, both originating in the vicinity of the OP: the Yellowstone-Snake River Plain (YSRP) track that trends to the northeast parallel to apparent plate motion [Pierce and Morgan, 1992] and the High Lava Plains (HLP) volcanic lineament that trends to the northwest, terminating at present near Newberry volcano [Jordan *et al.*, 2004]. Basaltic eruptive activity that is not time progressive persists into the Holocene along both the HLP and YSRP [Camp and Ross, 2004 and references therein].

The early Steens/Columbia River flood basalt activity has been interpreted by some as the result of an impacting plume head in SE Oregon at ~17 Ma [e.g., Camp and Ross, 2004; Jordan *et al.*, 2004]. The YSRP volcanism has been interpreted as a hotspot track formed as the North American continent migrated southwest across a stationary plume tail [e.g. Pierce and Morgan, 1992; Smith *et al.*, 2009]. The time-progressive HLP volcanic lineament is difficult to explain with a plume model because its silicic volcanism trends at an oblique angle to plate motion. Other explanations for the formation of the HLP include lithospheric thinning as a result of Basin and Range extension [Cross and Pilger, 1982; Christiansen *et al.*, 2002],

rollback of the subducting Juan de Fuca plate [Carlson and Hart, 1987], and back-arc extension [Christiansen and McKee, 1978].

Seismic imaging can help constrain the relative importance of various tectonic structures in the formation of the HLP. Recent studies of shear wave velocity structure, determined from teleseismic surface waves, show significant differences in the upper mantle beneath the HLP and YSRP [Warren *et al.*, 2008; Wagner *et al.*, 2010]. However, these studies primarily image regions below the crust-mantle boundary. Ambient noise studies can be used to examine shallower structures in the crust and uppermost mantle, but recent broad-scale studies of the entire western US do not have sufficient resolution to examine the HLP in detail [e.g., Bensen *et al.*, 2008; Yang *et al.*, 2008, 2011; Moschetti *et al.*, 2010a,b] and the more fine-scale regional studies do not focus on the HLP [e.g. Stachnik *et al.*, 2008; Gao *et al.*, 2011; Porritt *et al.*, 2011]. Although other seismic methods have been used to examine the structure of the HLP, this is the first ambient noise tomography study to use the increased resolution of the densely spaced stations of the High Lava Plains seismic experiment in addition to the EarthScope/USArray Transportable Array to provide to examine the crust and uppermost mantle of the HLP and surrounding regions in detail.

3.2. Data and Methods

Data for this project come from 361 broadband seismic stations deployed across the Pacific Northwest from January 2006 to September 2009 (Figure 1). We used records from the 118 broadband seismometers that comprised the High Lava Plains seismic experiment [Eagar *et al.*, 2011] and 243 broadband stations from the EarthScope/USArray Transportable Array (TA) (rows D-Q and columns 1-19). An additional 43 stations from the other regional networks supplement the more extensive TA and HLP stations.

3.3. Phase velocity models from ambient noise tomography

We determine surface wave dispersion curves from cross-correlations of ambient noise [Bensen *et al.* 2008 and references therein]. We invert these phase velocity measurements to obtain 2-D phase velocity models via the method of Barmin *et al.* [2001]. We remove data with travel-time residuals greater than three standard deviations from the mean following the criteria of Bensen *et al.* [2008]. From the remaining data we calculate final phase velocity maps for periods at 8, 10, 12, 20, 25, 30, 33 and 40s on a $0.25^\circ \times 0.25^\circ$ grid (see Figures S1 & S2 and text of the auxiliary materials for details).

3.4. Shear wave velocity model

We invert for the 1-D shear wave velocity structure at each point in map view. We use a simplified starting model and adjust the crustal thickness at each point according to the receiver function results of Eagar *et al.* [2011] (see Figure S3 and text of the auxiliary material). Following the method of Weeraratne *et al.* [2003], we invert for the 1D shear wave velocity model at each point in map view that most accurately predicts the suite of phase velocities observed at that location. We then combine these 1-D shear wave models to produce a 3-D shear wave velocity model. The RMS misfit between the observed phase velocities at each point and the phase velocities predicted by our shear wave velocity models can be seen in Figure S7. Given the range of periods used in this inversion, our best resolution ranges between 5 and 50 km depth, though we are able to recover anomalies from depths up to 70 km. We performed error analyses to investigate the sensitivity of our shear wave models to error in the phase velocities (see Figure S8 and text of the auxiliary materials).

3.5. Results and Discussion

The results of our shear wave velocity inversions are shown in Figures 2, 3, S4-S6, and S12-S15. We recover many of the major features seen in previous ambient noise tomography studies, giving us confidence in the robustness of our results. The major features include the shallow low velocity Columbia Basin anomaly in northern Oregon and Washington that is likely due to an extensive sedimentary basin in the area [Gao *et al.*, 2011; Moschetti, *et al.*, 2010a], the N-S trending high velocity anomaly associated with the ancestral Cascades [Porritt *et al.*, 2011; Gao *et al.*, 2011], the high velocity Wyoming Craton and Siletzia terrane [Gao *et al.*, 2011], the broad low velocities associated with the Basin and Range, Coastal Ranges of northern California [Moschetti, *et al.*, 2010a; Yang *et al.*, 2008, 2011], and the Intermountain Belt [Yang *et al.*, 2011]. In addition to these features, our study reveals a number of additional structures that have either not been identified or not been discussed in previous papers.

3.6. Owyhee Plateau Anomaly

The Owyhee Plateau (OP) is a relatively undeformed region [Shoemaker, 2004] characterized by somewhat thicker crust than the surrounding HLP and Basin and Range province [Eagar *et al.* 2011]. The central portion of the Plateau is visible in our models as a roughly cylindrical high velocity anomaly that extends through the upper and mid crust (Figure 2a, b, anomaly 1). The lowermost crust and upper mantle beneath this anomaly appear to have more velocities that are lower than within the Plateau and higher than the low velocities associated with the volcanic lineaments (henceforth referred to as average velocities)(Figure 2c, d, Figure 3a) in contrast to the very low velocities of the adjacent High Lava Plains and Basin and Range.

The genesis of the high Vs anomaly in the upper crust of the Owyhee Plateau is uncertain. The thickened lithospheric block that became the OP appears to have formed by lithospheric scale Sevier age thrusting that juxtaposed Mesozoic accreted lithospheric mantle over older Precambrian cratonic lithospheric mantle [Shoemaker, 2004 and references therein]. The onset of mid-Miocene flood basalt volcanism ca. 17 Ma in the region of the OP was largely limited to its structurally weaker margins, with major eruptive centers located along a narrow array of N-S trending vents in the vicinity of Steens Mountain to the west. At ~11 Ma, Basin and Range extension resulted in the production of mafic basalts along the margins of the OP [Shoemaker, 2004; Shoemaker and Hart, 2002], but by 5 Ma, volcanism on the Plateau itself ceases with only small volcanic centers resuming in the past 1 Ma at the northernmost margins.

One possible interpretation of our observations is that the region of average velocities in the upper mantle beneath the OP could represent older Precambrian lithosphere that has been further depleted during the flood basalt stage [Shoemaker, 2004]. The depleted lithosphere would provide stability to and limit Basin and Range extension within the Plateau. The cylindrical high velocity anomaly in the upper and mid crust could be evidence of a residue left behind from the more limited mid-Miocene volcanism that occurred within the margins of the Plateau.

3.7. High velocity mid-crustal anomaly beneath the SRP

While we are not the first to observe the mid-crustal high velocity anomaly of the SRP [e.g. Smith *et al.*, 1982; Sparlin *et al.*, 1982; Priestley and Orcutt, 1992; Stachnik *et al.*, 2008], our results resolve important distinctions in the lateral extent of this anomaly. In particular, we observe that the southwestern half of this high velocity anomaly extends south of the SRP into

Nevada and Utah. The southward extension of this high velocity anomaly is seen in a number of previous tomography studies, though it has not been discussed explicitly before [Pollitz and Snoke, 2010; Lin *et al.*, 2010; Yang *et al.*, 2011]. Of notable exception are the results of Moschetti *et al.* [2010a,b] who see a high velocity anomaly constrained solely within the limits of the SRP. The methodology of Moschetti *et al.* [2010a,b] differs from those of the previous tomography studies in their inclusion of Love waves and radial anisotropy. While this may suggest that radial anisotropy is responsible for the southward extension of the high velocity anomaly in our results, we see no corresponding feature in the crustal radial anisotropy maps in Moschetti *et al.* [2010b]. The cause of this model discrepancy remains unknown.

The high velocities observed beneath the SRP have been attributed to a mid-crustal layer of mafic sill intrusions [e.g. Peng and Humphreys, 1998, Shervais *et al.*, 2006, Stachnik *et al.* 2008, DeNosaquo *et al.*, 2009]. DeNosaquo *et al.* [2009] use regional gravity anomalies along with other geophysical data to constrain the density structure of these mafic intrusions. The observed gravity anomaly referenced in their study also extends to the south into Utah and Nevada, roughly coincident with our observed high velocity anomaly. This suggests that the same type of sill structures inferred to exist within the SRP may produce the high velocity anomaly south of the SRP. If that is the case, then the broadening of these sill structures along the earlier portions of the SRP volcanic track could indicate a broadening of the mantle upwelling responsible for their formation. This has important implications when considering whether or not the entire SRP track was formed by passage of a narrow plume tail, or whether a more regional upwelling is required to explain the broader anomaly associated with the earlier portions of the volcanic sequence. Evolving stress in the extending lithosphere may also

have focused intrusions farther south for a period of time, regardless of the details of the specific mantle upwelling involved.

3.8. Low velocities in the lower crust beneath Yellowstone

We observe a significant low velocity anomaly directly beneath Yellowstone (Figure 2, anomaly 3) that appears to extend vertically from the surface to the upper mantle (Figure 3). This is consistent with the results of Moschetti *et al.* [2010a,b], but stands in contrast to other previous results that find high shear wave velocities in the lower crust directly beneath Yellowstone, and a SW dipping low velocity anomaly [e.g. Stachnik *et al.*, 2008]. Given that this anomaly is near the edge of our model, we have performed a number of recovery tests to demonstrate the robustness of our results (see Figures S10 and S11 of the auxiliary materials).

The low velocity anomaly under Yellowstone broadens to the southwest in the lower crust and upper mantle, for ~450 kilometers, roughly consistent with earlier results (Figure 3b) [Smith *et al.*, 1982, 2009; Schutt *et al.*, 2008; Stachnik *et al.*, 2008]. Holocene basaltic volcanism in the SRP is roughly co-located with the low shear wave velocities in the lowermost crust and upper mantle (Figure 2c,d, anomaly 3, Figure 3b), suggesting a possible causal link between the persistent low velocities in the upper mantle and lower crust along the northeastern half of the SRP and ongoing basaltic volcanism in the region.

3.9. High Lava Plains low velocity zone

The HLP region exhibits widespread low velocities throughout the crust and upper mantle (Figure 2, anomaly 4). A few features stand out within this region of generally low velocities. At shallow depths (Figure 2a, anomaly 4), the lowest velocities are present beneath the active arc and Newberry caldera. Low velocities are also observed beneath Diamond and

Jordan Craters in eastern Oregon. Along the HLP volcanic track, pronounced low velocities are observed from mid-crustal depths into the upper mantle (Figure 2b, anomaly 4; Figure 3a).

Of particular interest is the apparent absence of mantle lithosphere beneath the HLP (Figure 3). Low velocities directly below the Moho are observed in the region between the subducted Juan de Fuca plate and the mantle beneath the OP. These low velocities could indicate either increased temperatures within a persistent chemically distinct mantle lithosphere, or they could indicate the absence of virtually all mechanical mantle lithosphere. Recent work by Till *et al.* [2012] suggests that primary melts are generated from within these very low velocities regions at depths that are directly beneath the Moho, favoring the latter interpretation. Regardless, the low shear wave velocities suggest a very weak layer underlying the HLP crust, which could help to explain the formation and persistence of volcanism across southeastern Oregon.

3.10. Acknowledgements

We are very grateful to the many people involved in making both the HLP experiment and Transportable Array deployment a reality. Many thanks also to the PASSCAL Instrument Center and the IRIS Data Management Center for their ongoing support, which are supported through the GEO Directorate through the Instrumentation and Facilities Program of the National Science Foundation under Cooperative Agreement EAR-0552316. The High Lava Plains project (<http://www.dtm.ciw.edu/research/HLP>) was funded through NSF award EAR-0507248 (MJF) and EAR-0506914 (DEJ). SHH's and LW's participation was supported by NSF award EAR-0809192. We thank M. Ritzwoller, M. Barmin, and W. Shen for providing the ambient noise tomography codes.

3.11. References

- Barmin, M.P., M.H. Ritzwoller, and A.L. Levshin (2001), A fast and reliable method for surface wave tomography, *Pure Appl. Geophys.*, 158(8), 1351 - 1375.
- Bensen, G.D., M.H. Ritzwoller, and N.M. Shapiro (2008), Broad-band ambient noise surface wave tomography across the United States, *J. Geophys. Res.*, 113, B05306, doi:10.1029/2007JB005248.
- Camp, V.E. and M.E. Ross (2004), Mantle dynamics and genesis of mafic magmatism in the intermontane Pacific Northwest. *J. Geophys. Res.* 109, B08204. Doi:10.1029/2003JB002838.
- Carlson, R.L. and W.K. Hart (1987), Crustal genesis of the Oregon plateau. *J. Geophys. Res.* 92, 6191-6207.
- Christiansen, R.L., G.R. Foulger, and J.R. Evans (2002), Upper-mantle origin of the Yellowstone hotspot. *Geol. Soc. Am. Bull.*, 114, 1245-1256.
- Christiansen, R.L. and E.H. McKee (1978), Late Cenozoic volcanic and tectonic evolution of the Great Basin and Columbia Intermontane regions, in *Geol. Soc. Amer. Memoir.*, edited by R.B. Smith, and G.P. Eaton, 283-311.
- Cross, T.A. and R. H. Pilger (1982), Controls on subduction geometry, location of magmatic arcs, and tectonic arc and back-arc regions. *Geol. Soc. Am. Bull.* 93, 545-562.
- DeNosaquo, K.R., R.B. Smith, and A.R. Lowry (2009), Density and lithospheric strength models of the Yellowstone-Snake River Plain volcanic system from gravity and heat flow data. *J. Volcanol. Geotherm. Res.* 188, 108-127.
- Eagar, K.C., M.J. Fouch, D.E. James, and R.L. Carlson (2011), Crustal structure beneath the High Lava Plains of eastern Oregon and surrounding regions from receiver function analysis, *J. Geophys. Res.*, 116, B02313, doi:10.1029/2010JB007795.
- Gao, H., E. D. Humphreys, H. Yao, and R. D. van der Hilst, (2011), Crustal and lithosphere structure of the Pacific Northwest with ambient noise tomography, *Earth Planet. Space. L.* 304, 202-211.
- James, D.E., M.J. Fouch, R.W. Carlson, and J.B. Roth, (2011), Slab fragmentation, edge flow and the origin of the Yellowstone hotspot track, *Earth Planet. Sci. Lett.*, doi: 10.1016/j.epsl.2011.09.007
- Jordan, B.T., A.L. Grunder, R.A. Duncan, and A.L. Deino (2004), Geochronology of age progressive volcanism of the Oregon High Lava Plains: implications for the plume interpretation of Yellowstone. *J. Geophys. Res.* 109, B10202. doi:10.1029/ 2003JB002776.

- Lin, F.-C., M.H. Ritzwoller, Y. Yang, M.P. Moschetti, M.J. Fouch, (2010), Complex and variable crustal and uppermost mantle seismic anisotropy in the western United States. *Nature: Geoscience*, 4, doi: 10.108/ngeo1036
- Moschetti, M.P., M.H. Ritzwoller, F-C. Lin, Y. Yang (2010a), Crustal shear wave velocity structure of the western United States inferred from ambient seismic noise and earthquake data. *J. Geophys. Res.* 115, B10306. doi:10.1029/2010JB007448.
- Moschetti, M.P., M.H. Ritzwoller, F-C. Lin, Y. Yang (2010b), Seismic evidence for widespread western-US deep-crustal deformation caused by extension. *Nature*, 464, doi: 10.138/nature08951.
- Pierce, K.L. and L.A. Morgan (1992), The track of the Yellowstone hotspot: Volcanism, faulting, and uplift, in: Link, P.K., M.A. Kuntz, and L.B. Platt (eds.), *Regional geology of eastern Idaho and western Wyoming*, *Geol. Soc. Am. Memoir* 179.
- Pollitz, F.F., and A. Snoke (2010), Rayleigh-wave phase-velocity maps and three-dimensional shear velocity structure of the western US from local non-plane surface wave tomography, *Geophys. J. Int.*, 180, p. 1153 - 1169
- Porritt, R.W., R.M. Allen, D.V. Boyarko, and M.R. Brudzinski (2011), Investigation of Cascadia segmentation with ambient noise tomography. *Earth Planet. Sci. Lett.*, 309, 67-76.
- Priestley, K. and J. Orcutt (1982), Extreme travel time inversion of explosion seismology data from the eastern Snake River Plain, Idaho, *J. Geophys. Res.*, 87(B4), 2634-2642.
- Schutt, D.L., K. Dueker, and H. Yuan (2008), Crust and upper mantle velocity structure of Yellowstone hot spot and surroundings, *J. Geophys. Res.*, doi: 10.1029/2007JB005109.
- Shervais, J.W., S.K. Vetter, B.B. Hanan (2006), Layered mafic sill complex beneath the eastern Snake River Plain: evidence from cyclic geochemical variations in basalt. *Geology* 34, 365–368.
- Shoemaker, K.A. (2004). The tectonomagmatic evolution of the Late Cenozoic Owyhee Plateau, Northwestern United States. Ph.D. Dissertation, Dep. of Geol., Miami University, Oxford, Ohio, USA.
- Shoemaker, K.A. and W.K. Hart (2002), Temporal controls on basalt genesis and evolution on the Owyhee Plateau, Idaho and Oregon, in B. Bonnichsen, C.M. White, and M. McCurry, eds., *Tectonic and Magmatic Evolution of the Snake River Plain: Idaho Geological Survey Bulletin* 30, p. 313-328.
- Smith, R.B., M. Jordan, B. Steinberger, C.M. Puskas, J. Farrell, G.P. Waite, S. Husen, W. Chang, and R. O'Connell (2009), Geodynamics of the Yellowstone hotspot and mantle plume, Seismic and GPS imaging, kinematics, and mantle flow, *J. Volcanol. Geotherm. Res.* 188, 26-56.

- Smith, R. B., M. Schilly, L. W. Braile, J. Ansorge, J. L. Lehman, M. R. Baker, C. Prodehl, J. H. Healy, S. Mueller, and R. W. Greensfelder (1982), The 1978 Yellowstone–Eastern Snake River Plain seismic profiling experiment: Crustal structure of the Yellowstone region and experiment design, *J. Geophys. Res.*, 87(B4), 2583–2596, doi:10.1029/JB087iB04p02583.
- Sparlin, M.A., L.W. Braile, and R.B. Smith (1982), Crustal structure of the eastern Snake River Plain determined from ray trace modeling of seismic refraction data. *J. Geophys. Res.* 87, 2619–2633.
- Stachnik, J.C., K. Dueker, D.L. Schutt, and H. Yuan, (2008), Imaging Yellowstone plume–lithosphere interactions from inversion of ballistic and diffusive Rayleigh wave dispersion and crustal thickness data. *Geochem. Geophys. Geosys.*, G3 9(6), Q06004. doi:10.1029/2008GC001992.
- Till, C.B., T.L. Grove, R.W. Carlson, J.M. Donnelly-Nolan, W.K. Hart, M.J. Fouch, L.S. Wagner, S. Hanson-Hedgecock, (2012, submitted?), Constraints on the depths and temperatures of anhydrous asthenospheric melting and the location of the lithosphere–asthenosphere boundary beneath southern Oregon and northern California
- Wagner, L.S., D.W. Forsyth, M.J. Fouch, and D.E. James (2010), Detailed three-dimensional shear wave velocity structure of the northwestern United States from Rayleigh wave tomography. *Earth Planet. Sci. Lett.* 299, 273–284.
- Warren, L.M., J.A. Snoke, D.E. James (2008), S-wave velocity structure beneath the High Lava Plains, Oregon, from Rayleigh-wave dispersion inversion. *Earth Planet. Sci. Lett.* 274, 121–131
- Weeraratne, D.S., D.W. Forsyth, K.M. Fischer, and A.A. Nyblade (2003), Evidence for an upper mantle plume beneath the Tanzanian craton from Rayleigh wave tomography, *J. Geophys. Res.*, 108, 2427, doi: 688 10.1029/2002JB002273.
- Wernicke, B., G.J. Axen, and J.K. Snow (1988), Basin and Range extensional tectonics at the latitude of Las Vegas, Nevada. *Bull. Seismol. Soc. Am.* 100, 1738–1757.
- Yang, Y., M.H. Ritzwoller, F.-C. Lin, M.P. Moschetti, and N.M. Shapiro (2008), Structure of the crust and uppermost mantle beneath the western United States revealed by ambient noise and earthquake tomography, *J. Geophys. Res.* 113, B12310, doi: 10.1029/2008JB005833.
- Yang, Y., W. Shen and M.H. Ritzwoller, (2011) Surface wave tomography in a large-scale seismic array combining ambient noise and teleseismic earthquake data, *Earthquake Science*, 24, 55–64

3.12. Figures, Hanson-Hedgecock *et al.*, 2011

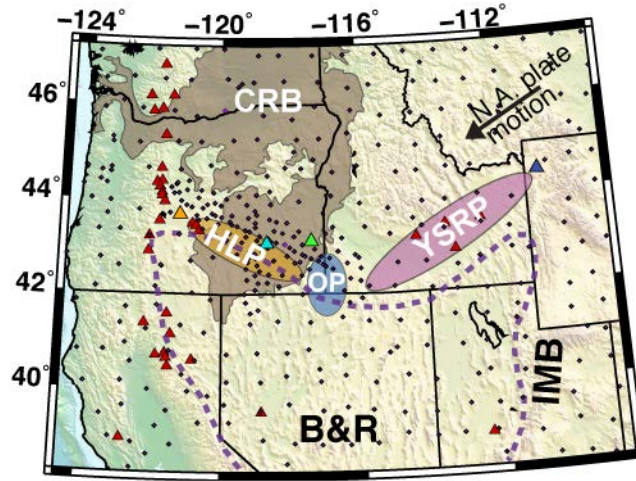


Figure 1. Geology of the study area: Stations shown as black diamonds. Also shown are the locations of the Owyhee Plateau (OP) (blue shaded oval), Yellowstone-Snake River Plains (YSRP) (magenta shaded oval), High Lava Plains volcanic lineament (HLP) (orange shaded oval), Columbia River Basalts (CRB) (brown shaded area) [Camp and Ross, 2004], the boundaries of Basin and Range extension (B&R) (purple dashed line)[Wernicke *et al.*, 1988], Intermountain Belt (IMB), Holocene volcanoes (red triangles), Yellowstone caldera (blue triangle), Newberry caldera (orange triangle), Jordan Craters (green triangle), and Diamond Craters (turquoise triangle).

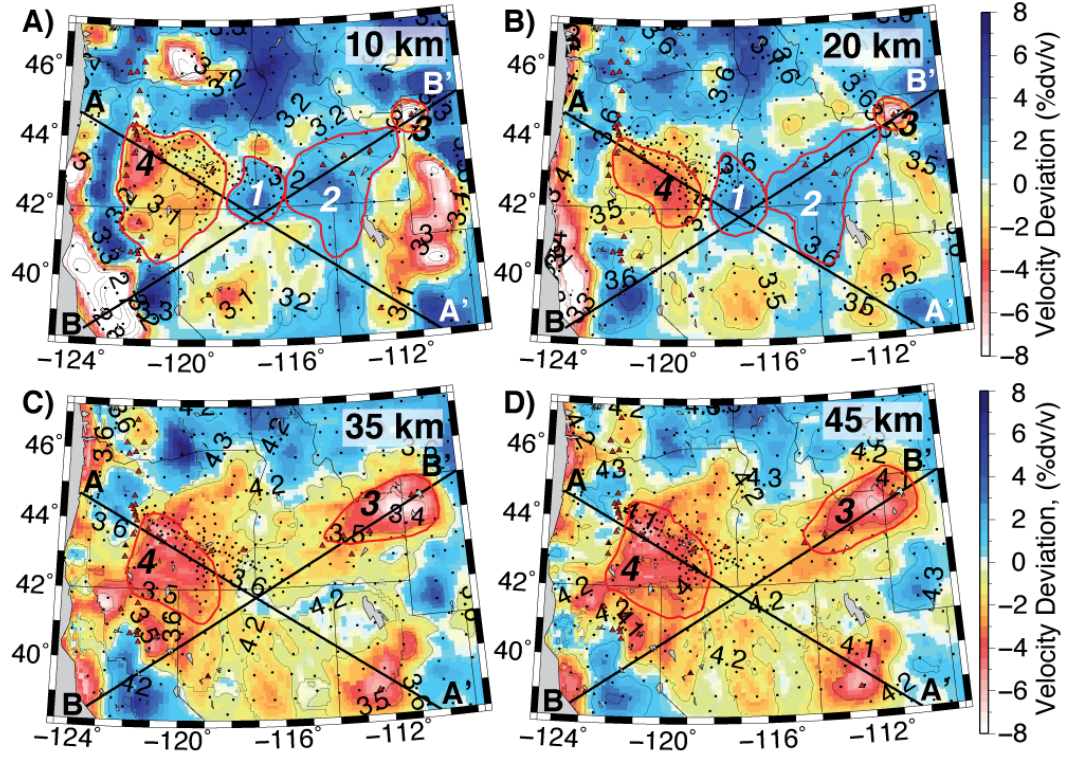


Figure 2. Shear wave velocity deviation maps for: (A) 10km; (B) 20km; (C) 35km; and (D) 45 km depth. Colors indicate deviation from the starting velocity model and contours show absolute velocities in 0.05 km/s increments. The major velocity anomalies are outlined in red and numbered: 1. OP high velocity cylinder, 2. SRP mid-crustal high velocities, 3. Yellowstone low velocities, and 4. HLP low velocities. Locations of cross sections A-A' and B-B' (Figure 3), station locations (black dots), and volcanoes (red triangles) are also plotted.

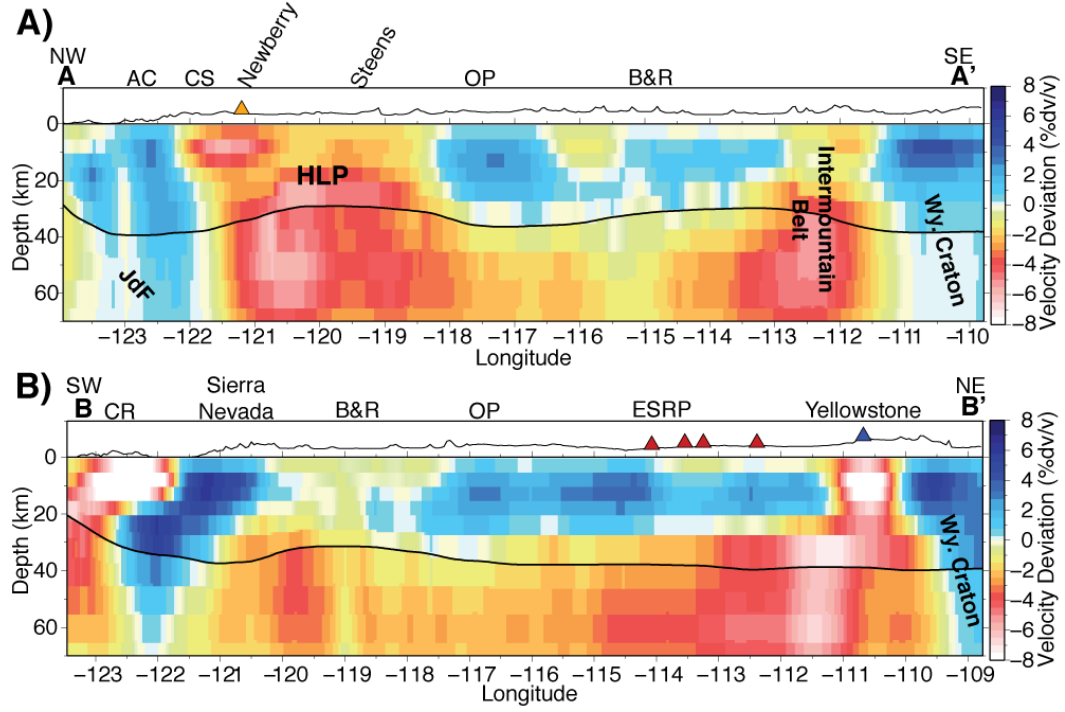


Figure 3. Shear wave velocity deviation cross-sections. Moho depth (thick black line) and topography (thin black line above deviations) are also plotted. Labeled features are the Owyhee Plateau (OP), Yellowstone caldera (blue triangle), Newberry caldera (orange triangle), eastern Snake River Plain (ESRP), Basin and Range province (B&R), high Cascades (CS), ancestral Cascades (AC), Wyoming Craton, Coastal Ranges (CR), northern Sierra Nevada, and Holocene volcanoes of the ESRP (red triangles)

3.13. Auxiliary Materials for Constraints on the causes of the mid-Miocene volcanism in the Pacific Northwest US from ambient noise tomography

Sara Hanson-Hedgecock¹, Lara S. Wagner¹, Matthew J. Fouch², David E. James²

¹ Department of Geological Sciences, University of North Carolina at Chapel Hill, Chapel Hill, NC, United States; ² Department of Terrestrial Magnetism, Carnegie Institution of Washington, Washington, DC, United States

Hanson-Hedgecock, S., L.S. Wagner, M.J. Fouch, and D.E. James (2012), Constraints on the causes of the mid-Miocene volcanism in the Pacific Northwest US from ambient noise tomography, *Geophys. Res. Lett.* doi: 10.1029/2012GLXXXXX

3.14. Introduction:

Included in the auxiliary materials are details of the methods used for determining our shear model, error analyses, and Yellowstone recovery test. Additional figures show results from the inversion for 2-D phase velocities using ambient noise tomography (Figures S1, S2), parameterization of our 1-D shear model and the starting Vs model (Figures S3), shear wave velocity deviation maps at depths not included in the main text (5, 15, 25, 30, 40, 50, 55, 60 km; Figure S4) (65, 70 km; Figure S5) (lower crust and upper mantle; Figure S6), period averaged RMS misfit map (Figure S7), shear model uncertainties (5, 10, 15, 20, 25, 30, 35, and 40 km; Figure S8) (45, 50, 55, 60, 65, and 70 km; Figure S9), Yellowstone anomaly recovery test (Figures S10, S11) and additional cross-sections through the 3-D shear model with location map (Figures S12-S15).

3.15. Text S1 Methods:

3.16. S1.1 Inversion for Shear Velocity and Shear Model Parameterization

The final phase velocity maps at 8, 10, 12, 20, 25, 30, 33 and 40s (Figure S1, S2) are used to invert for the 3-D shear velocity model beneath the HLP and adjoining tectonic provinces. We first calculate the 1-D shear wave velocity model that best fits the average observed phase velocities determined from the final phase velocity maps. The shear velocity, V_s , and density, ρ , for the initial starting model is assigned from IASP91 [Kennett, 1991] and plotted in Figure S3 as the yellow line and stars. The V_p/V_s ratio of the model is kept constant at 1.78, which is set from the previous study of Moschetti *et al.* [2010]. The crust is parameterized with 6 layers of individual thicknesses between 5 and 8km and a total thickness of 35km. The mantle is parameterized with 9 layers that range in thickness between 10 and 50 km (Figure S3). We modify the thickness of each layer so that the corresponding diagonal element of the resolution matrix is greater than 0.1 but less than 0.5. Results of the inversion for the 1-D shear velocity model that best fits the average observed phase velocities are plotted in Figure S3 in magenta dashed lines and squares. The best-fit 1-D shear velocity model contains significantly lower velocities in the upper mantle than the IASP91 model, but is similar to the western United States reference shear velocity model calculated by Moschetti *et al.* [2010].

We used a simplified version of the best-fit 1-D shear model, described above, as the starting model for the many 1-D inversions that go into the final 3-D model. This simplified model and its predicted phase velocities are plotted in Figure S3 as a blue dot-dashed line and hexagons. We adjust the simplified 1-D best-fit shear model for each individual 1-D inversion to account for the Moho depth variations at the grid point in question. We determine the Moho depth at each grid point from a 2-D crustal thickness map made using results from the receiver

function studies of Eagar *et al.*, [2011] for the greater HLP region and is supplemented by the EARS catalogue [Crotwell and Owens, 2005]. Continental crust varies from about ~27 to 42 km in thickness, while oceanic crust remains fixed at 10 km thickness. In an attempt to preserve original layer thicknesses as much as possible, we only change the thickness of the layer in which the new Moho is located and in those layers that are immediately adjacent to the Moho-containing layer. We split the Moho containing layer into two sub-layers, with the sub-layer above the Moho added to the layer above it, and the sub-layer below the Moho added to the layer below it. We divide the layer that the thicker sub-layer was added to in half, which keeps the total number of model layers constant. We assign lower-most crustal velocities to the layers above the new Moho and uppermost mantle velocities to the layers below the new Moho.

Given the new shear velocity starting model at each grid point, we calculate predicted phase velocities using the method of Saito *et al.* [1988], which are then compared to the observed phase velocities determined from the phase velocity maps at each period for each grid point. We use a linearized inversion technique based on the iterative least-squares approach of Tarantola and Valette [1982] to determine the shear velocity model that minimizes the misfit between the observed and predicted phase velocities [see Weerartne *et al.*, 2003]. The 3-D shear wave velocity model is a composite of the 1-D shear wave models at each grid point.

3.17. S1.1.2 Dispersion misfit

We calculate the RMS misfit between the observed phase velocities and those calculated from the shear wave velocity models, averaged over all periods at each grid node (see Figure S7). The average RMS misfit over the entire grid is 0.024km/s with a maximum of 0.088km/s. The largest misfits occur in the Columbia Basin and Coastal Ranges/Great Valley

region of northern California and occur at the shorter periods (<20s) that are most sensitive to crustal structures. The very low velocities in these regions likely results from the thick sedimentary cover in the Columbia Basin and Great Valley and the highly deformed crust of the Coastal Ranges.

3.18. S1.1.3 Shear wave velocity model uncertainty

We evaluate the sensitivity of our shear wave velocity models to small changes in phase velocity by adding small amounts of noise to each of the phase velocities at each point and recalculating the shear wave velocities using these adjusted values. The noise added has a mean of 0 and a standard deviation of $\pm 1\%$ of the observed phase velocity at that period for that grid point. This process is repeated 100 times at each grid point, after which we calculate the standard deviation of the resultant shear wave velocity columns at all depths. Shear velocity uncertainties are plotted in Figure S8 and S9. In general, phase velocity deviations of $\pm 1\%$ produce an average shear velocity uncertainty of ~ 0.02 km/s with a maximum of 0.033 km/s.

3.19. S1.2 Yellowstone Recovery Tests

We perform recovery tests to demonstrate the robustness of our observation that the low velocity anomaly directly beneath Yellowstone extends from the upper mantle to the surface (Figure S10, S11). The input model for the tests is a -8% , $1^\circ \times 1^\circ$ square anomaly located either directly below the Yellowstone caldera (Figure S10) or slightly to the west (Figure S11). Synthetic travel times are calculated and noise, which has the same mean and standard deviation as the observed travel times, is added to the synthetic dataset for each period. Our tests show that the low velocity anomaly is recovered at all periods (10-35s) that sample the mid to lower crustal depths (Figure S10) and that an anomaly placed to the west does not streak laterally under Yellowstone. This shows that when there is a low velocity anomaly directly

beneath Yellowstone we recover it. If there is no low velocity anomaly beneath Yellowstone, but there is a low velocity anomaly to the west of it (as has been previously suggested), that anomaly does not produce a low velocity artifact directly beneath Yellowstone. We therefore conclude that the low velocity anomaly that we observe in the lower crust beneath Yellowstone is a robust result.

3.20. S1.3 References

- Crotwell, H.P., and T.J. Owens, (2005), Automated Receiver Function Processing, *Seismo. Res. Lett.*: Electronic Seismologist November/December.
- Eagar, K.C., M.J. Fouch, D.E. James, and R.L. Carlson, (2011), Crustal structure beneath the High Lava Plains of eastern Oregon and surrounding regions from receiver function analysis, *J. Geophys. Res.*, *116*, B02313, doi:10.1029/2010JB007795.
- Moschetti, M.P., M.H. Ritzwoller, F.-C. Lin, and Y. Yang, (2010). Crustal shear wave velocity structure of the western United States inferred from ambient seismic noise and earthquake data, *J. Geophys. Res.*, *115*, B10306, doi: 10.1029/2010JB007448.
- Kennett, B.L.N., (1991). *IASPEI 1991 Seismological Tables*. Bibliotech, Canberra, Australia.
- Saito, M., (1988), DISPER80: A subroutine package for the calculation of seismic normal-model solutions, in *Seismological Algorithms*, pp. 293-319, ed. Doornbos, D.J., Academic Press, New York.
- Tarantola, A., and B. Valette, (1982), Generalized non-linear problems solved using the least-squares criterion, *Rev. Geophys. Sp. Phys.*, *20*, 219-232.
- Weeraratne, D.S., D.W. Forsyth, K.M. Fischer, and A.A. Nyblade, (2003), Evidence for an upper mantle plume beneath the Tanzanian craton from Rayleigh wave tomography, *J. Geophys. Res.*, *108*, 2427, doi: 688 10.1029/2002JB002273.

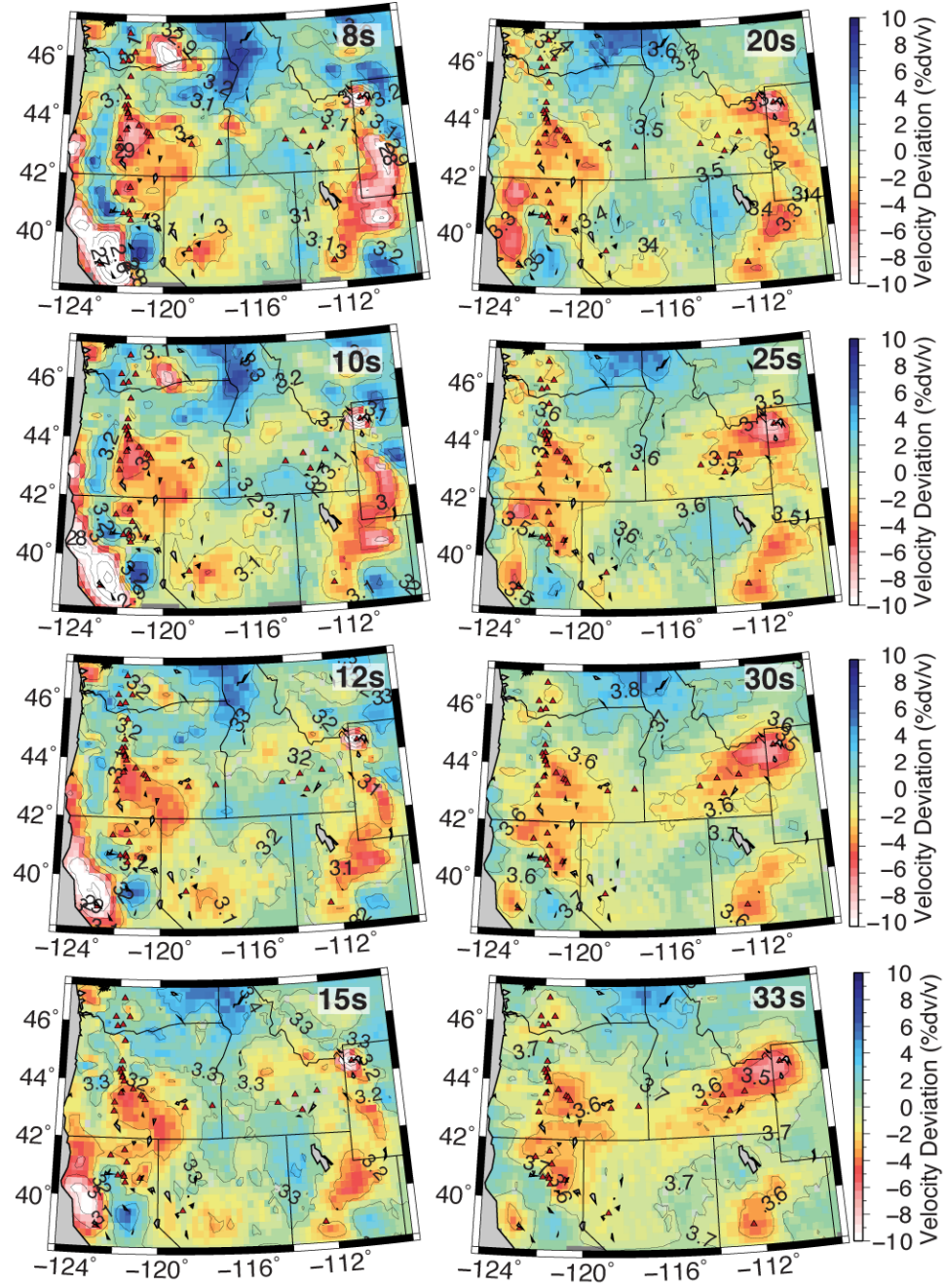


Figure S1. 2-D phase velocity maps at 8, 10, 12, 15, 20, 25, 30, and 33s determined using ambient noise tomography. The colors show deviations from the starting phase velocity and contours show absolute phase velocity in 0.1 km/s increments. Holocene volcanoes are represented by red triangles.

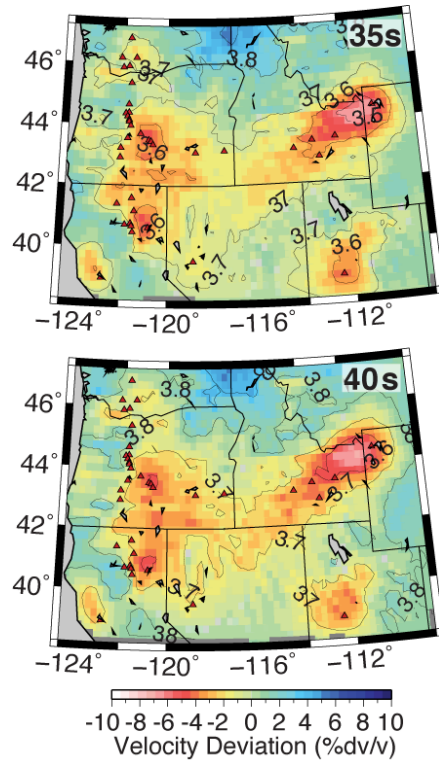


Figure S2. 2-D phase velocity maps at 35, and 40s. Annotation is the same as for Figure S1.

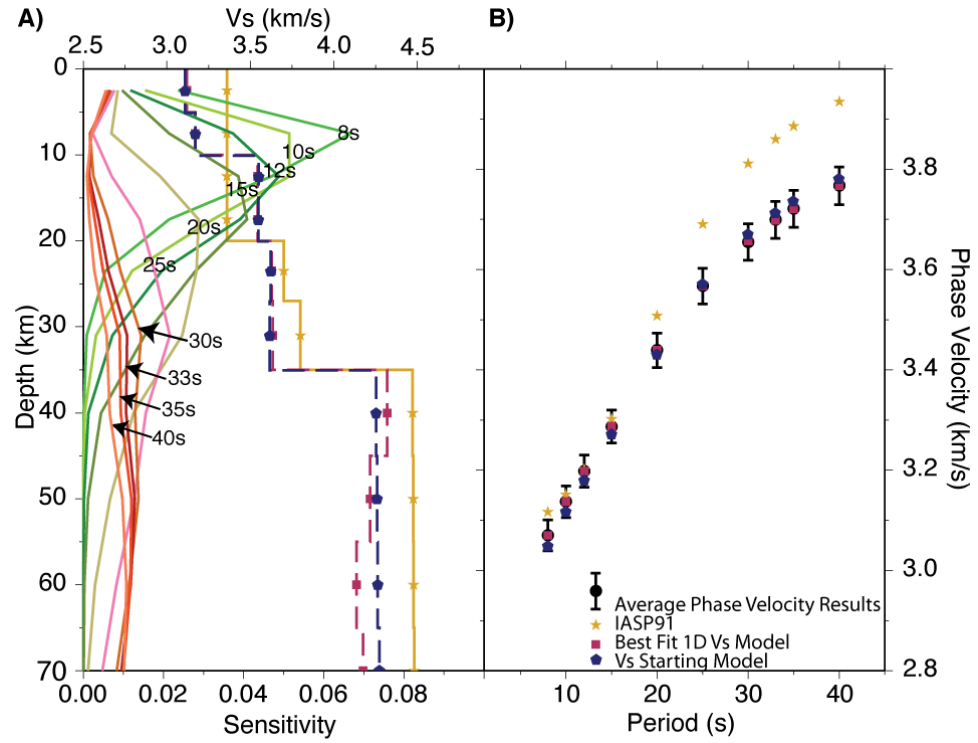


Figure S3. Results of the 1-D best fit shear inversion. A) The multi-colored lines with black labels show the sensitivity kernels to shear wave structure as a function of depth for the periods used in this study (8s-40s). The IASP91 shear wave model (yellow line and stars), best fit 1-D shear model (magenta dashed line and squares), and simplified 1-D starting model (blue dot-dashed line and hexagons) are plotted. B) Dispersion curves are plotted for the average phase velocities across the study area with error bars showing the standard error (black dots and error bars), IASP91 predicted phase velocities (yellow stars), best fit 1-D simplified shear model (magenta squares), and predicted phase velocities for the starting model (blue hexagons).

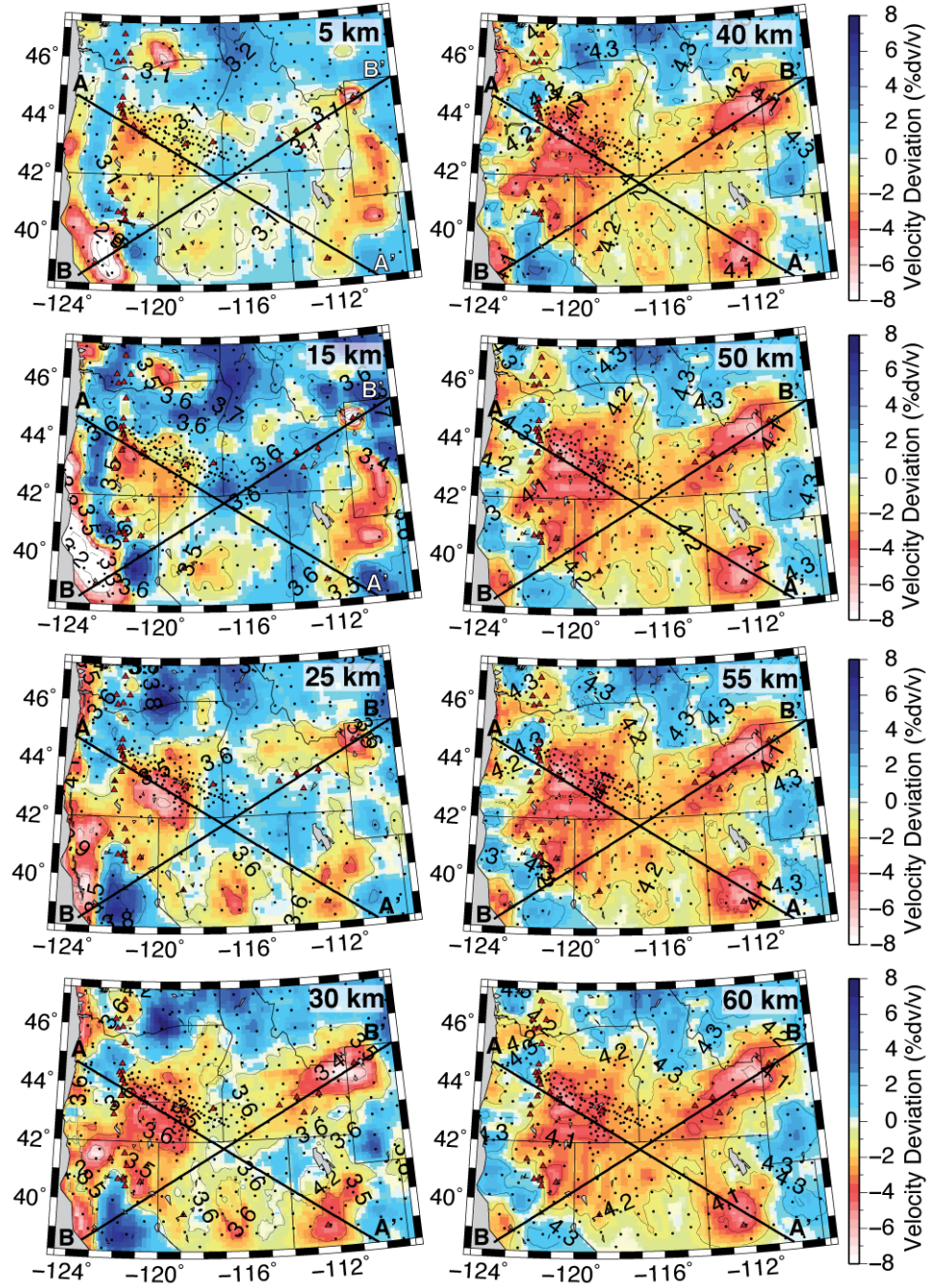


Figure S4. Shear wave velocity deviation maps for 5, 15, 25, 30, 40, 50, 55, and 60 km depths. Colors indicate deviation from the starting velocity model and contours show absolute velocities in 0.1km/s increments. Locations of cross sections A-A' and B-B' (Figure 3), station locations (black dots), and volcanoes (red triangles) are also plotted.

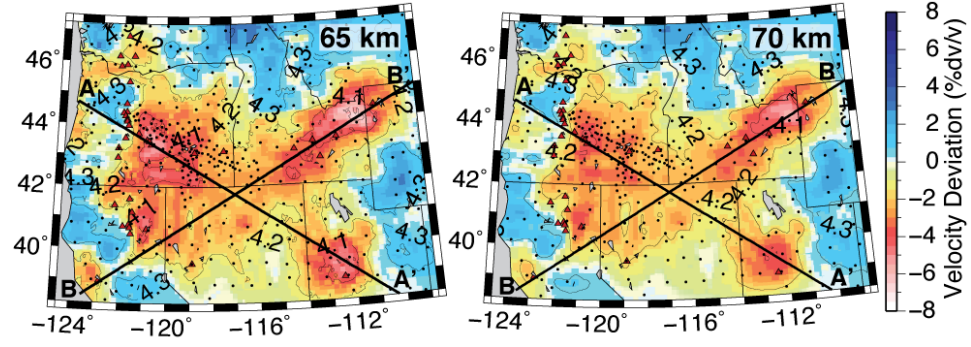


Figure S5. Shear wave velocity deviation maps for 65 and 70 km depths. Annotation is the same as for Figure S4.

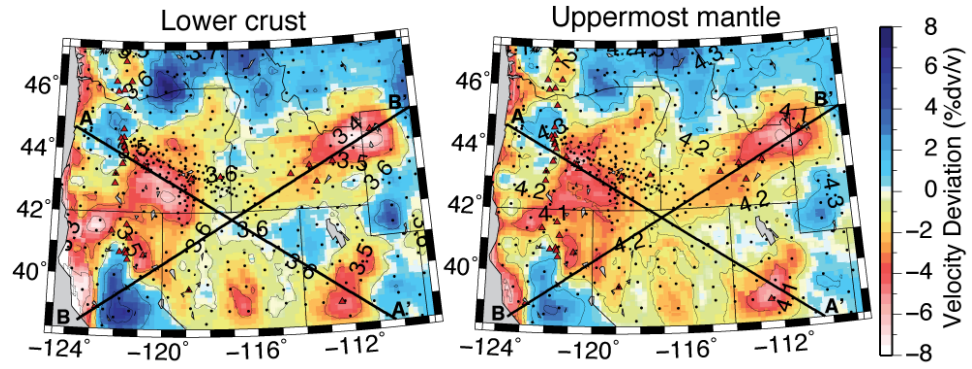


Figure S6. Shear wave velocity deviation maps in the lower crust, just above the Moho, and uppermost mantle, just below the Moho (depth is variable). Annotation is the same as for Figure S4.

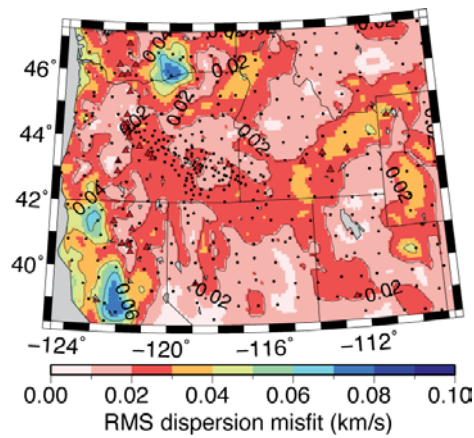


Figure S7. Period averaged misfit map shows the RMS misfit (km/s) between the observed phase velocities and predicted phase velocities computed from the 3-D V_s model. Most of the study area has an RMS misfit of 0.03 km/s or less.

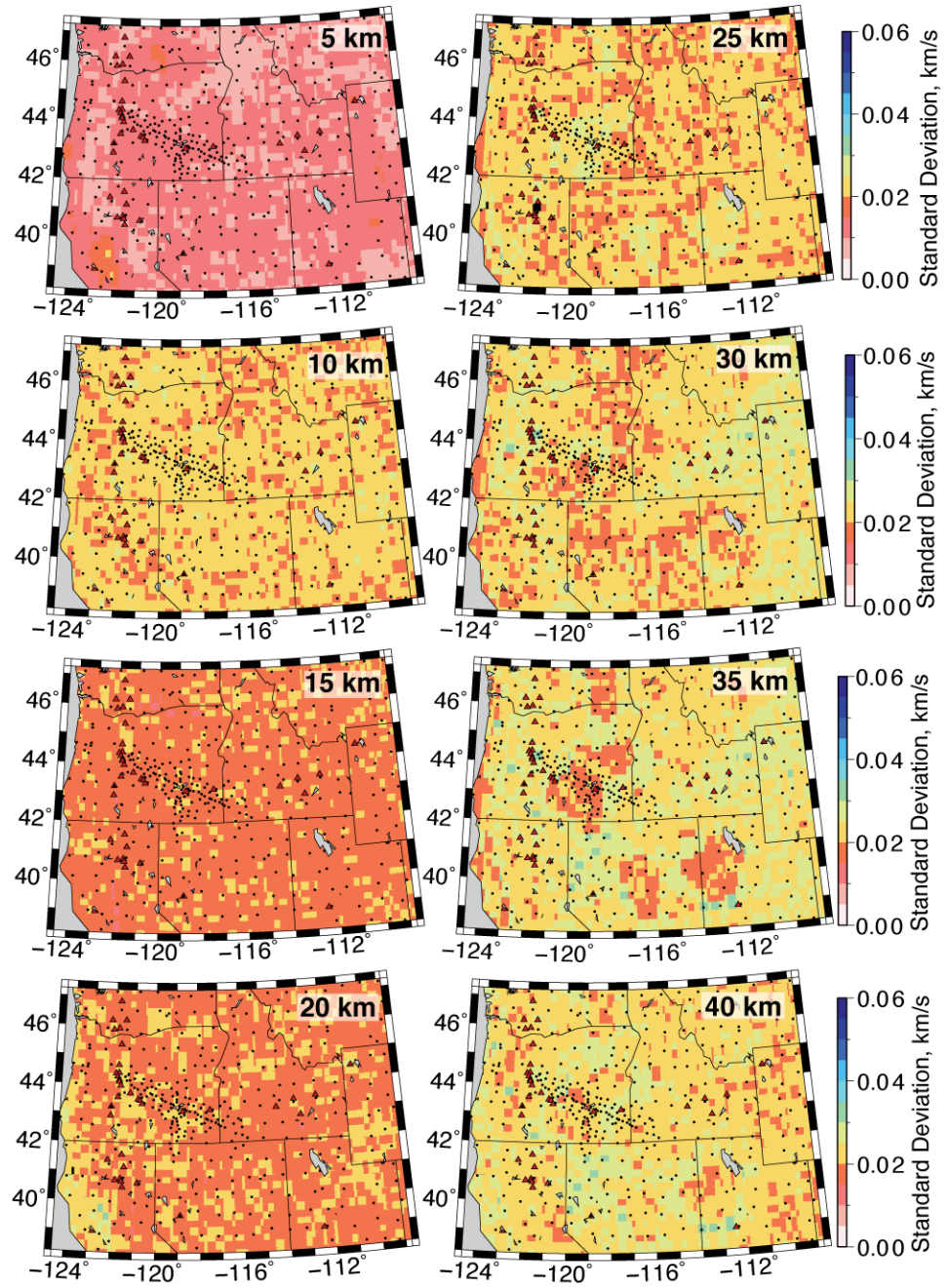


Figure S8. Shear velocity model standard deviations at 5, 10, 15, 20, 25, 30, 35, and 40 km depths.

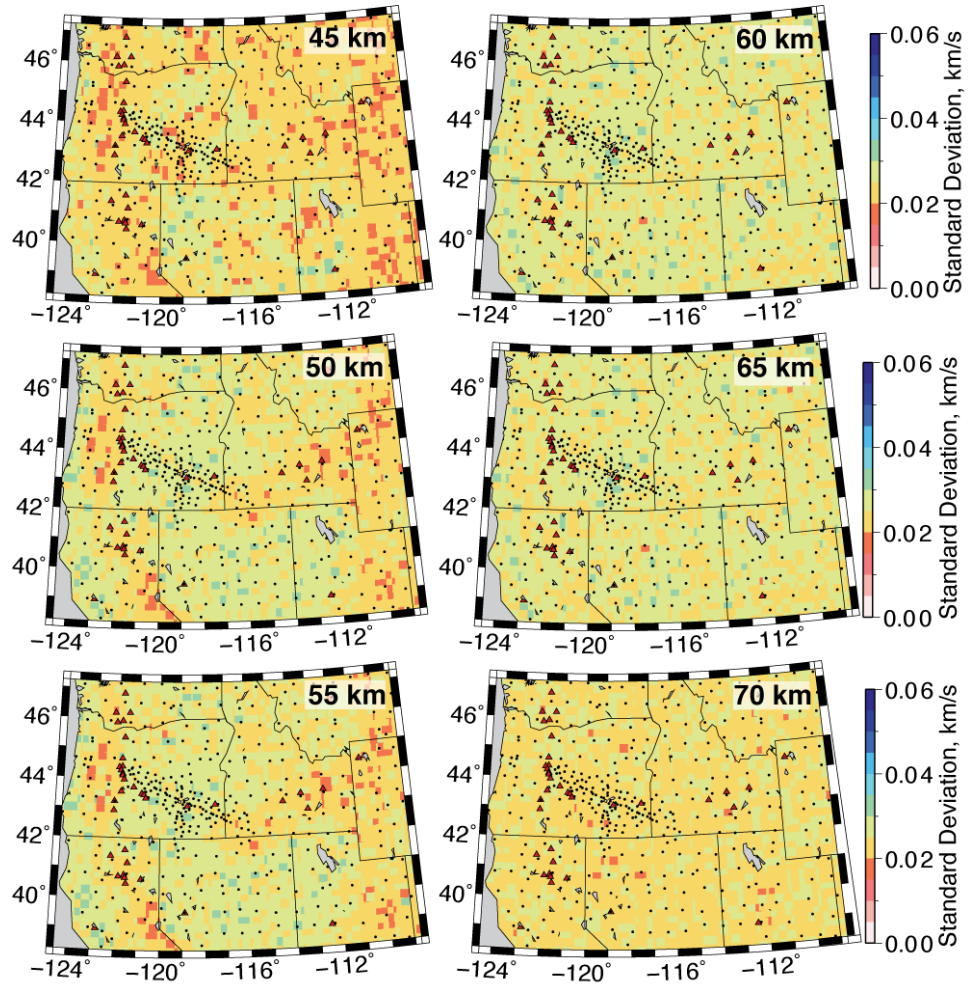


Figure S9. Shear velocity model standard deviations at 45, 50, 55, 60, 65, and 70 km depths.

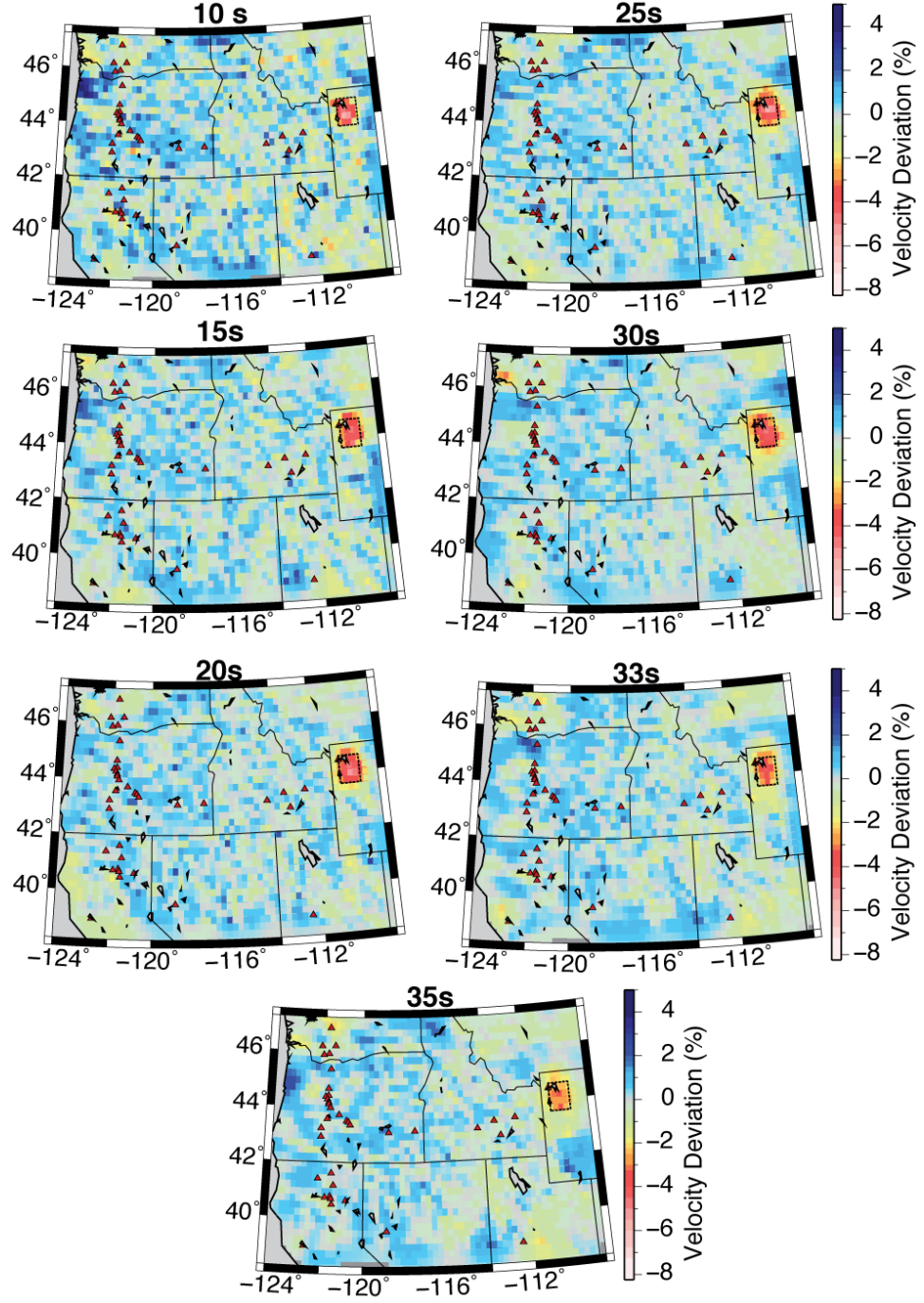


Figure S10. Recovered anomalies from the Yellowstone low velocity anomaly recovery tests: -8%, $1^\circ \times 1^\circ$ anomaly directly under the Yellowstone caldera. The dashed box shows the outline of the original anomaly and the colors show deviations from the starting phase velocity. The low velocity anomaly is recovered at all periods.

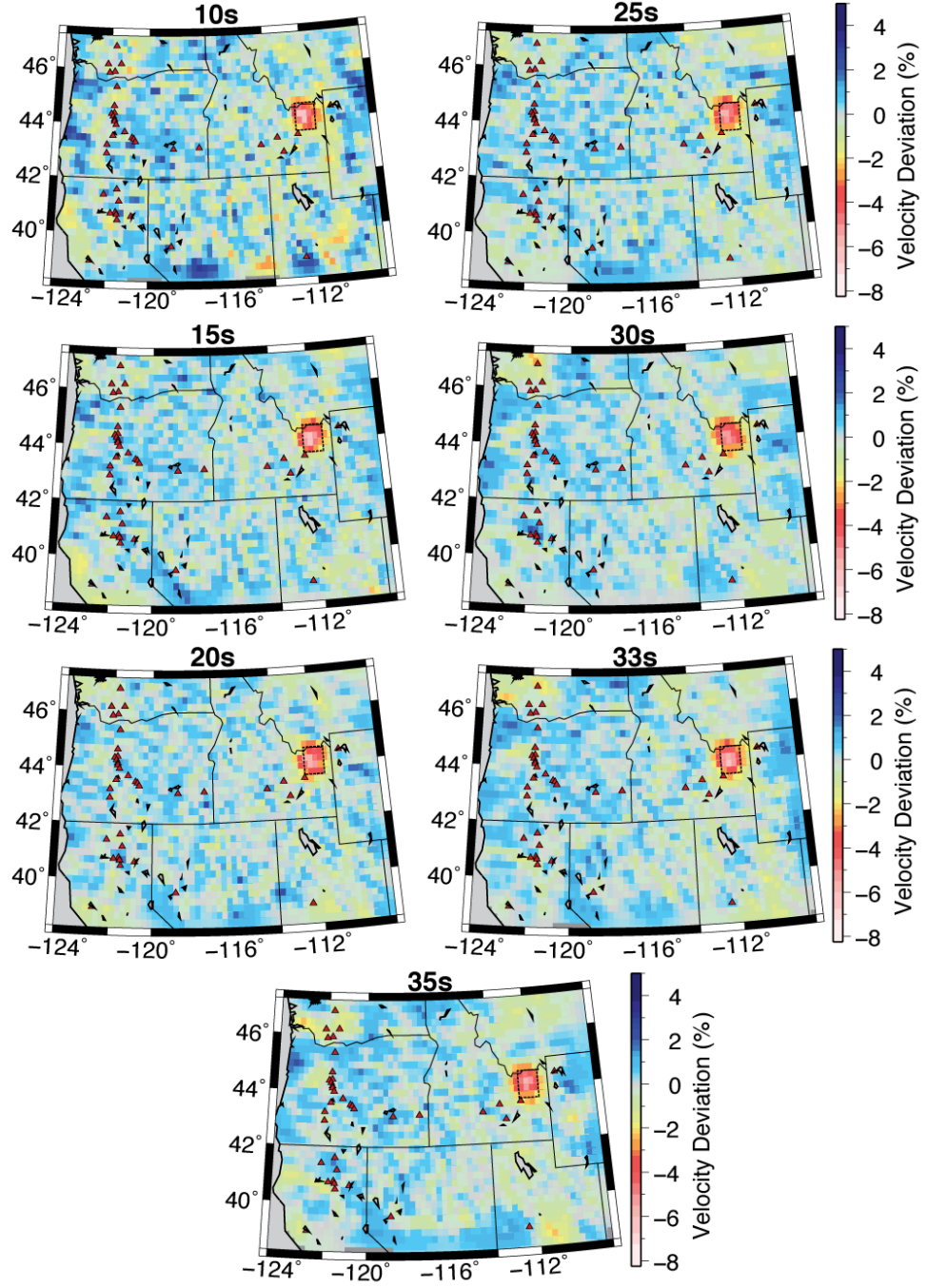


Figure S11. Recovered anomalies from the Yellowstone low velocity anomaly recovery tests: -8%, $1^\circ \times 1^\circ$ anomaly to the west of Yellowstone caldera, under the Snake River Plain. Annotation is the same as for Figure S9. The low velocity anomaly is recovered at all periods.

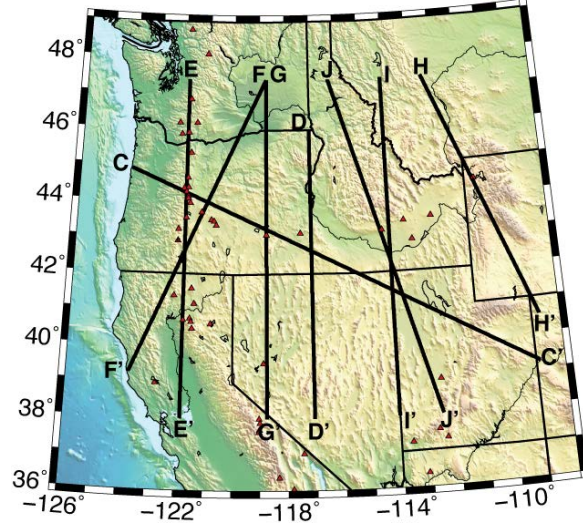


Figure S12. Locations of additional shear wave velocity cross-sections in Figures S13-S15.

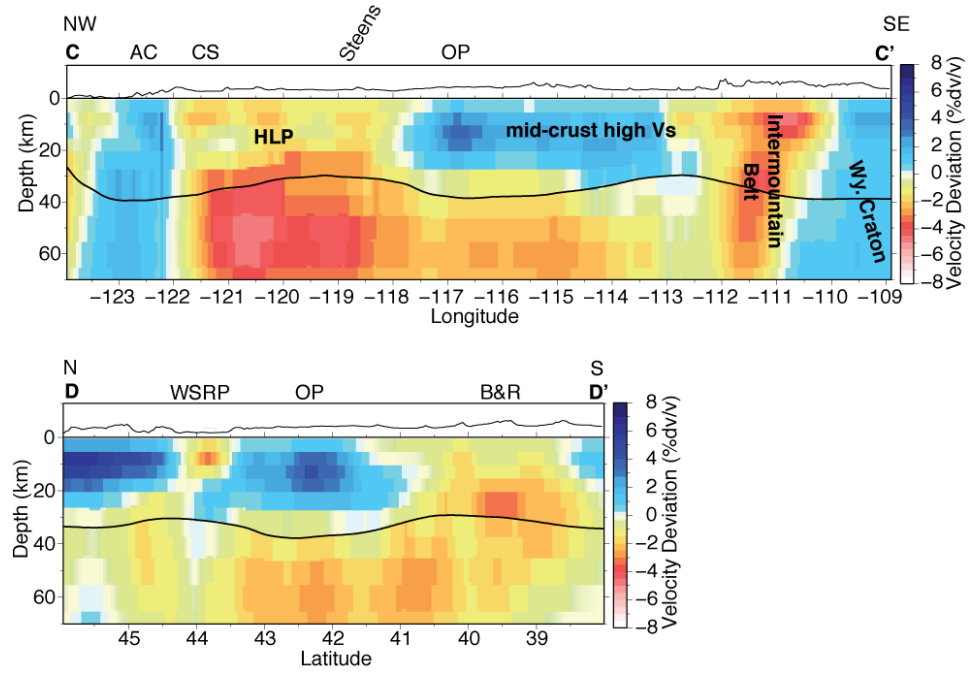


Figure S13. Shear wave velocity deviation cross-sections, C-C' and D-D'. C-C' is NW-SE along the highest density line of the High Lava Plains experiment and D-D' is N-S through the Owyhee Plateau. The Moho depth (thick black line) and topography (thin black line above deviations) are also plotted. Noted features are the High Lava Plains (HLP), Owyhee Plateau (OP), Basin and Range province (B&R), high Cascades (CS), ancestral Cascades (AC), Wyoming Craton, western Snake River Plain (WSRP), Steens Mountain, and Intermountain Belt.

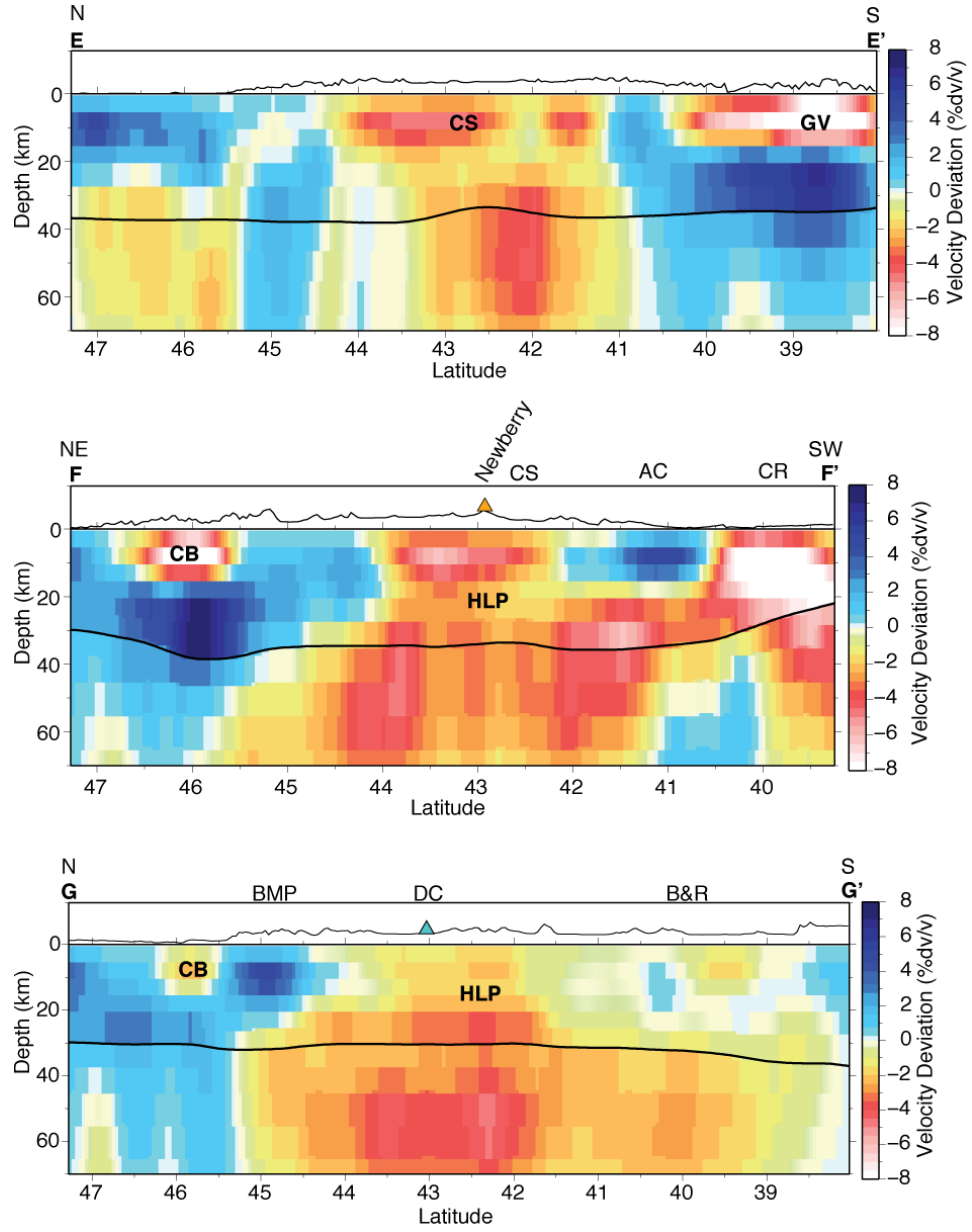


Figure S14. Shear wave velocity deviation cross-sections through the High Lava Plains: E-E', F-F', and G-G'. The Moho depth (thick black line) and topography (thin black line above deviations) are also plotted. Noted features are the High Lava Plains (HLP), high Cascades (CS), ancestral Cascades (AC), Great Valley (GV), Coastal Ranges (CR), Columbia Basin (CB), Blue Mountain Province (BMP), Basin and Range province (B&R), and Diamond Craters (turquoise triangle).

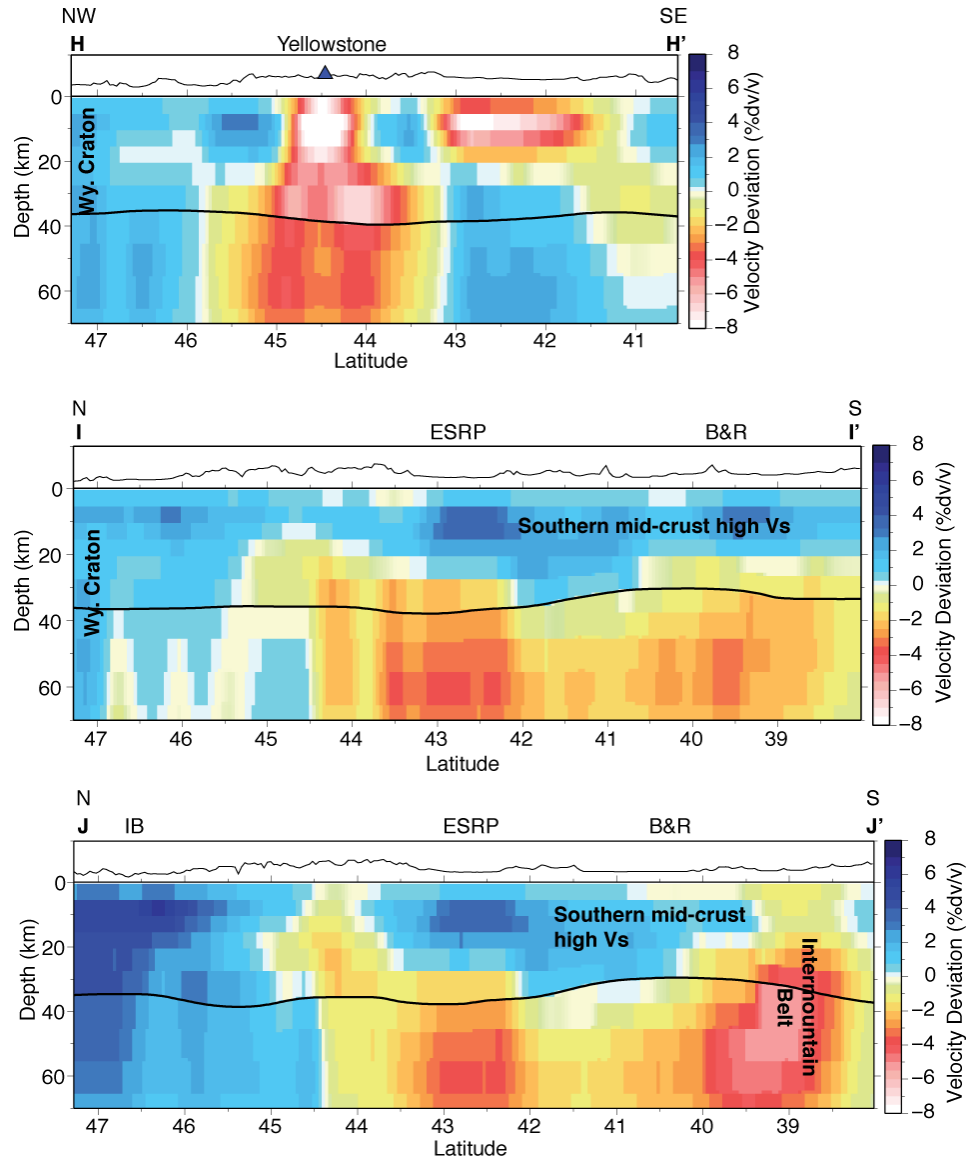


Figure S15. Shear wave velocity deviation cross-sections through the Yellowstone-Snake River Plain; H-H', I-I', and J-J'. The Moho depth (thick black line) and topography (thin black line above deviations) are also plotted. Noted features are the Yellowstone caldera (blue triangle), Wyoming Craton, eastern Snake River Plain (ESRP), Basin and Range province (B&R), Intermountain Belt, and the southernmost extent of the mid-crustal high velocity anomaly.

Chapter 4

VELOCITY CHANGES ASSOCIATED WITH PERIODS OF INCREASED ERUPTIVE ACTIVITY AT TUNGURAHUA VOLCANO, ECUADOR IN 2010, DETERMINED FROM NOISE INTERFEROMETRY

4. Introduction

I present the results of measuring velocity changes associated with three episodes of increased eruptive activity at Tungurahua in 2010 using ambient noise correlations. Tungurahua volcano was one of the most active volcanoes in the Ecuadorian Andes. Eruptions since 1999 have generated Strombolian and Vulcanian style volcanic activity that pose a threat to ~25,000 people living in the towns (including Baños) that surround the volcano, as well as the Agoyan hydroelectric dam. During 2010 Tungurahua experienced three episodes of heightened eruptive activity in (1) January to early March, (2) Late May to June 18th paroxysmal crisis with continued moderate activity through July, and (3) mid-November to December. Following standard procedures, ambient noise correlations were calculated from daily, 0.5-4Hz bandpass filtered, continuous seismic records at 5 broad-band seismometers, deployed around the flanks of Tungurahua by the Instituto Geofísico Escuela Politécnica Nacional (IGEPN). Using the dilation correlation coefficient (stretching) method [Lobkis and Weaver, 2003; Hadziioannou *et al.*, 2009, 2011; Weaver *et al.* 2011] the homogenous relative velocity change, dV/V , was calculated that maximizes the cross-correlation coefficient between each daily correlation function and a reference function composed of the 1 year-long stack of the daily correlations. During the three eruptive episodes of 2010, a drop in the relative velocity

was observed of ~0.51%, 0.53%, and 0.49%, respectively. These values were greater than the calculated root mean square of the erroneous relative dilation, $\text{RMS } \varepsilon = 0.15\%$. The observed drop in relative velocity began at the onset of eruption, decreases gradually, and began to recover as eruptive activity decreased. The correspondence of decreased velocity with increased eruptive activity suggests a source that was directly related to eruption processes, e.g., fracturing and dilation due to pressurization in the magmatic/hydrothermal system, shallowing of fragmentation depth, or deepening of the exsolution depth.

4.1. Background: Monitoring Volcanoes Using Relative Velocity Changes

Continuous monitoring of hazardous active volcanos is important to giving adequate warning and mitigating the risk from eruptions and other volcanic hazards to the populations surrounding an erupting volcano. One such dangerous volcano, erupting intermittently since 1999, was Tungurahua in Ecuador. Its hazards that directly threaten the ~25,000 people living in towns, including the tourist town of Baños, that surround the volcano, as well as pose a risk to the Agoyan hydroelectric dam include pyroclastic flows, lava flows, lahars, tephra and ash falls and avalanches (Figure 7). Although infrequent, sector collapses have occurred during Tungurahua's geologic history and remain a hazard of indeterminate risk. The volcano is continuously monitored by the IGEPN using a network of instruments to record seismicity, tilt, and gas emissions that augments the visual observations of local volunteers and IGEPN staff.



Figure 7. Hazards of Tungurahua Volcano. (Top left) Ash and pumice fall deposit buries a cinderblock house; (Top right) Pyroclastic flow field; (Bottom left) Avalanche and lahar channel cutting through ash, pumice and pyroclastic flow deposits; (Bottom right) Ash plume expelled by Tungurahua (hidden by the white clouds) in July 2009. (Source: S. E. Hanson-Hedgecock)

Previous studies have measured the temporal changes in relative velocity using low frequency ambient noise, below 0.5 Hz, with multiplet earthquakes at volcanoes [Ratdomopurbo and Poupinet, 1995; Sabra *et al.*, 2006; Sens-Schönfelder and Wegler, 2006; Wegler *et al.*, 2006; Duputel *et al.*, 2009; Brenguier *et al.*, 2008a; Haney *et al.*, 2009; Battaglia

et al, 2012] and active fault zones [Poupinet 1984; Nishimura *et al.*, 2000; Wegler and Sens-Schönfelder, 2007; Brenguier et al, 2008b; Meier *et al.*, 2010; Hadziioannou *et al.*, 2009; Weaver *et al.*, 2012]. Multiplets, earthquakes with similar locations and waveforms, but occurring at different times, has been used to measure relative velocity changes prior the volcanic eruptions at Mt. Merapi [Ratdomopurbo and Poupinet, 1995; Wegler *et al.*, 2006]. Ratdomopurbo and Poupinet, [1995] measured a decrease in shear velocity, while Wegler *et al.* [2006] observed a small increase in velocity correlated to pre-eruptive seismicity and dome growth. Both observations were attributed to pressure changes in the volcano [Ratdomopurbo and Poupinet, 1995; Wegler *et al.*, 2006]. The use of discrete sources from individual earthquake coda and airgun shots limited the length of time that observations can be made and resolution of measurements in these previous studies.

Measuring relative velocity changes using continuous ambient noise correlations can improve the duration of observations and increase the temporal resolution of on the order of once a day. Sens-Schönfelder and Wegler [2006] used ambient noise correlations to determine daily velocity changes at Mt. Merapi volcano from August 1997 to June 1999. They observed long term changes in relative velocity that correlated to fluctuating ground water level caused by changes in the amount of precipitation [Sens-Schönfelder and Wegler, 2006]. This seasonal trend obscured any changes due to volcanic activity. Long term seasonal trends were also observed in the Los Angeles basin [Meier *et al.*, 2010] and at Piton de la Fournaise volcano [Brenguier *et al.*, 2008b].

Brenguier *et al.* [2008b] was able to observe velocity changes, measured from ambient noise correlations that corresponded to eruptive activity after removing the seasonal trend. Using 10-day stacks of ambient noise correlations he observed a drop in relative velocity on the

order of 0.1% preceding eruptive periods [Brenguier *et al.*, 2008b]. These decreases are interpreted as dilations of the edifice resulting from magma intrusion [Brenguier *et al.*, 2008b]. This is similar to the dilatancy hypothesis of earthquakes, which proposed that fracturing of the rocks around a fault zone can result in drops in V_p/V_s prior to earthquake rupture [Nur, 1973; Scholz *et al.*, 1973]. Unfortunately, the limited resolution of 10 day stacks has the effect of shifting the start of the apparent velocity changes in time. Baig *et al.* [2009] improved the temporal resolution of relative velocity measurements from 10 days to 1 day by applying an adaptive filter to enhance the signal-to-noise ratio of the noise correlations and did not observe any precursory decrease in relative velocity, using the same dataset as Brenguier *et al.* [2008].

Both Brenguier *et al.* [2008b] and Baig *et al.* [2009] determined relative velocity from measuring the time shift of coherent arrivals in the ambient noise correlation function. Alternatively, the dilation correlation coefficient method (DCC) [Lobkis and Weaver, 2003; Sens-Schönfelder and Wegler, 2006; Hadziioannou *et al.*, 2009, 2011; Weaver *et al.* 2011] has been shown to improve measurements of relative velocity changes from fluctuating (noisy) waveforms with low signal-to-noise ratios [Hadziioannou *et al.*, 2009]. This method measures the relative dilation of separate waveforms resulting from changes in velocity and allows one to accurately calculate small velocity changes using finer using shorter lengths of time (1 day versus 10 days) can be used to determine velocity changes. The relative velocity changes associated with three episodes of increased eruptive activity at Tungurahua volcano, Ecuador, for 2010 were determined by applying this method to correlation functions calculated from 6 hours of continuous ambient noise.

4.2. Geologic Setting of Tungurahua Volcano

Tungurahua Volcano (1.45°S, 78.43°W), located in the eastern Andes of Ecuador, is one of the most active volcanoes in the Ecuadorian Andes. It is composed of three volcanic edifices (called Tungurahua I, II, and III) built on the Paleozoic-Cretaceous metamorphic basement of the Eastern Cordillera [Hall *et al.*, 1999]. The remnant flanks of Tungurahua I, composed of dacite to andesite lava flows and interbedded tephra, are found on the north, south, and east flanks of the current edifice. Tungurahua I appears to have been partially destroyed by a sector collapse that deposited thick units of andesitic avalanche breccia deposits that were observed in the Ulba valley to the NW and in several anomalous hills at the base of the western flank of the volcano. The intermediate cone, Tungurahua II, appears to be composed of andesite lava flows younger than 14,000 years BP, which were exposed on the upper southern flanks. Tungurahua II was partially destroyed by a sector collapse, approximately 2955±90 years ago, on its western flank that produced a ~8 km³ debris flow filling the Chambo River valley. The extent of this collapse can be seen in the smooth fan like shape of the western flank, which is distinct from the topographically rougher, stream channel incised remnants of Tungurahua I and II on the south, east and north flanks. Subsequent frequent eruptions, producing tephra falls, pyroclastic flows, lava and debris flows, have infilled the collapse scarp and formed the current edifice, Tungurahua III. Tungurahua III has been growing for the last ~2300 years and has rebuilt approximately 50% of the volume of the previous cone, Tungurahua II, at an estimated rate of ~1.5×10⁶ m³ per year.

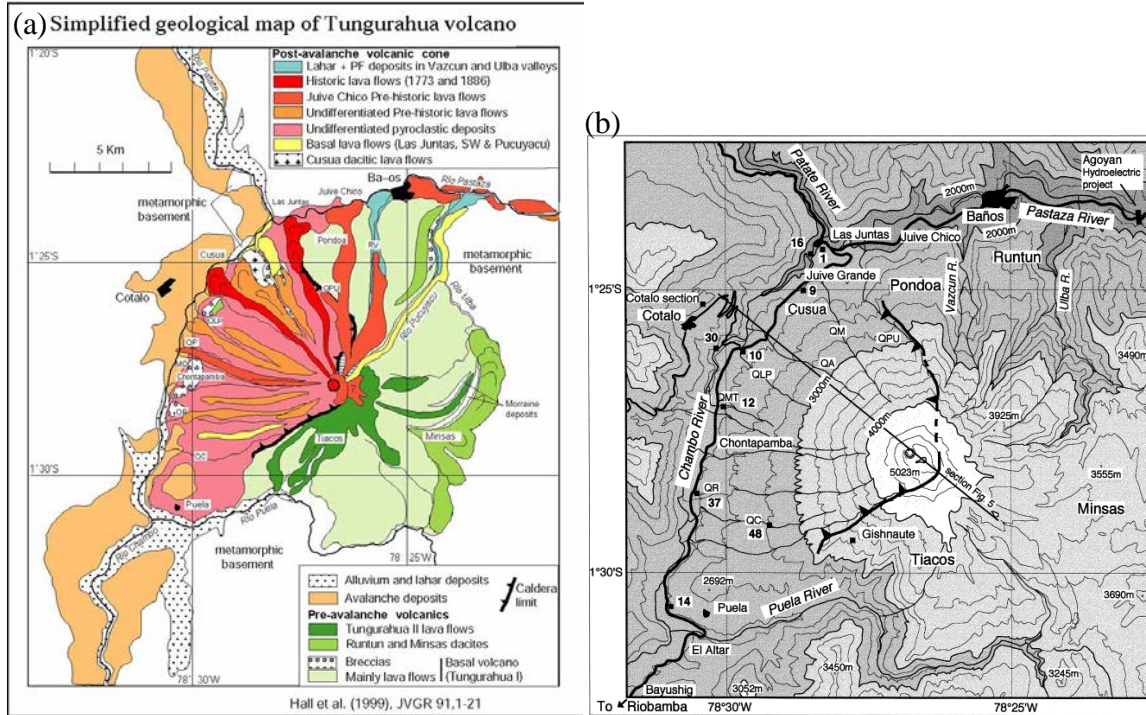


Figure 8. (a) Simplified geologic map and (b) contour map of Tungurahua Volcano. Marked features include the Tungurahua II avalanche scarp (bold line with teeth), QA, Quebrada Achupashal; QC, Quebrada Confesionario; QM, Quebrada Mandur; QMT, Quebrada Motilones; QLP, Quebrada La Piramide; QPU, Quebrada Palma Urcu; QR, Quebrada Rea, [source: Hall *et al.*, 1999]

4.3. Eruptive Episodes at Tungurahua in 2010

Since August 1999, Tungurahua has experienced numerous periodic episodes of eruptive activity. These eruptions generate Strombolian and Vulcanian style volcanic activity that pose a threat to the ~25,000 people living in the towns (including Baños) surrounding the volcano, as well as the Agoyan hydroelectric dam [Hall *et al.*, 1999, 2008]. In 2010, Tungurahua experienced 3 major episodes of eruptive activity during (1) January to March 2010, (2) late May to June 18th paroxysmal crisis with continued moderate activity through July, and (3) mid-November to December 2010.

The first episode began on around January 5-6, 2010, when a gas and ash plume was observed rising to an elevation of ~6.5 km a.s.l. This was followed by an increase in the

duration and amplitude of volcanic tremor and number of explosions that produced ash falls and other ejecta. Volcanic activity during January was characterized by eruptions that produced ash plumes and falls, as well as some Strombolian activity (January 18-23) that ejected incandescent blocks, ash plumes, and lava fountaining. In February eruptions produced ash falls and plumes, rising to an elevation of between 7-8km a.s.l., small pyroclastic flows on the N and NNW flanks (February 11), and in addition to small lahars, the occasional Strombolian eruption of incandescent material. Activity decreased markedly in late February and into March, with the last reported ash fall occurring on March 19th. [IGEPN, 2010; Venzke *et al.*, 2012]

Prior to the onset of the first episode, an increase in the number of recorded earthquakes was observed in December 2009. The number of long period (LP) earthquakes increased from 3 in the first week of December to 21 in the last week of December, reached a maximum of 310 recorded in the second week of February and decreased to 25 recorded in the last week of March. The number of long period (LP) earthquakes increased from 3 in the first week of December to 21 in the last week of December, reached a maximum of 310 recorded in the second week of February and decreased to 25 recorded in the last week of March. [IGEPN, 2010; Venzke *et al.*, 2012]

The second and most intense episode of activity began May 26-28, 2010, after ~10 weeks of relative quiescence. A strong explosion on May 26, 2010 06:12 CST produced small pyroclastic flows on the N, W, and SW flanks; an ash plume that reached an altitude of 12km a.s.l.; and ash fall on the S and SW flanks. A larger eruption on May 28, 08:47 CST produced an ash plume that reached an altitude of 15km a.s.l. The ash fall was heavy and affected a wide area, reaching as far as Guayaquil, Ecuador (180km SW). Locally pumice fell as far as 6-8km

and pyroclastic flows were produced that travelled about 3km from the summit on the NW, W, and SW flanks Tungurahua. Eruptive activity was produced by plumes of ash and gas, lava fountaining, explosions of incandescent rock and some small pyroclastic flows. This intense activity continued into the beginning of June reaching its peak around June 8-9. On June 8 the maximum measured SO₂ released was 4030 tons. Volcanic activity continued at a moderate level during July, ending in the first few days of August. Eruptive activity was characterized by Strombolian style explosions, steam and ash plumes reaching altitudes of between 1.5 to 8km a.s.l. and ash falls that primarily affected the local population around Tungurahua. On July 27th a series of explosions were recorded by the seismic network and ash fall in the surrounding area was also reported. The last reported plume of steam and ash occurred on July 30th. [IGEPN, 2010; Venzke *et al.*, 2012]

The last episode of major eruptive activity in 2010 began with a gradual increase in seismic activity at the end of October followed by vulcanian style eruptions beginning in the second week of November. Fumarolic and emissions of gas characterized eruptive activity of Tungurahua during the first week of November. Small eruptions of ash and gas were reported from November 13 until November 22, when activity increased sharply. In the afternoon of November 22 vulcanian style explosions ejected incandescent blocks, that fell as far as 4km below the summit, and an ash plume that reached altitudes of 11-12km a.s.l.. Strombolian activity ejected incandescent blocks, November 25-26, 28-29; and December 2-8. December 4th marked an increase in the number and intensity of explosions that produced ash fall, pyroclastic flows down the N and W flank, and a lava flow that travelled down the La Hacienda quebrada for about 1 km. This lava flow was only the second reported since the beginning of activity in 1999; the previous one occurred in August 2006 and descended the

Cusúa quebrada on the northwestern flank on Tungurahua. After moderate size explosions December 24-25 that produced ash plumes and blocks, eruptive activity at Tungurahua decreased and explosions ceased by the end of the first week on January 2011. [IGEPN, 2010; Venzke *et al.*, 2012]

Chapter 5

METHODS

5. Data

Continuous seismic time-series records from 5 broad-band seismometers during 2010, deployed around the flanks of Tungurahua volcano, Ecuador by the Instituto Geofísico Escuela Politécnica Nacional (IGEPN), were used (Figure 9). Reftek digitizers recording at a sample rate of 50Hz, were deployed with Guralp CMG-40T seismometer (band sensitivity 0.03 Hz-50Hz) at 5 sites (clockwise from north BRUN, BULB, BPAT, BMAS, and BBIL). The array dimensions were approximately 11 km (N-S) by 8.5 km (E-W) and the maximum interstation spacing was 11 km and the minimum spacing was 2.8 km.

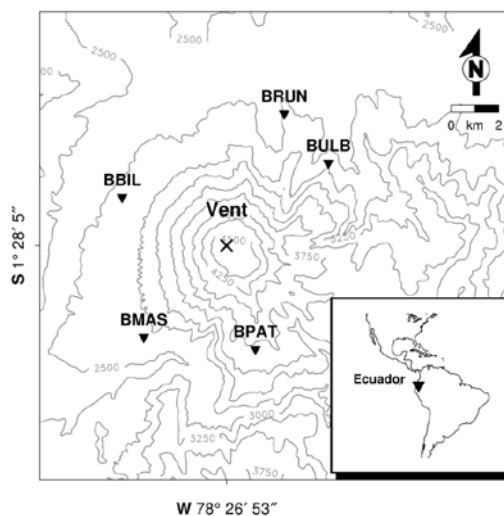


Figure 9. Map of station locations for the IGEPN broadband seismic array at Tungurahua Volcano, Ecuador deployed in 2010. Topographic contour spacing is every 50 meters. (Source: Keehoon Kim)

5.1. Calculation of noise correlation functions (CFs)

Processing the ambient noise recordings to calculate the noise correlation functions was done following the basic procedures of Bensen *et al.* [2007]. Processing the ambient noise data was a three step process: (1) Preliminary processing of individual station records to enhance the noise signal and remove earthquake signals and instrumental irregularities, (2) cross-correlation of station pairs and auto-correlation of each station for each 6-hour long preprocessed ambient noise record, followed by and (3) stacking of the individual correlation functions for each station and station pairs.

In the preliminary processing, each daily seismic record demeaned and detrended and band-passed filtered from 0.5-4 Hz. This higher frequency filtering allowed for the recovery of the local, shallow (<15km) structure of Tungurahua rather than regional structures recovered using the microseism bands (0.025-0.5Hz). To reduce the effect of earthquakes that could mask the ambient noise signal, a running-absolute-mean normalization was applied that weights the waveform by the inverse of the running average of the absolute value of the waveform amplitude in a normalization time window of fixed length equal to one half the maximum period of the data [Bensen *et al.*, 2007]. Any remaining coherent phases were removed by applying sign-bit normalization to each day long record. In the frequency band used, spectral whitening had the effect of introducing additional incoherent noise into the correlation functions and was not applied to the noise records. Each day long record was cut into 6-hour sections prior to correlation.

For each 6-hour vertical component (Z) record, 5 auto-correlation functions, for each individual station (BBIL, BMAS, BPAT, BULB, BRUN), (Figure 10-Figure 14) and 10 cross-correlation functions (Figure 15-Figure 24) for each station pair were calculated. The symmetric correlation function was obtained by averaging the positive (causal signal) and

negative (acausal signal) lags, approximating a more homogeneous distribution of subsurface noise sources [Draganov, et al 2009]. The 6-hr correlation functions were then stacked for each station and station pair to form the reference correlation function trace used to determine velocity change.

5.2. Measuring temporal velocity changes at Tungurahua Volcano

Passive image interferometry (PII) was used to image temporal variations and the spatial extent of velocity structures in the shallow subsurface due to fracturing, fluid movement, or changes in source location. PII measured small velocity changes using correlations of coda from repeating earthquake sources (multiplets) or, more recently, noise correlations. Several PII methods have been previously used to calculate the relative velocity change in a variety of geologic settings. One of the earliest method, the moving window cross spectrum technique (MWCS) [Poupinet *et al.* 1984] was first developed to measure the relative velocity change, dV/V , between two earthquakes with similar locations and waveforms, but occurring at different times, called doublets. This method has been used to measure small velocity changes occurring prior to volcanic eruptions at Mt. Merapi [e.g. Ratdomopurbo and Poupinet, 1995; Wegler *et al.*, 2006], as well as before and after large, $>M5.9$, earthquakes [e.g. Poupinet 1984; Nishimura *et al.*, 2000].

The moving window cross spectrum technique (MWCS) measures the relative velocity change from the phase of the cross spectrum between the two earthquakes for a given time window, i . In the frequency domain the cross spectrum of the two seismograms given the Fourier transformed signals at the frequency, f , is given as $S_i(f) = A_{2i}^*(f) A_{1i}(f)$ where the asterisk, $*$, denoted the complex conjugate and $A_{1i}(f)$ and $A_{2i}(f)$ were the spectra of the two

earthquakes. The phase in radians, $\phi(f) = 2\pi\delta_i f$, was determined directly from the complex valued cross spectrum function, $S_i(f)$. The time delay, δt , was calculated from slope of the least squares line fit to the phase weighted by a factor, $\frac{C_i^2}{(1-C_i^2)}$, where the coherence, $C_i(f)$, between the two earthquakes is, $C_i(f) = \frac{S_i^2(f)}{A_{1i}(f)A_{2i}(f)}$, and the velocity change was given by the slope of the time delay versus time, $t(i)$, function, $\frac{d\delta}{dt} = \frac{-dV}{V}$, assuming the velocity change was homogenous throughout the medium. [Poupinet 1984]

To avoid errors from inaccurate earthquake locations or the expense of using repeated active sources earthquake coda correlations can be used instead of multiplet sources. The coda is the “tail” following the direct arrivals and is composed of multiply scattered [Sneider, 2004]. The coda is useful because coda correlations, like noise correlations, can be used to recover the Green’s function without having to determine the precise location of the source [Sneider 2004]. Furthermore, scattering paths, which are longer than the direct paths, result in the accumulation of very small travel time delays averaged over a longer path length. This allows one to measure very small velocity changes using scattered waveforms that cannot be measured using direct arrivals [Sneider 2006; Brenguier *et al.*, 2011]. Coda correlations have been used to both image the structure of the volcano Erebus [Chaput *et al.*, 2012] and measure relative velocity changes at Vanuatu after a large $M_w 7.3$ earthquake [Battaglia *et al.*, 2012].

The disadvantage of using earthquakes or discrete active sources is that they do not provide continuous information about changes in the medium. Continuous monitoring requires a continuous source that is now available with recent developments in retrieving the Green’s function from ambient noise [Lobkis and Weaver, 2001; Shapiro and Campillo, 2004; Sneider,

2004; Weaver and Lobkis, 2004; Roux, *et al.*, 2005; Wapenaar, 2004]. Ambient noise correlation have been used extensively in determining the structure of the crust and uppermost mantle on regional scales including studies in Europe, New Zealand, and South Africa in addition to the US [e.g. Lin *et al.* 2007, 2008; Mochetti *et al.* 2007; Bensen *et al.* 2008; Yang *et al.* 2007, etc.]. [Shapiro *et al.*, 2005; Sabra *et al.* 2005; Lin *et al.* 2007, 2008; Mochetti *et al.* 2007; Bensen *et al.* 2008; Yang *et al.* 2007]. Additionally, the velocity structure of Piton de la Fournaise has been imaged using surface wave dispersion measurements from ambient noise correlations by Brenguier *et al.* [2007].

More recently, the MWCS technique, applied to ambient noise correlations, has been used to monitor temporal velocity changes at active faults and volcanoes [Brenguier *et al.*, 2008a,b; Duputel *et al.*, 2008; Clarke *et al.*, 2011]. The MWCS method is very accurate for small measurements and by applying the technique to small time windows around individual arrivals in the Green's function, one can estimate the location and depth of the velocity changes. Unfortunately, this technique was very sensitive to random fluctuations (noise) in the estimated Green's function [Hadziioannou *et al.*, 2009], which may lead to erroneous velocity change measurements between the spurious arrivals.

5.3. Dilation Correlation Coefficient Method (DCC)

The dilation correlation coefficient method (DCC) is a better method for retrieving relative velocity changes from waveforms with low signal-to-noise ratios, such as ambient noise correlations in which the Green's function is only partially retrieved [Hadziioannou *et al.*, 2009]. The stability of DCC velocity change measurements using fluctuating (noisy) waveforms allows for the accurate calculation of small velocity changes using a finer temporal resolution. Correlation functions using shorter lengths of time (1 day versus 30 days) can be

used to determine very small relative velocity changes. This property is important the calculation of continuous dV/V and to monitoring volcanic eruption conditions.

The dilation correlation coefficient method (DCC) [Lobkis and Weaver, 2003; Sens-Schönfelder and Wegler, 2006; Hadziioannou *et al.*, 2009, 2011; Weaver *et al.* 2011] was based on the idea that waveforms will suffer from a dilation and distortion due to different rates of mode conversion between P (dilatational) and S (shear) waves in a diffuse field. The differing rates result from changes in elastic properties of a medium due to stress, to a lesser extent temperature, and the degree of heterogeneity of a medium [Weaver and Lobkis, 2000; Lobkis and Weaver, 2003]. DCC was first used to measure velocity changes at Mt. Merapi volcano attributed to seasonal variations in ground water level [Sens-Schönfelder and Wegler, 2006]. Subsequently, it was used in measuring velocity changes in the Los Angeles Basin [Meier *et al.*, 2010], and before and after 2004 Parkfield earthquake along the San Andreas Fault [Hadziioannou *et al.* 2011; Weaver *et al.*, 2011] and the 2004 $M_w 6.6$ Mid-Niigata earthquake in Japan [Wegler and Sens-Schönfelder 2007].

The homogenous relative velocity change, dV/V , was found by searching for the dilation (stretching) factor, ϵ , that maximized the cross-correlation coefficient between two waveforms, ϕ_1, ϕ_2

$$X(\epsilon) = \frac{\int \phi_1(t) \phi_2(t(1+\epsilon)) dt}{\sqrt{\int \phi_1^2(t) dt \int \phi_2^2(t(1+\epsilon)) dt}} \quad (1)$$

Identical waveforms have a maximum correlation coefficient, $X_{max}(\epsilon)$ of 1 [Weaver *et al.*, 2011]. Any value of $X_{max}(\epsilon)$ less than unity indicates that the two waveforms differ by more than a simple dilation and is a measure of the distortion between the two waveforms, ϕ_1, ϕ_2 .

This allows for quantification of whether noise source locations are stable or changes over time; $X_{max}(\epsilon) \sim 1$ indicates stable sources and $X_{max}(\epsilon) \ll 1$ indicates that noise source locations are changing [Hadziioannou *et al.*, 2011]. The dilation (or stretching) factor ϵ is related to the relative time shift by,

$$\epsilon = -\frac{d\delta}{dt} = \frac{dV}{V} \quad (2)$$

To distinguish between velocity changes that are due to changes in the wave speed of a medium from changes due to erroneous fluctuations in the waveform or changes in noise source, Weaver *et al.* [2011] derived an expression for the root mean square erroneous relative dilation,

$$\text{RMS } \epsilon = \frac{\sqrt{1-X^2}}{2X} \sqrt{\frac{6\sqrt{\frac{\pi}{2}}T}{\omega_c^2(t_2^3-t_1^3)}} \quad (3)$$

X is the correlation coefficient, T is the inverse of the frequency bandwidth, t_1 and t_2 are the start and end times of the window used in calculating X , and ω_c is the center frequency of the bandwidth. Changes in dV/V greater than this RMS ϵ value are interpreted as real dilations, and not measurement errors [Weaver *et al.*, 2011].

5.4. Procedures for measuring dV/V at Tungurahua

The dilation correlation coefficient method [Weaver and Lobkis, 2000; Hadziioannou *et al.*, 2009; Weaver *et al.*, 2011] was used to calculate the relative velocity change between the reference correlation functions and individual 6-hr, and 1,5,7,10-day correlation functions. Each individual correlation function was interpolated at times $t(1+\epsilon)$, where ϵ , the stretching factor, was the relative velocity change, dV/V of the individual correlation function. The

dilation correlation coefficient $X(\epsilon)$ was calculated for each value of ϵ from -0.02 to 0.02 in increments of 0.00002. Poor quality velocity measurements corresponding values of $X_{max}(\epsilon) \leq 0.5$ were discarded. The dV/V measurements for each station and station pair were averaged and the standard deviation of the dV/V measurements was calculated. For $X_{max}(\epsilon) \geq 0.5$ the estimate of the root mean square estimate of the relative dilation between the reference correlation function and the individual correlation functions, RMS ϵ , was calculated as 0.002 for the band from 0.5 to 4 Hz; erroneous relative dilation changes in dV/V greater than this RMS ϵ value were interpreted as real dilations, not measurement errors. Velocity changes were also measured for correlation functions filtered between 0.5 to 2 Hz and 2 to 4 Hz, which corresponds to RMS ϵ values of 0.006 and 0.002, respectively

Chapter 6

RESULTS

6. Results: Correlation functions

For each 6-hour, vertical component record of ambient noise the symmetric correlation function (CF) from 0 to 15 seconds lag time was calculated for each station (Figure 10-Figure 14, lower left panel) and station pair (Figure 15-Figure 24, lower left panel). The reference CF at each station and station pair was calculated by stacking each individual CF for 2010 (Figure 10-Figure 14, lower right panel). The correlation coefficient between the reference trace and the individual CFs was calculated as an estimate of the baseline variance between the individual CFs and the reference (Figure 10-Figure 24, top panel, right hand axis, solid line). This variance corresponds to the level of fluctuations of the individual CF around the reference trace and was a measure of the emergence of coherent arrivals in the CF [Sabra *et al.*, 2005]. A correlation coefficient of ~ 1 means the individual and reference waveforms were coherent with stable noise sources, while a value $\ll 1$ was less coherent and noise source locations vary over time [Hadziioannou, *et al.* 2011].

Figure 10-Figure 14 shows the individual autocorrelation functions (ACF) for each station from January1-December31, 2010 (lower left panel), the 1-yr stacked reference trace (lower right panel), and the correlation coefficient between each individual CF and the reference CF (upper panel, right axis, solid line); the real-time-seismic amplitude measurement (RSAM) (upper panel, left axis, dashed line), peaks in the curve indicate seismically active

periods at Tungurahua volcano. The gray dashed lines indicate the episodes of increased eruptive activity. The ACFs showed a high correlation coefficient, ~ 0.8 , during quiescent, non-eruptive periods. At the stations BRUN and BBIL, both located at roughly the same elevation, on the smooth north and west flanks of the volcano, there were dramatic drops in the correlation coefficient during the periods of increased eruptive activity, from ~ 0.95 to ~ 0.6 . The three other stations (BULB, BPAT, and BMAS), did not exhibit the drops in correlation coefficient and remained stable during the eruptive periods. These stations were located on the topographically rougher and older flanks of Tungurahua.

Figure 15-Figure 24 show the individual cross-correlation functions (XCF) for each station pair from January 1-December 31, 2010 (lower left panel), the 1-yr stacked reference trace (lower right panel), and the correlation coefficient (upper panel, right axis, solid line) and average RSAM for each station pair (upper panel, left axis, dashed line). The gray dashed lines indicate the periods of increased eruptive activity. The XCFs exhibited lower overall correlation coefficients than the ACFs and spatial and temporal variations in their values. BULB-BRUN, BBIL-BULB, BMAS-BPAT, BBIL-BMAS, and BBIL-BPAT had the highest overall correlation coefficient around ~ 0.6 to ~ 0.7 , which decreased to between ~ 0.2 - 0.4 during the active eruptive episodes.

During periods of increased eruptive activity, the CF waveforms appear to show a time shift and/or slight distortion. Quiescent period coherent arrivals were lower amplitude and arrived at a constant time throughout the period, and may have contained high frequency fluctuations. Active episode coherent arrivals were stronger amplitude, broad arrivals and may have appeared shifted relative to arrivals during quiescent periods and relative to earlier CFs within the active episode. For example, during the spike in the RSAM curve of the first active

episode the arrivals were delayed by about ~ 0.1 - 0.2 s. During the second active episode in May, there was also a noticeable delay of ~ 0.1 - 0.2 s coinciding with the spike in the RSAM curve and following this period the arrivals were variable and much less organized. The arrivals of the third active episode showed a similar shift during the peak period of the RSAM curve.

6.1. Autocorrelation Functions—Individual Stations Clockwise from North

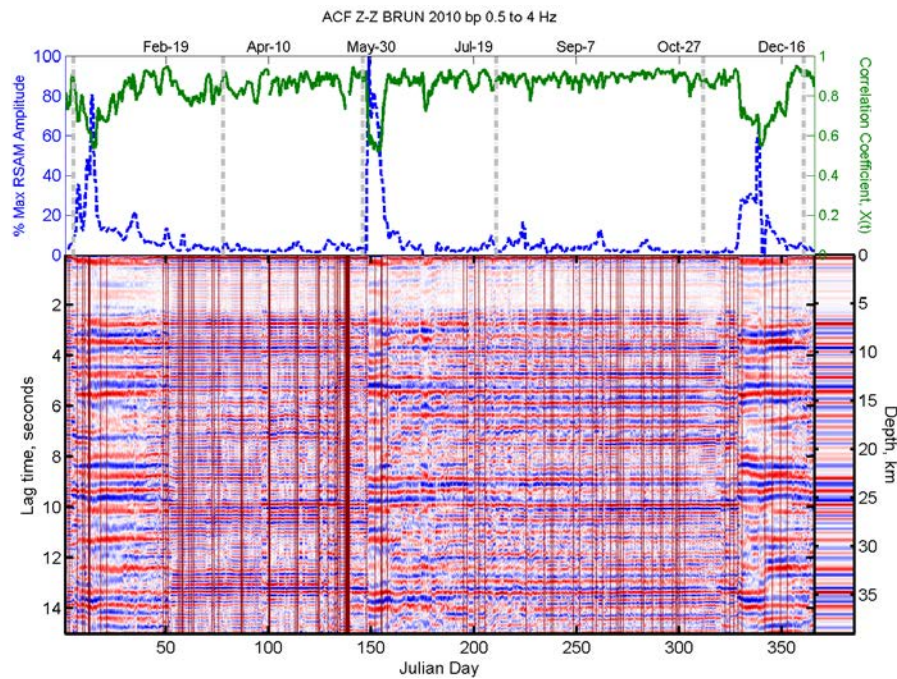


Figure 10. Individual and 1 year stacked autocorrelation functions at station BRUN for 2010. Colors are amplitude normalized to the mean trace amplitude; red is positive and blue is negative amplitude. The rms amplitude AGC is applied to the traces in a 4s window. Vertical, solid, dark red lines indicate that no CF is calculated for that time period due to a gap in the seismic record. The lower left hand window shows the individual ACF traces calculated from 6hrs records of ambient noise, the lower right window, outlined in black, is the 1-yr stacked ACF that is used as the reference trace in calculating dV/V , with depth calculated assuming a constant $V_p=2.5$ km/s and the top window shows the RSAM calculated for each 6hr record at BRUN (blue, dashed line and axis) and the correlation coefficient (green, solid line and axis) calculated between the unstretched reference trace (lower right) and each individual CF trace (lower left). Dashed light gray bars indicate the start and end of the three periods of increased volcanic activity.

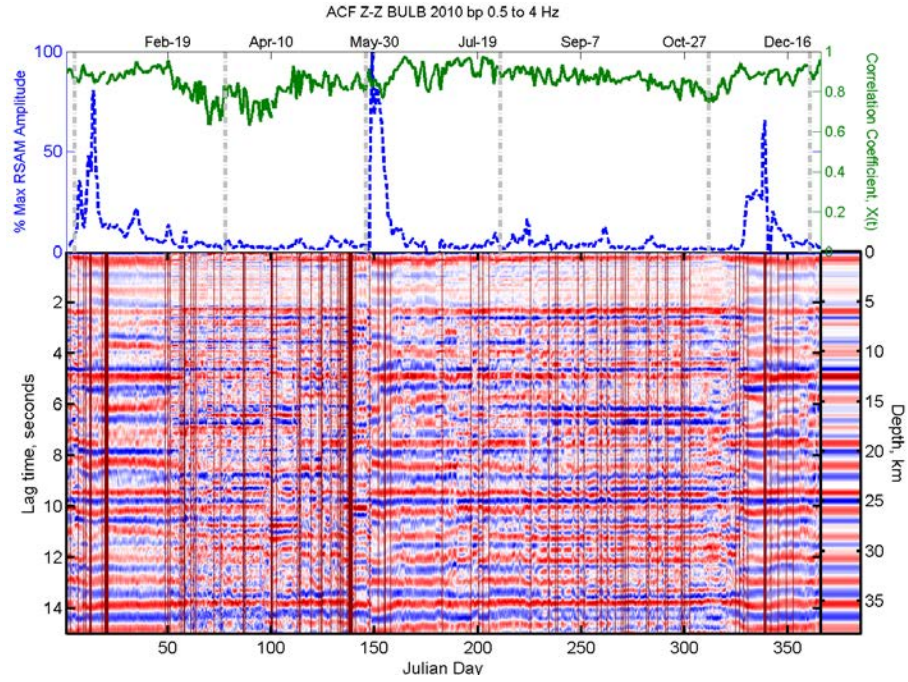


Figure 11. Individual and 1 year stacked autocorrelation functions at station BULB for 2010. Annotation is the same as for Figure 10.

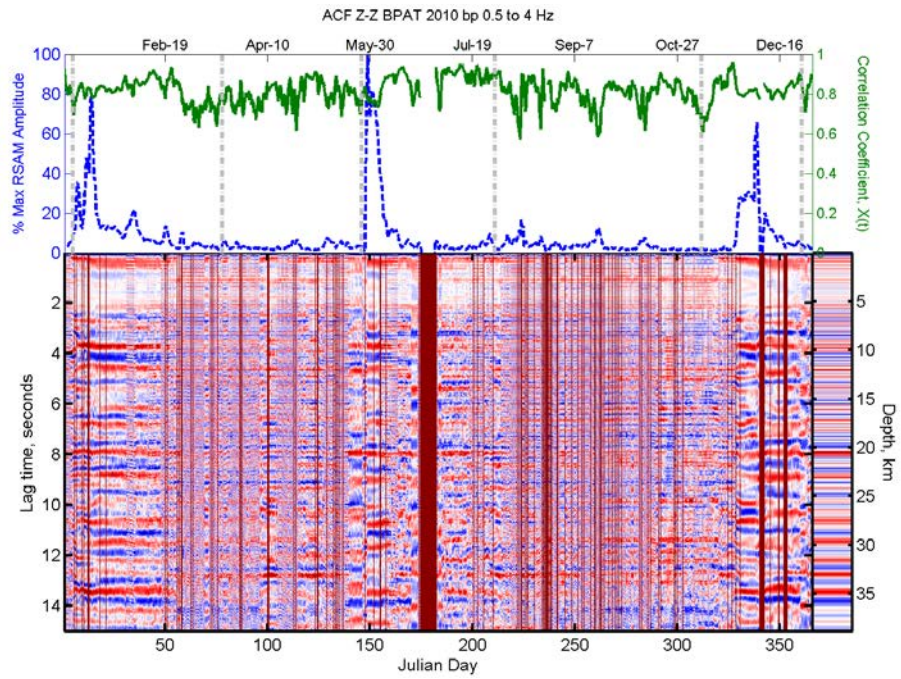


Figure 12. Individual and 1 year stacked autocorrelation functions at station BPAT for 2010. Annotation is the same as for Figure 10.

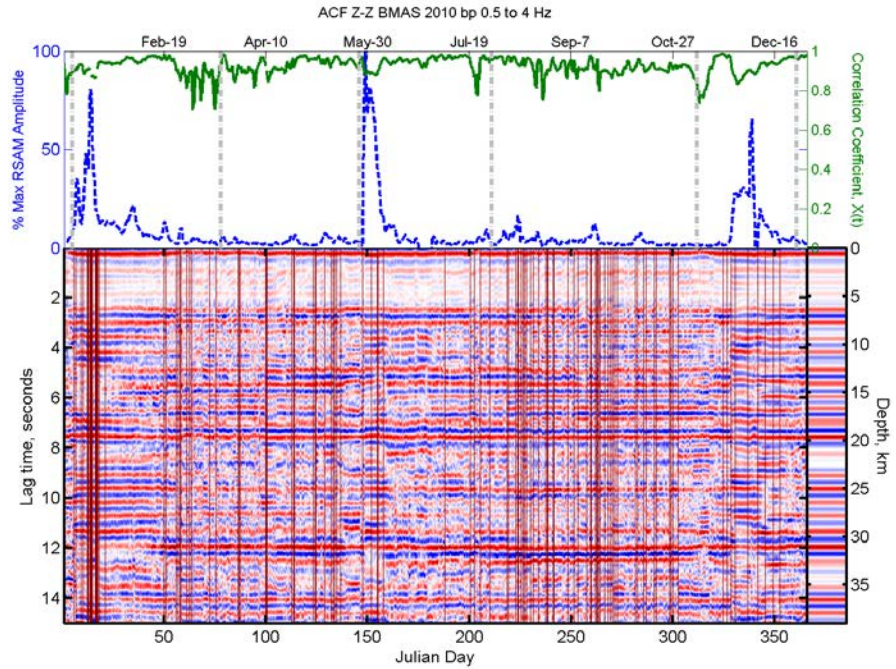


Figure 13. Individual and 1 year stacked autocorrelation functions at station BMAS for 2010. Annotation is the same as for Figure 10.

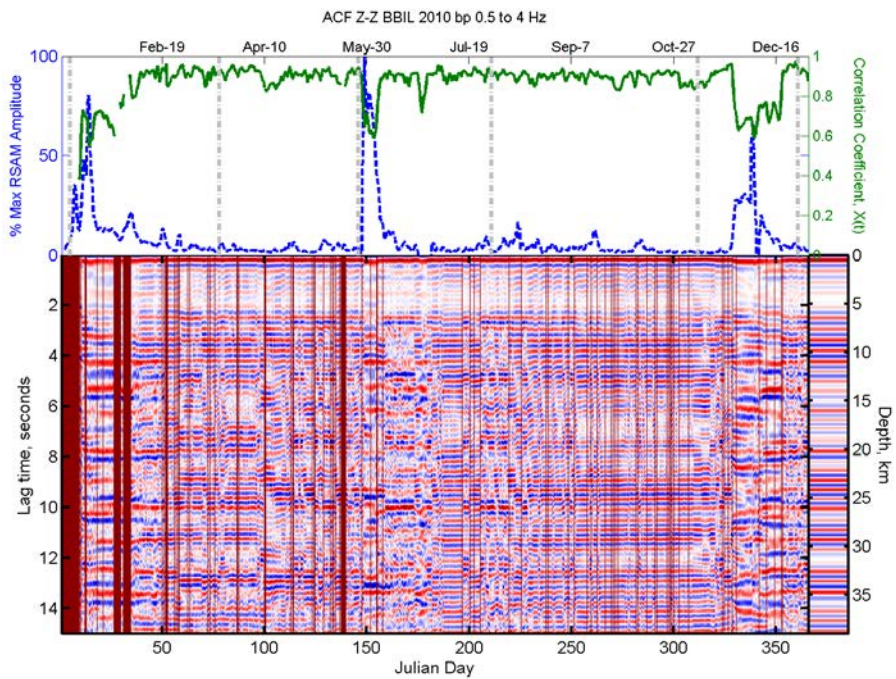


Figure 14. Individual and 1 year stacked autocorrelation functions at station BBIL for 2010. Annotation is the same as for Figure 10.

6.2. Cross-Correlation Functions—Near Vent Crossing Station Pairs

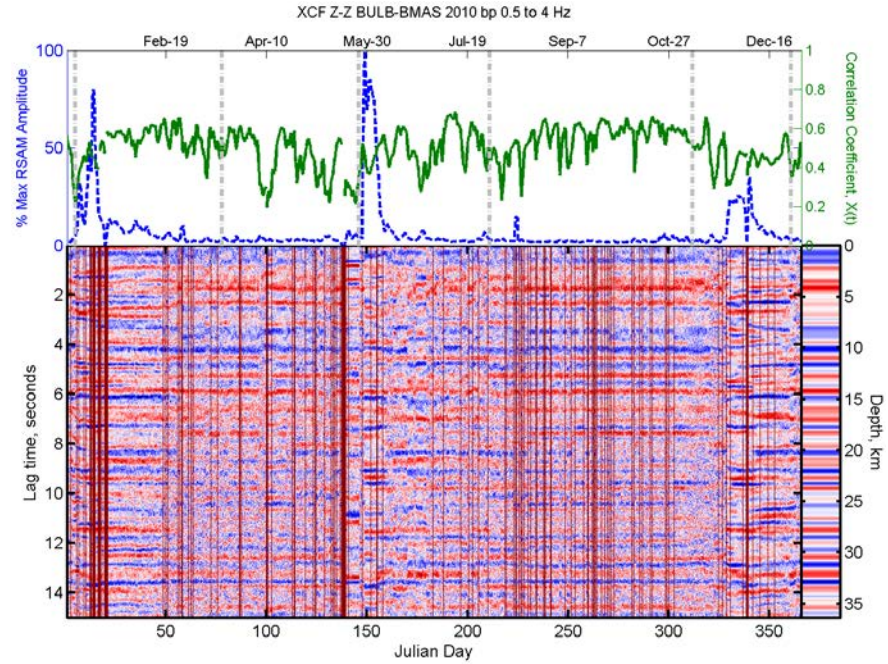


Figure 15. Individual and 1 year stacked cross-correlation functions at station pair BULB-BMAS, crossing nearest to the vent, for 2010. Annotation is the same as for Figure 10.

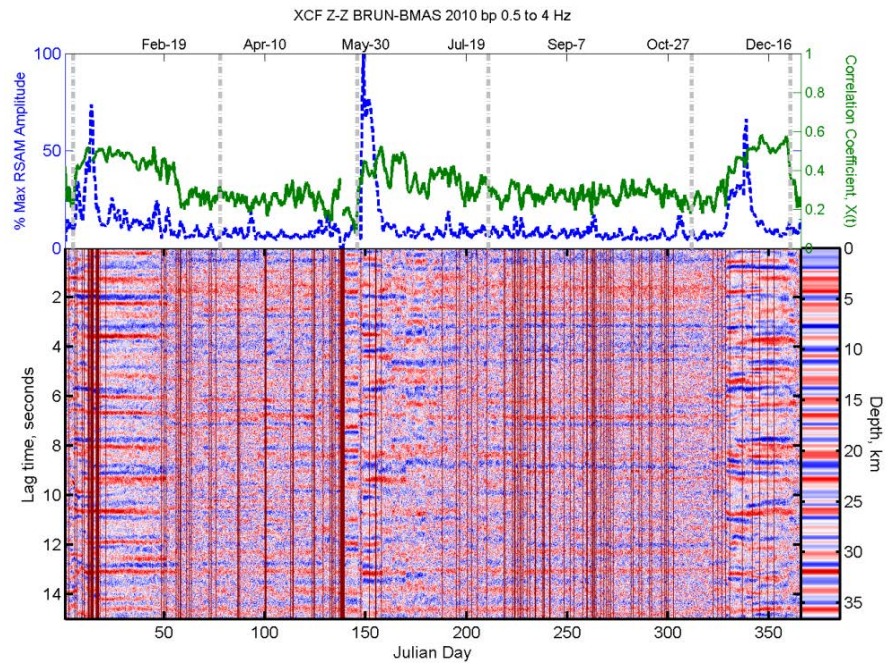


Figure 16. Individual and 1 year stacked cross-correlation functions at station pair BRUN-BMAS, crossing near to the vent, for 2010. Annotation is the same as for Figure 10.

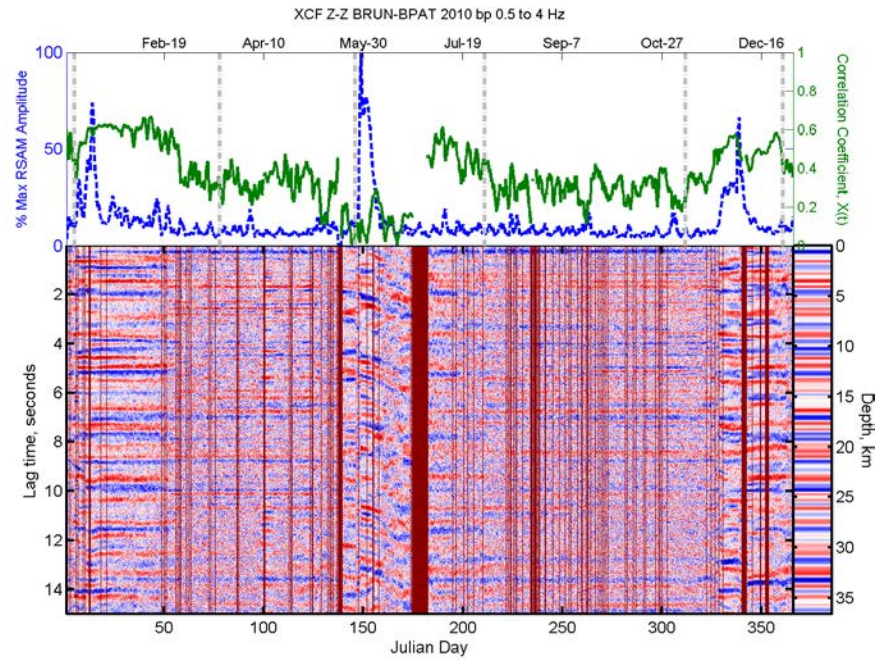


Figure 17. Individual and 1 year stacked cross-correlation functions at station pair BRUN-BPAT, crossing near to the vent, for 2010. Annotation is the same as for Figure 10.

6.3. Cross-Correlation Functions—North Flank (W-E) Crossing Station Pairs

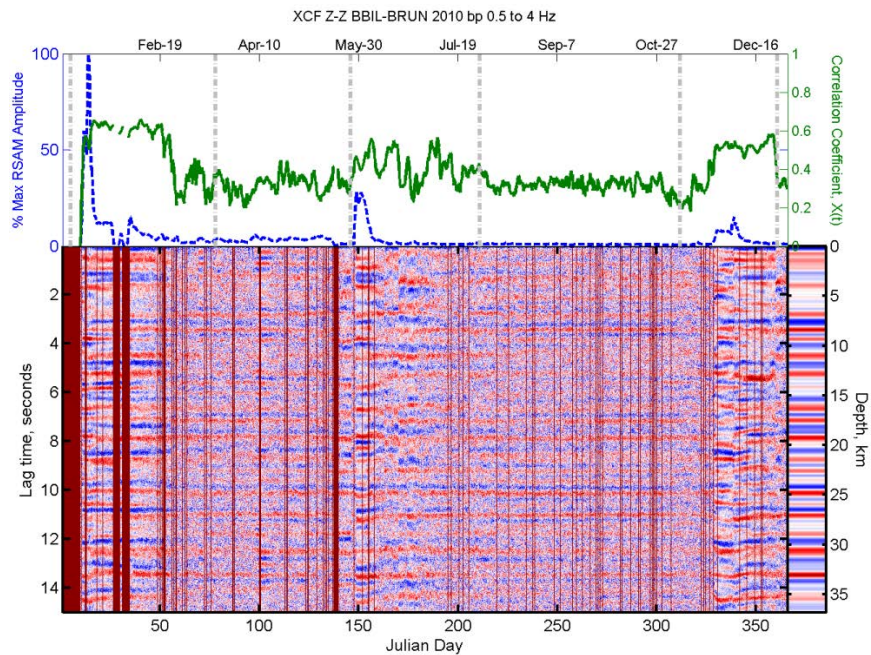


Figure 18. North flank crossing individual and 1 year stacked cross-correlation functions at station pair BBIL-BRUN for 2010. Annotation is the same as for Figure 10.

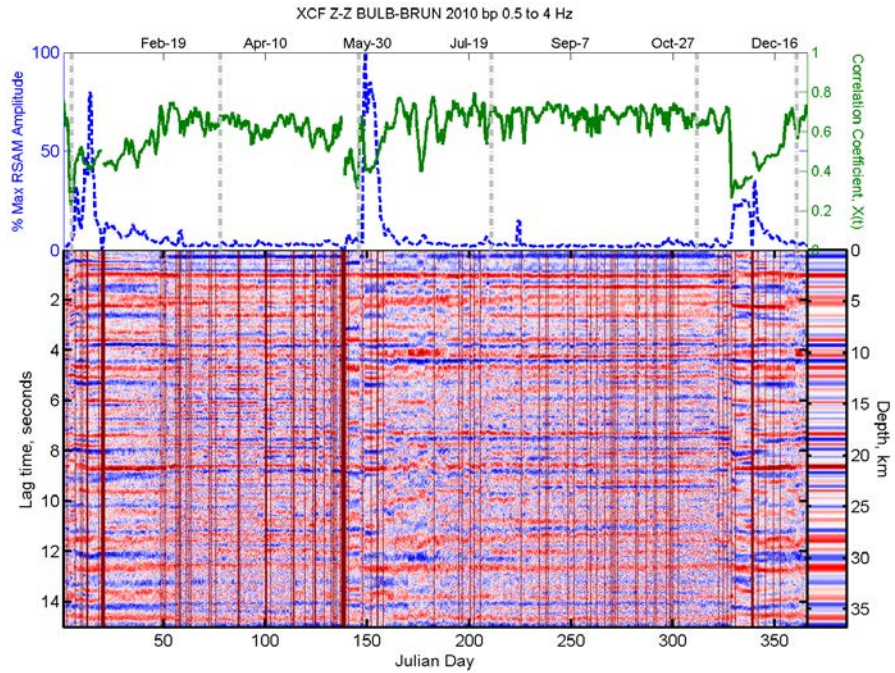


Figure 19. North flank crossing individual and 1 year stacked cross-correlation functions at station pair BULB-BRUN for 2010. Annotation is the same as for Figure 10.



Figure 20. North flank crossing individual and 1 year stacked cross-correlation functions at station pair BBIL-BULB for 2010. Annotation is the same as for Figure 10.

6.4. Cross-Correlation Functions—South Flank (W-E) Crossing Station Pairs

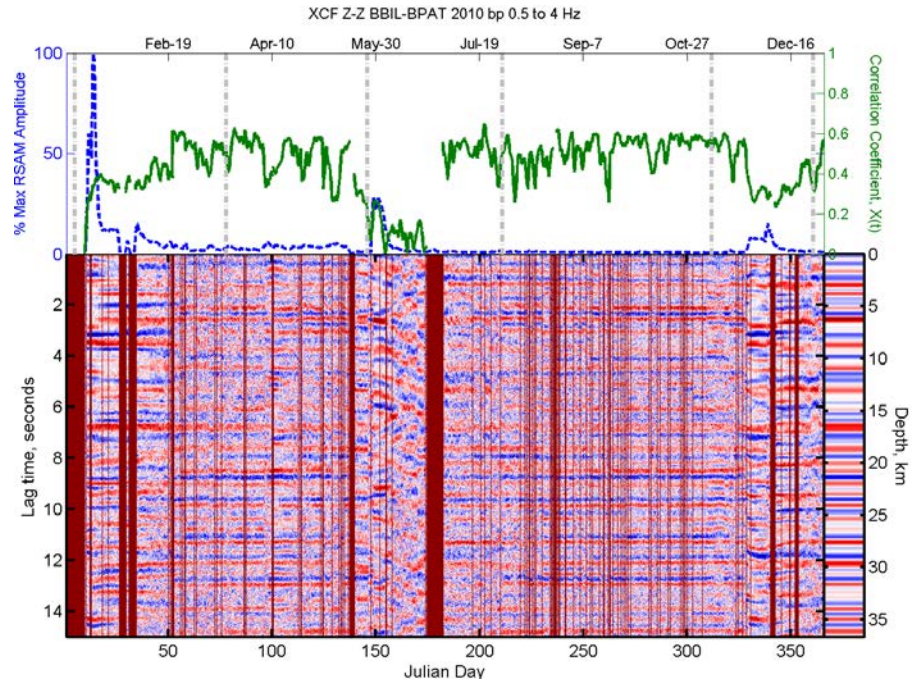


Figure 21. South flank crossing individual and 1 year stacked cross-correlation functions at station pair BBIL-BPAT for 2010. Annotation is the same as for Figure 10.

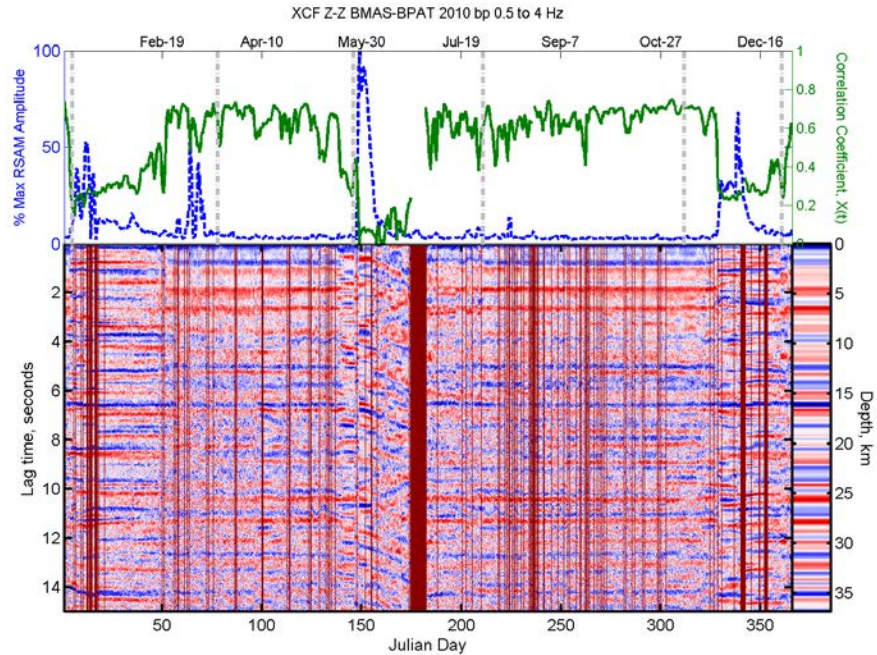


Figure 22. South flank crossing individual and 1 year stacked cross-correlation functions at station pair BMAS-BPAT for 2010. Annotation is the same as for Figure 10.

6.5. Cross-Correlation Functions—East and West Flank (N-S) Crossing Station Pairs

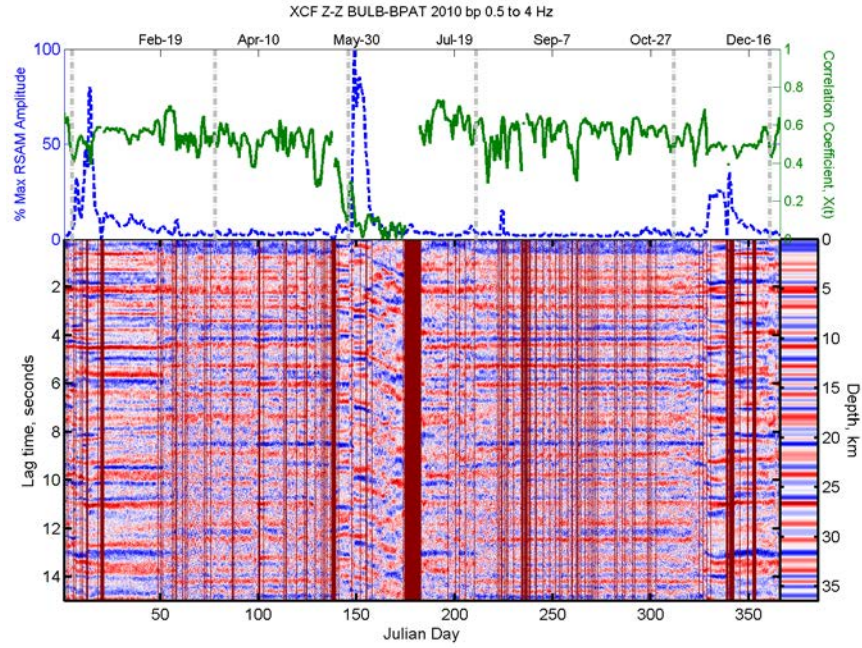


Figure 23. East flank crossing individual and 1 year stacked cross-correlation functions at station pair BULB-BPAT for 2010. Annotation is the same as for Figure 10

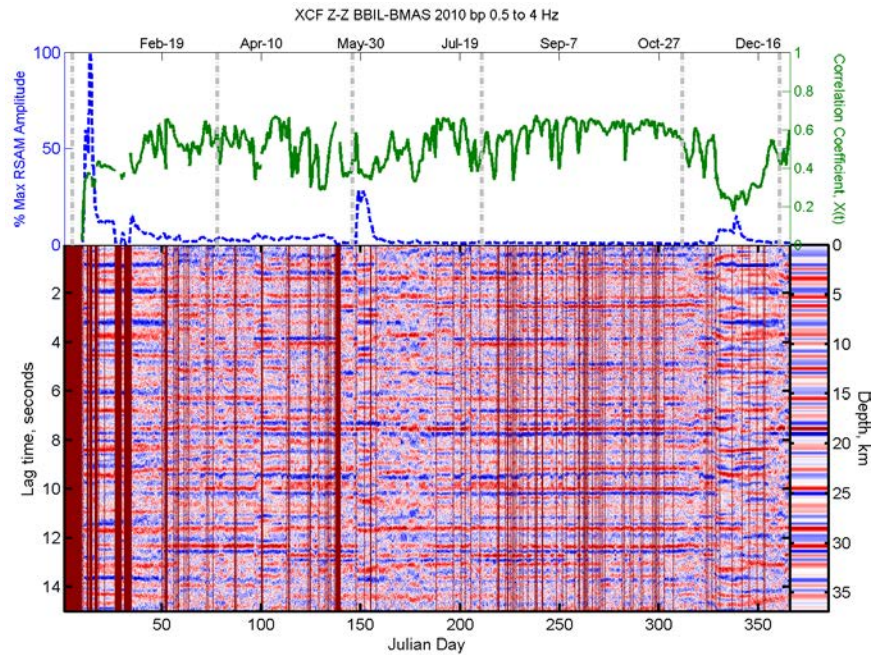


Figure 24. West flank crossing individual and 1 year stacked cross-correlation functions at station pair BBIL-BMAS for 2010. Annotation is the same as for Figure 10.

6.6. Results Figures: Velocity change, dV/V , and maximum correlation coefficient, X_{\max} , for 6hrs and 1, 5, 7 and 10 day stacks

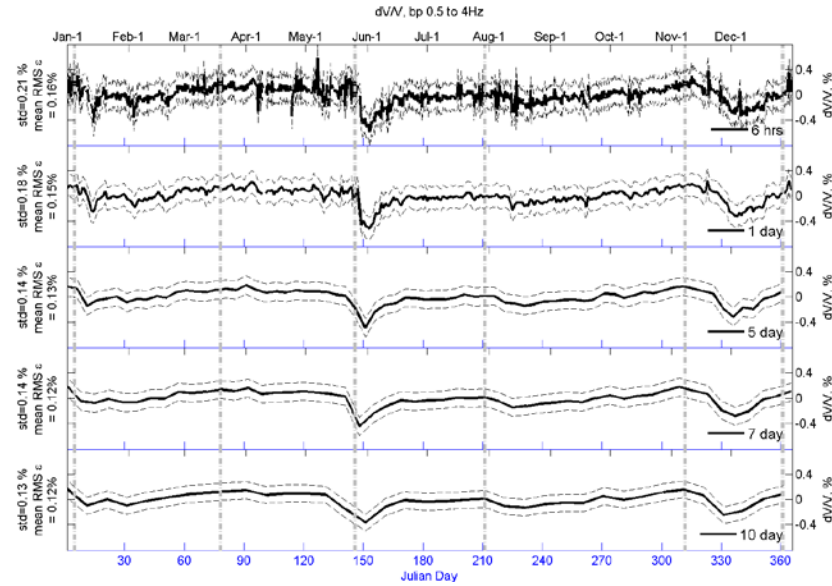


Figure 25.(top to bottom panel), % dV/V for 6hrs and 1, 5, 7 and 10 days (thick black line) and band-passed filtered from 0.5 to 4Hz (wide-band) averaged over all stations and station pairs with 1σ standard deviation bars (thin dashed line). Also plotted are dashed gray bars indicating the three episodes of increased volcanic activity

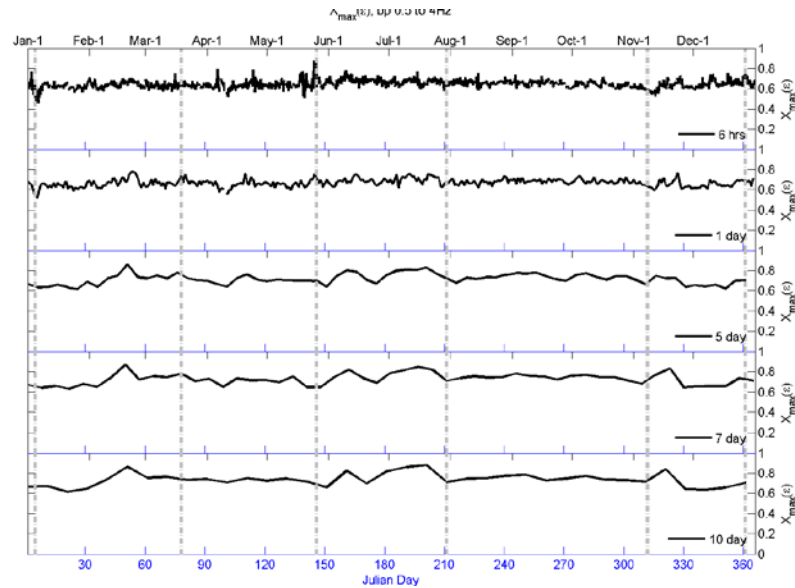


Figure 26.(top to bottom panel), Average X_{\max} , corresponding to the dV/V curves for 6hrs, and 1, 5, 7 and 10 days (thick black line) and band-passed filtered from 0.5 to 4 Hz (wide-band) averaged over all stations and station. Annotation is the same as for Figure 25

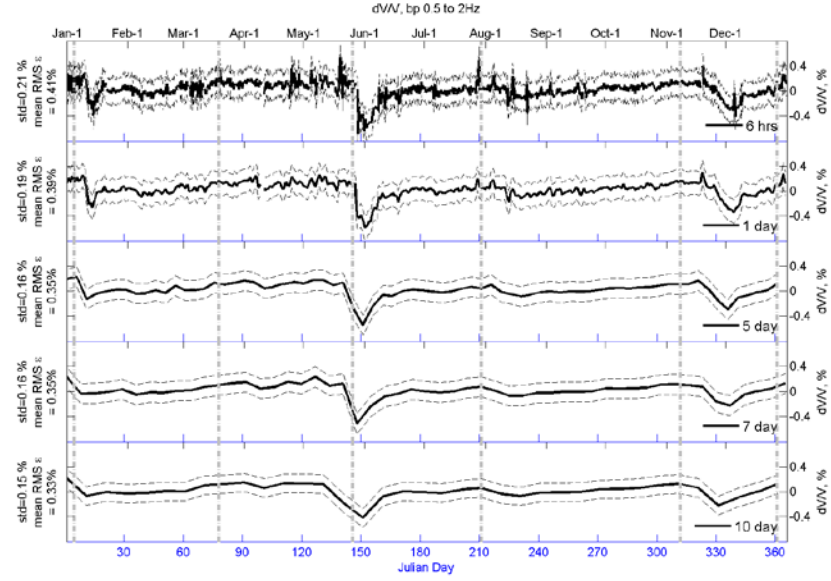


Figure 27.(top to bottom panel), % dV/V for 6hrs and 1, 5, 7 and 10 days (thick black line) and band-passed filtered from 0.5 to 2 Hz (low frequency) averaged over all stations and station pairs with 1σ standard deviation bars (thin dashed line). Also plotted are dashed gray bars indicating the three episodes of increased volcanic activity.

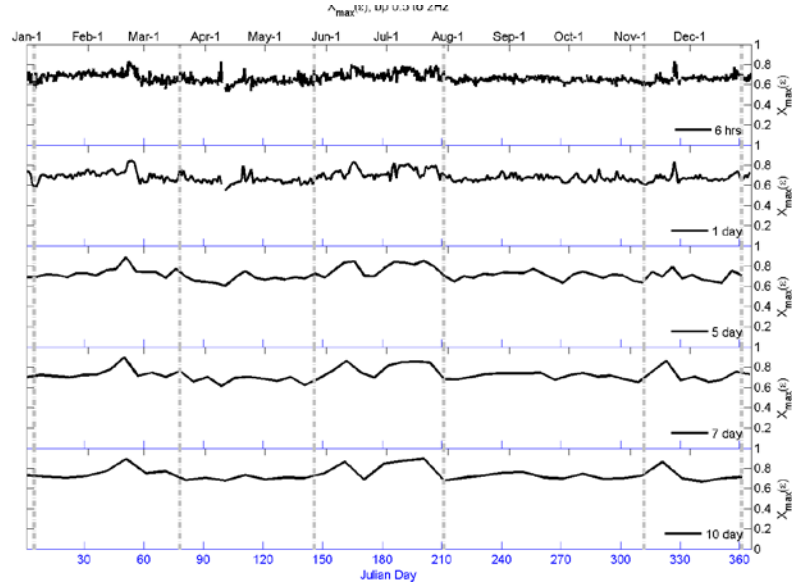


Figure 28.(top to bottom panel), Average X_{max} , corresponding to the dV/V curves for 6hrs, and 1, 5, 7 and 10 days (thick black line) and band-passed filtered from 0.5 to 2Hz (low-frequency) averaged over all stations and station. Annotation is the same as for Figure 27

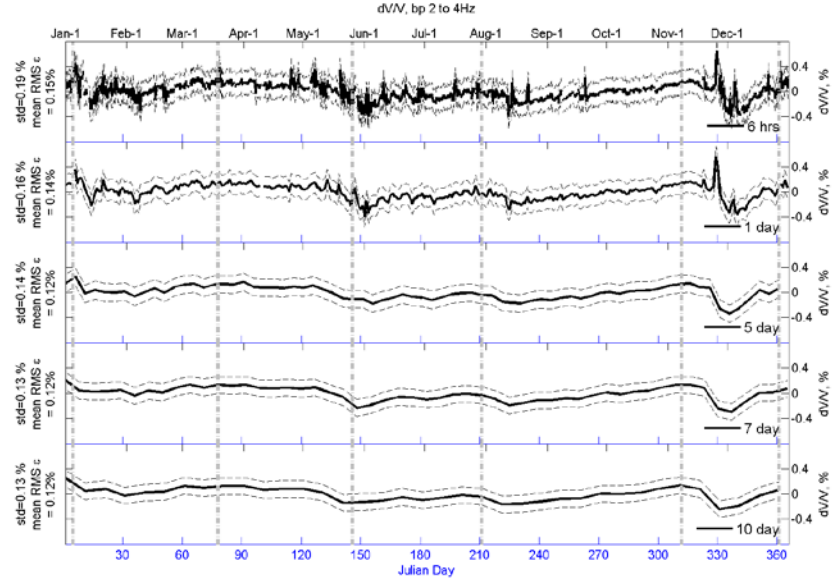


Figure 29.(top to bottom panel), $\% dV/V$ for 6hrs and 1, 5, 7 and 10 days (thick black line) and band-passed filtered from 2 to 4 Hz (high frequency) averaged over all stations and station pairs with 1σ standard deviation bars (thin dashed line). Also plotted are dashed gray bars indicating the three episodes of increased volcanic activity

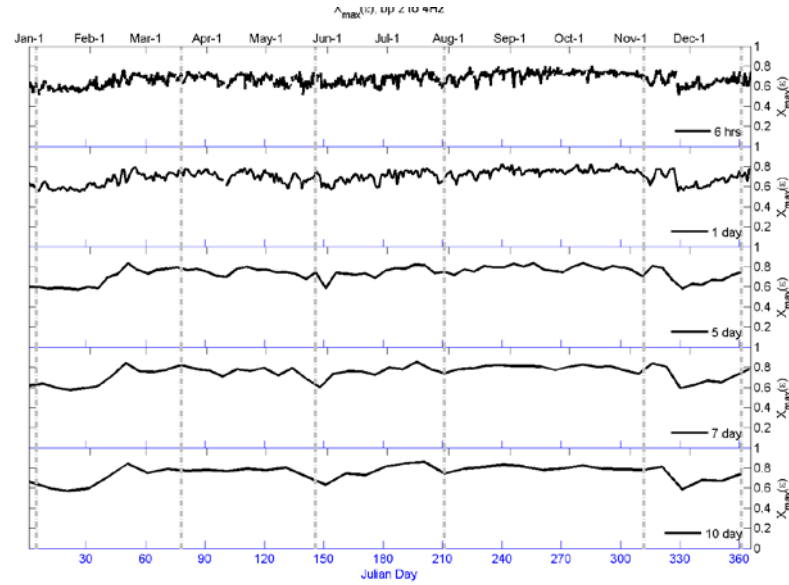


Figure 30.(top to bottom panel), Average X_{max} , corresponding to the dV/V curves for 6hrs, and 1, 5, 7 and 10 days (thick black line) and band-passed filtered from 0.5 to 2Hz (low-frequency) averaged over all stations and station. Annotation is the same as for Figure 29 Results: Velocity changes, dV/V

6.7. Results: Relative velocity change, dV/V

Using the dilation correlation coefficient method, the relative velocity change, dV/V , was calculated between the 1-year stacked reference trace and the individual 6-hrs and 1, 5, 7 and 10 day stacked CFs, filtered between 0.5 and 4 Hz (wide-band). Velocity changes were also measured for CFs filtered between 0.5 to 2 Hz (low frequency) and 2 to 4 Hz (high frequency). Assuming a spatially constant velocity change, measurements were averaged over all 15 CFs (5 autocorrelations and 10 cross-correlations) to determine the average relative velocity change, dV/V , at Tungurahua. Figure 25 to Figure 32 show this spatially averaged dV/V (thick black line), with 1σ standard deviation bars (thick black line), and corresponding maximum correlation coefficient, X_{\max} , curves for the 6-hrs and 1, 5, 7 and 10 day stacks, filtered from 0.5-4Hz (Figure 25, Figure 26), 0.5-2Hz (Figure 27, Figure 28) and 2-4Hz (Figure 29, Figure 30). Table 1 summarizes the year-long average dV/V , standard deviation, correlation coefficient and minimum acceptable level of fluctuation for the different bands. For 0.5-4 Hz wide-band runs (Figure 25, Figure 26; Figure 31, top panel), the average dV/V ranges between -0.0059% to -0.0073% , for the 5 day and 6 hour stacks, respectively and 1σ standard deviation bars of $\pm 0.13\%$ to $\pm 0.21\%$. The mean minimum acceptable level of fluctuation, $RMS \epsilon$, decreased with increasing stack length from 0.16% (6 hour stack) to 0.12% (10 day stack), for an average correlation coefficient X_{\max} of 0.64 to 0.74 , respectively. For the low frequency, 0.5-2 Hz band (Figure 27, Figure 28; Figure 31, middle panel), the average dV/V was higher, ranging between 0.0101% to 0.0210% , for the 10 and 1 day stacks, respectively. The 1σ standard deviation error bars range from $\pm 0.15\%$ to $\pm 0.21\%$. The mean minimum acceptable level of fluctuation, $RMS \epsilon$, was higher than for the wide-band and ranges from 0.41% (6 hour stack) to 0.31% (10 day stack), for average correlation coefficients, X_{\max} , of 0.66 and 0.74 , respectively. In the high frequency band, 2-4 Hz (Figure 29, Figure 30; Figure 31, bottom

panel), the average dV/V was similar to that of the wide-band, ranging between -0.0028% to -0.0079% , for the 10 and 7 day stacks, respectively. The 1σ standard deviation error bars range from $\pm 0.13\%$ to $\pm 0.19\%$. The mean minimum acceptable level of fluctuation, RMS ϵ , ranges from 0.15% (6 hour stack) to 0.12% (10 day stack), for average correlation coefficients, X_{\max} , of 0.67 and 0.74 respectively. Overall, the maximum correlation coefficient was high and ranges from 0.64 to 0.75 , though there may be some non-stationary sources that add errant fluctuations to the recovered coherent arrivals. (see Table 1 for summary)

Table 1. Summary of mean dV/V , the 1σ standard deviation, X_{max} and corresponding RMS ϵ for each stack length of individual CFs used in the calculation (6-hrs and 1, 5, 7 and 10 day stacks) and each filter band (0.5-4 Hz, 0.5-2 Hz, 2-4 Hz) applied to the CFs.

	0.5-4 Hz, Wide band			
CF stack length	<i>mean dV/V, %</i>	<i>1 σ standard deviation, %</i>	X_{max}	<i>mean RMS ϵ</i>
6 hours	-0.0073	0.21	0.64	0.16
1 day	-0.0070	0.18	0.67	0.15
5 days	-0.0059	0.14	0.72	0.13
7 days	-0.0067	0.14	0.73	0.12
10 days	-0.0068	0.13	0.74	0.12
	0.5-2 Hz, Low Frequency			
CF stack length	<i>mean dV/V, %</i>	<i>1 σ standard deviation, %</i>	X_{max}	<i>mean RMS ϵ</i>
6 hours	0.0203	0.21	0.66	0.41
1 day	0.0210	0.19	0.68	0.39
5 days	0.0160	0.16	0.72	0.35
7 days	0.0136	0.16	0.72	0.35
10 days	0.0101	0.15	0.74	0.33
	2-4 Hz, High Frequency			
CF stack length	<i>mean dV/V, %</i>	<i>1 σ standard deviation, %</i>	X_{max}	<i>mean RMS ϵ</i>
6 hours	-0.0032	0.19	0.67	0.15
1 day	-0.0053	0.16	0.70	0.14
5 days	-0.0078	0.14	0.73	0.12
7 days	-0.0079	0.13	0.74	0.12
10 days	-0.0028	0.13	0.75	0.12

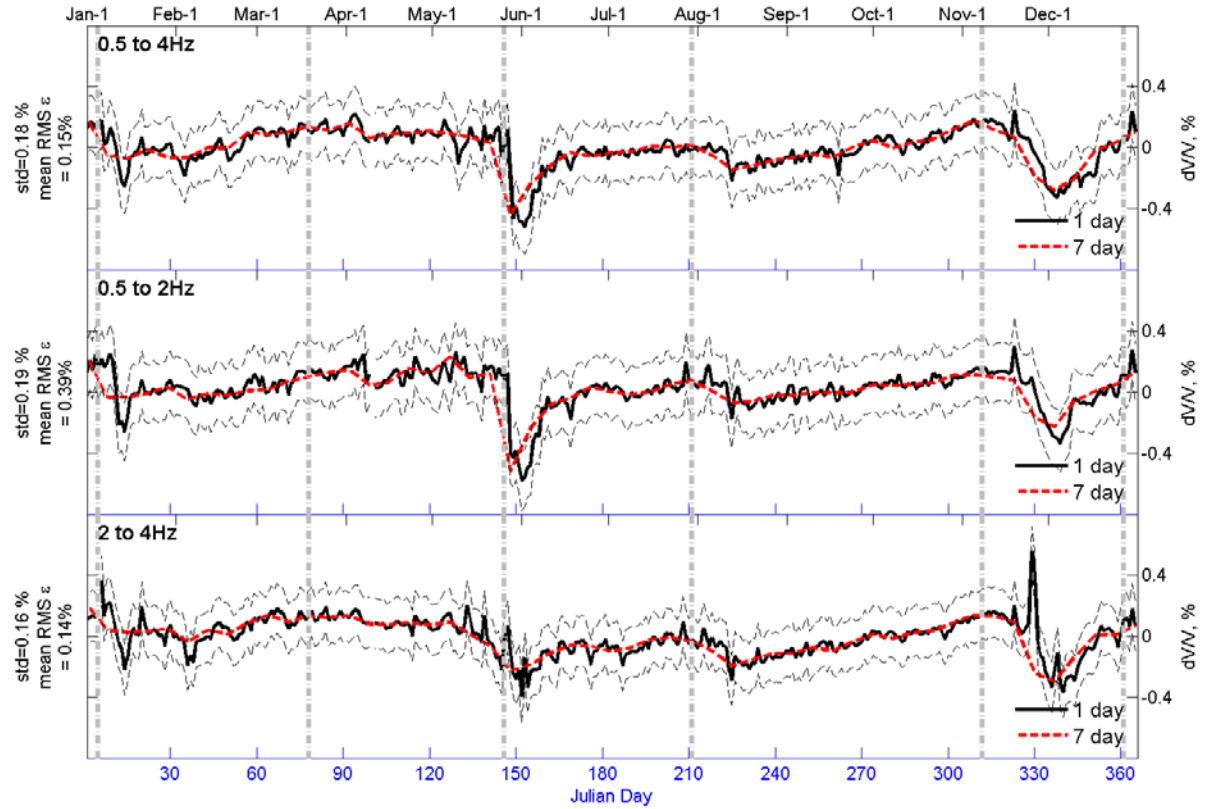


Figure 31. % dV/V for 1- (thick solid black line) and 7 day-stacks (dashed red line) averaged over all stations and station pairs with 1σ standard deviation bars (thin dashed line). Prior to calculation of dV/V the CFs were filtered in the bands (a) 0.5-4Hz (wide-band), (b) 0.5-2Hz (low frequency), and (c) 2-4Hz (high frequency) Also plotted are dashed gray bars indicating the three episodes of increased volcanic activity.

The dV/V curves for 2010 showed similar trends regardless of the length of the individual CF used in the calculation (6-hrs and 1, 5, 7 and 10 day stacks) or the filter band (0.5-4 Hz, 0.5-2 Hz, 2-4 Hz) applied to the CFs. During the three episodes of increased volcanic activity, dV/V decreased significantly after the onset of eruptive activity; the difference between dV/V at the start of the active episode and the minimum measured dV/V was 0.41% for episode 1 (January 14), 0.53% for episode 2 (June 2) and 0.49% for episode 3 (December 4), measured from the 1 day, 0.5-4Hz filtered dV/V curve (Figure 31, top panel, black line). These velocity changes were greater than the mean minimum fluctuation strength,

RMS $\epsilon = 0.15\%$ for the 0.5-4 Hz curve. The low frequency curve (0.5-2 Hz) shows similar drops of 0.40% (January 14), 0.67% (June 3), and 0.50% (December 6) from the onset of eruptive activity to the minimum measured dV/V , which were all greater than the mean minimum fluctuation strength, RMS $\epsilon = 0.39\%$ (Figure 31, middle panel, black line). Drops of 0.58% (January 14), 0.38% (June 3), and 0.52% (December 6) with a mean RMS $\epsilon = 0.14\%$ were measured on the high frequency (2-4 Hz) curves (Figure 31, bottom panel, black line). Interestingly, the second episode (May-July) showed less of a velocity drop for the high frequency band for than the other two bands, while the first and last episodes had comparable drops in relative velocity. The dominant source of the velocity change during the May episode may be located deeper than the peak sensitivity of the 2-4 Hz band, suggesting that the eruptive characteristics of the May episode were different from those of the January-March and November-December episodes. Measurements of relative velocity change, dV/V , can be affected by the presence or lack of sources, such as LP earthquake events. It may be significant that more LPs, which dominate the 0.5-2 Hz band (K. Kim, pers. comm., 2013), were recorded during the second episode than the first and last episodes. Another interesting feature of the 2-4 Hz band was the large positive spike in dV/V late on November 26 and a smaller spike on December 4. The correlation coefficient for that day was reasonable, 0.55 and 0.58, respectively, and those days corresponded to the reported occurrence of lava fountaining (fuentes de lava) and the La Hacienda andesite lava flow.

The quiescent periods between episodes of eruptive activity exhibited a gentle increase in dV/V . Between the end of the first and onset of the second eruptive episodes, March 20 to May 25, dV/V increased by +0.15 % measured on the 1 day, 0.5-4Hz filtered dV/V curve (Figure 31, top panel, black line); +0.14% measured on the 1 day, 0.5-2Hz filtered dV/V curve

(Figure 31, middle panel, black line); and +0.39% on the measured on the 1 day, 2-4Hz filtered dV/V curve (Figure 31, bottom panel, black line). During the second quiescent period, July 31 to November 18, dV/V increased by +0.223 % measured on the 1 day, 0.5-4Hz filtered dV/V curve (Figure 31, top panel, black line); +0.227% measured on the 1 day, 0.5-2Hz filtered dV/V curve (Figure 31, middle panel, black line); and +0.249% on the measured on the 1 day, 2-4Hz filtered dV/V curve (Figure 31, bottom panel, black line).

These results are consistent with the relative velocity change trend observed at Piton de la Fournaise, using the 10 day [Brenguier *et al.*, 2008b] and the improved 1 day resolution [Baig *et al.*, 2009]. The 10-day stacks showed drops in velocity prior to onset of eruption that we also observed in our 10-day stacks, while the 1 day showed increases in relative velocity prior to eruptive onset, followed by post-eruption onset drops [Baig *et al.*, 2009]. The 10 day stacks have the effect of averaging the velocity change over a long time window, which impeded the ability to detect real time changes in velocity [Baig *et al.*, 2009]. The velocity drop may not be a precursor, but could occur anytime within the 10 day window. The velocity drops occurred on the order of hours to a few days and a small time window was needed to determine the exact onset. The dilation correlation coefficient (DCC) method allowed determination of relative velocity changes with the resolution of up to 6 hours using single component, ZZ, correlations and assessed the quality of the measurements by calculating the correlation coefficient and minimum acceptable level of fluctuation, without having to design and apply special denoising filters.

Additionally, we did not observe a long term seasonal trend in our dV/V measurements that was observed at Mt. Merapi [Sens-Schönfelder and Wegler, 2006], Piton de la Fournaise [Brenguier, *et al.*, 2008a,b], and in the Los Angeles basin [Meier *et al.*, 2011]. Seasonal

variability may result from close proximity of these settings to the coast. These studies also used longer period ambient noise that may be more sensitive to regional scale, seasonal changes. By using the 0.5-4 Hz band with a narrow array velocity changes due to local scale volcanic changes may be better resolved and larger regional fluctuations reduced or eliminated.

Chapter 7

DISCUSSION AND CONCLUSIONS

7. Discussion: Comparison of dV/V results with volcanic activity during 2010 at Tungurahua Volcano

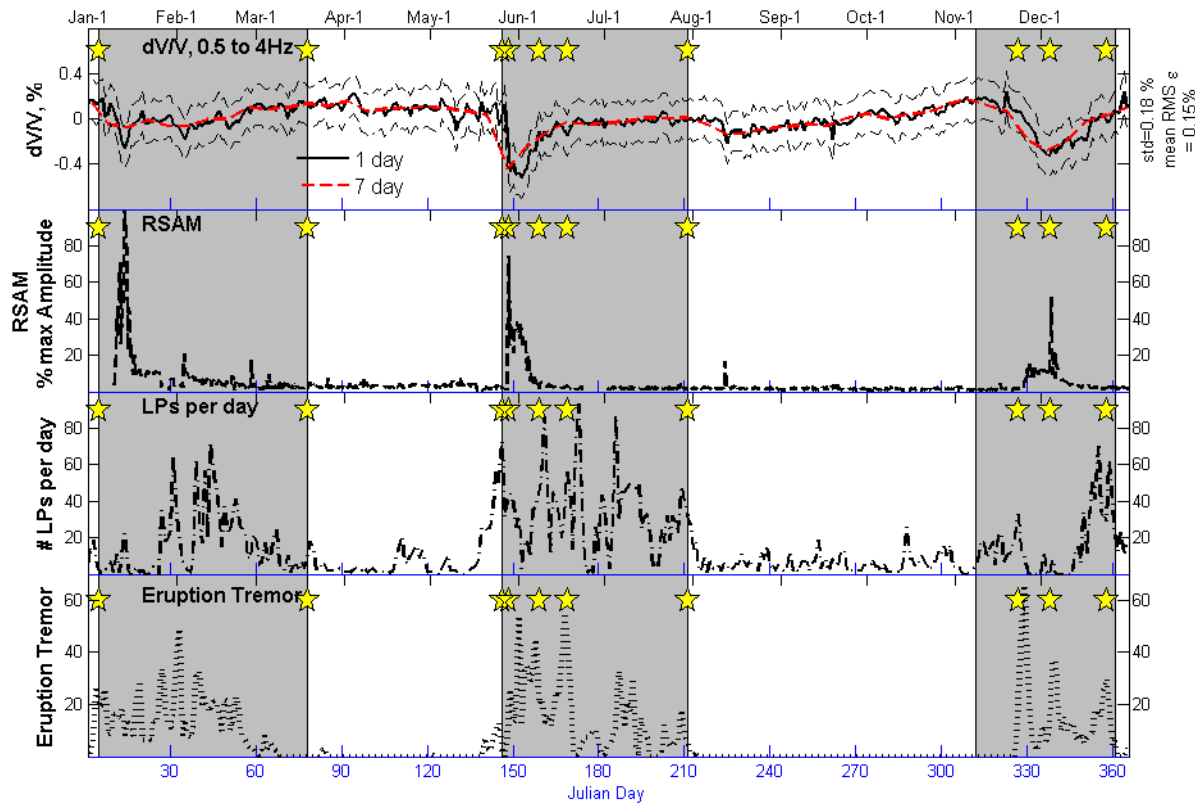


Figure 32. (top panel) % dV/V for 1- (thick solid black line) and 7 day-stacks (dashed red line) averaged over all stations and station pairs with 1 σ standard deviation bars (thin dashed line). Also plotted are significant eruptions noted in the text (yellow stars) and gray bars that indicate the three episodes of increased volcanic activity. RSAM (2nd panel, dashed line), number of LPs (3rd panel, dot-dashed line) and number of eruption tremor waveforms (4th panel, horizontal bars) recorded per day are plotted in the three panels below the top, respectively. CFs were band-passed filtered in 0.5-4Hz (wide-band) prior to calculation of dV/V.

During the time period of interest Tungurahua volcano experienced 3 major episodes of Strombolian to Vulcanian style eruptive activity: (1) January to March 2010, (2) late May to June 18th paroxysmal crisis with continued moderate activity through July, and (3) mid-November to December 2010. For each of these episodes of activity, the dV/V curves showed a cyclical trend of large, steep drops in dV/V immediately following the onset of eruptive activity, with troughs occurring at the same time as the most active period of eruption, followed by a slow recovery. During the quiescent periods, in between the episodes of active eruption, dV/V gradually increased. The 1 and 7 day averaged, 0.5-4Hz filtered dV/V trends were compared with three measures of volcanic activity: (1) average RSAM, (2) number of LPs and (3) number of eruption tremor waveforms per day (Figure 32). The RSAM was calculated as the RMS amplitude of each 6 hour record of vertical component seismic data normalized to the percent deviation from the maximum amplitude, while the number of LPs and eruption tremor events were tabulated by the IGEPN.

7.1. Active Episode 1: January 5th to March

The first episode began on January 5th, 2010, with the eruption of a gas and ash plume that rose to an elevation of ~6.5 km a.s.l. Following the start of the first active eruption episode the relative velocity dropped 0.41% to the minimum value measured on January 14th, on the 1-day stack, 0.5-4Hz filtered dV/V curve (Figure 32, top panel). Moderate eruptive activity producing ash plumes and falls, as well as some Strombolian activity into late February coincided with the region of depressed, but gradually increasing dV/V, while the decrease in activity in the waning stages of the eruptive episode in late February was mirrored by the recovery of the dV/V curve to levels close to zero.

7.2. 1st Quiescent Period: March 20th to May 26th

After activity associated with the first eruptive episode ceases, the relative velocity trend continued to gradually increase. Between the end of the first and onset of the second eruptive episodes, March 20 to May 25, dV/V increased by +0.151 % (Figure 31). A slight increase in the number of LPs recorded occurs in late April that did not appear to correspond to any change in the dV/V trend (Figure 32, third panel) and the RSAM (Figure 32, second panel) and eruption tremor (Figure 32, bottom panel) curves remained close to zero.

The wide band (0.5-4 Hz) and low frequency band (0.5-2Hz) dV/V curves did not show precursory changes other than rapidly fluctuating, slightly higher amplitude values in the days prior to the May 26 and 28 eruptions that were the start of the second active episode. The high-frequency curve did show a precursory downward trend in the dV/V values beginning in early May that also corresponded to a rapid increase in the number of recorded LPs a (Figure 32, third panel) and increase in the eruption tremor (Figure 32, bottom panel).

7.3. Active Episode 2: May 26th to June 18th with moderate activity through July

The second and most intense episode of activity began May 26-28, 2010. Following the onset of eruption, in a pattern that was similar to that of the first episode, dV/V dropped rapidly immediately following the initial eruptions for the duration of the sustained high eruptive activity that follows and recovers as eruptive activity wanes. The difference between dV/V at the start of the active episode and the minimum measured dV/V was 0.53% for episode 2 (June 2), measured using the 1 day, 0.5-4Hz filtered dV/V curve (Figure 32, top panel). The trough of the dV/V curve appeared to coincide with a major swarm of volcanic explosions and the recording of hundreds of seismic events that occurred for several days following the May 28th eruption [Lees et al, 2012]. The rapid increase in dV/V that occurred during the first half of

June, from ~ June 1 to ~June 18, coincided with the period in which harmonic tremor tapers off [Lees et al, 2012]. The intense eruptive activity was reported by the IGEPN to reach its peak around June 8-9. On June 8 the maximum measured SO₂ released was 4030 tons. At the same time tilt measurements at three stations (RETU, BILBAO, and PONDOA) indicated a small inflation

Between June 18 and Aug 1 the dV/V showed a slight upward trend, while volcanic activity continued at a moderate level. The number of LPs recorded fluctuates, but remained high (Figure 32, third panel) , while the level of tremor was high, but lower than between May 26 and June 18 (Figure 32, bottom panel). A series of explosions recorded by the seismic network on July 27th did not appear to alter the trend of the dV/V curve, though it was accompanied by a release of 3207 tons of SO₂ and a slight inflation recorded on the tiltmeters at RETU, BILBAO, and PONDOA. The last reported plume of steam and ash occurred on July 30th.

7.4. 2nd Quiescent Period: August to mid-November

Over the duration of the second quiescent period, from July 31st to November 7th, dV/V gradually increased by +0.223 % (Figure 31), which was greater than for the first quiescent period. There was no precursory decrease in the 2-4 Hz dV/V curves, unlike the decrease that occurred prior to the May 26th eruption. The onset of the third eruptive episode also differed from the second episode in its eruptive characteristics; the onset of activity during the third eruptive episode was more gradual, while the first episode activity increased sharply, triggered by the May 26th and 28th large eruptions. This may indicate differing dominant eruption mechanisms between the two episodes.

7.5. Active Episode 3: mid-November to December 27th

The last episode of major eruptive activity in 2010 began with a gradual increase in seismic activity at the end of October followed by Vulcanian style eruptions beginning in the second week of November. Starting in October and continuing into November, the number of LPs recorded by the IGEPN gradually increased from 31 recorded events in the first week of October to 87 recorded during the final week of October, to 112 recorded in the second week of November, the week eruptions began. The first week of November the number of recorded LPs dropped to 14. The number of LPs recorded per day during this last episode remains lower than in the second episode (Figure 32, third panel).

During this period of gradual increase in volcanic activity dV/V gradually decreased between the start of the episode to the minimum by 0.49% (December 4), measured using the 1 day, 0.5-4Hz filtered dV/V curve (Figure 32, top panel). The steepest drop in the dV/V curve occurs following the large November 22nd eruption and continued into early December. The trough of the dV/V curve corresponds with the December 4th eruption that produced the 1 km long La Hacienda quebrada lava flow. This was again followed by a slow increase in the dV/V curve until volcanic activity ends, after moderate size explosions on December 24-25th, eruptive activity at Tungurahua decreased and explosions ceased by the end of the first week on January 2011. This decrease in explosive activity was accompanied by a decrease in recorded earthquakes, a deflation recorded in the tilt and decreasing SO_2 emissions.

7.6. Discussion: Possible causes of dV/V changes at Tungurahua

At Tungurahua, changes in relative velocity, dV/V , appear to correspond to cyclical changes in eruptive activity. Steep drops in dV/V occur immediately following the onset of eruptive activity, with troughs occurring at the same time as the most active period of eruption,

followed by a slow recovery as eruptions wane. Quiescent periods were characterized by gradual increased in dV/V . A definite pattern of precursory velocity changes was not observed; a precursory drop in velocity was observed only for the second episode and on the 2-4Hz filtered dV/V curve. No increases in velocity prior to eruption were observed. The dV/V curve did appear to give an indication of the intensity of eruptive activity. Episode 2 had the most intense eruptive activity, decreasing for episode 3 and then episode 1, which corresponded to dV/V drops of 0.53%, 0.49% and 0.41%, respectively. The periods of the largest drops also correspond to the time period in which eruptive activity was greatest. Recovery of pre-eruption dV/V levels occurs as eruptive activity decreases.

The close correspondence of decreased velocity with increased eruptive activity suggests a source that is directly related to eruption processes. These include fracturing and dilation due to pressurization in the magmatic and/or hydrothermal system, shallowing of fragmentation depth, deepening of the water exsolution depth, or dispersive waves that propagate in fluid filled cracks. Prior to eruptions, intrusions of magma into the conduit system lead to a pressurization of the conduit system and inflation of the volcanic edifice [Brenguier *et al.*, 2008b]. A deepening of the exsolution depth and fragmentation depth, resulting in the generation of trapped volatile bubbles also contributed to the pressurization of the conduit system [Haney *et al.*, 2009]. This pressurization could cause the increase in velocity prior to eruption onset, while the sudden release of this pressure by eruption [Garces *et al.*, 2000] could result in the drops of relative velocity following the onset of eruption. Continued release of magma and volatiles through eruptions and degassing could cause the depressed dV/V that occurred for the duration of the eruptive episode. The decline in the level of eruptive activity correlated to gradual recovery of pre-eruptive levels of dV/V .

It has also been suggested that inversely dispersive waves propagating in fluid filled cracks, the “crack” or “slow” waves that generate LP events [Chouet, 1996], could result in the drops in velocity [Haney *et al.*, 2009]. These waves have the property that their phase and group velocities decrease with an increasing ratio of wavelength-to-conduit thickness and a narrowing of the conduit due to depressurization following eruption would correspond to a decrease in velocity. This mechanism did not appear to dominate the dV/V trends at Tungurahua. If the presence of inversely dispersive propagating waves, recorded as LP events, caused velocity drops then the dV/V curve would more closely mimic the LP trend; low velocity spikes would correlate to increased number of LPs. This mechanism did not explain why there was a gradual increase in velocity prior to eruption during periods that lack an LP activity. While, additional, non-stationary (moving) sources from increased LPs appeared to contribute to some of the velocity decrease, in the 0.5-2 Hz band, during the second eruptive episode at Tungurahua, the contribution to other periods of activity was less certain. Further study is needed to quantify how the added LP sources affect the dV/V trends.

7.7. Conclusions

The close paralleling of the dV/V curve with eruptive activity makes it a promising method for monitoring eruption intensity, but not for a predictive tool to forecast eruption onset. The RSAM curve shows peaks in seismic activity that does not always correspond to peaks in eruptive activity. Precursory increases in the number of LP and eruption tremor events are observed for the first and second eruptive episodes, but less so for the third. Eruption intensity is also not as closely correlated to LP and tremor activity as the dV/V curve. The dV/V curve appears to more closely correlate with the eruptive activity better than these other measures of volcanic activity.

The different eruptive characteristics of episode 2 and 3 are also reflected in the measured velocity changes. Episode 2 dV/V drops dominate in the LP band and are not as closely tied to gas emissions. Potentially dV/V changes could be tied to the same mechanisms inferred to result in LP events, i.e. vibrating fluid filled conduit. Episode 3 on the other hand has a similar shape regardless of the band and appears to have spikes coinciding with lava eruptions (flow or Strombolian effusions). While the steepest drop coincides with LP and tremor numbers the dominant source may not be vibrating fluids, but to pressurization and fracturing due to influx of gas or magma. Future work is needed to identify the source of the dV/V changes and to quantify the effect of non-stationary sources (i.e. LP and other seismic events) on relative velocity measurements.

Chapter 8

EQUIPARTITIONING OF THE AMBIENT NOISE FIELD AT TUNGURAHUA VOLCANO, ECUADOR, 2010

8. Background and Methods

8.1. Background: Equipartition of a diffuse wavefield

Equipartition is a key assumption in derivations of the Green's function from the ambient noise wavefield. Equipartition refers to the concept that in a diffuse (random) wavefield the average energy densities at any given place for any given mode (Rayleigh, P, S, etc.) are equal [Shapiro *et al.*, 2000; Weaver, 2010]. For ambient seismic noise in a large, open system the local wavefield may be diffuse, the result of a continuous and random distribution of sources and scattering, but not equipartitioned [Weaver, 2010]. In the case of ambient noise surface wave tomography, it is generally assumed that by averaging ambient noise wavefield correlations over a year or more, that a kind of local equipartition can be achieved where all modes of the regional wavefield are equally energetic and the Green's function can be retrieved. For continuous monitoring, with shorter averaging times, it becomes important to measure the extent of equipartition in the local seismic wavefield. Temporal changes in the direction and strength of the local wavefield impedes the retrieval of the Green's function and accurate measurements of seismic velocities and other elastic parameters [Roux *et al.*, 2009; Lawrence *et al.*, 2011] as well as helps to differentiate the source of relative velocity changes, dV/V . In spite of this, few previous studies have attempted to measure the equipartition of the local wavefield.

The purpose of this work is to characterize the equipartition of the wavefield at Tungurahua Volcano, Ecuador and use this information to characterize potential sources of velocity changes associated with eruptions. Previously, it was shown that the Green's function of a medium could be retrieved from the correlation of recordings of the ambient noise wavefield [e.g., Lobkis and Weaver, 2001; Sneider, 2004; Weaver and Lobkis, 2004; Wapenaar, 2004; Roux, *et al.*, 2005]. A fully equipartitioned diffuse field develops in a heterogeneous medium as a result of multiple scattering of a wave. Partition between energies is reached when a wave has encountered a sufficient number of scatterers [Shapiro *et al.*, 2000]. The partition of a measured ambient noise field has been previously estimated from two energy ratios, (1) the shear to compressional energy ratio, $R=W_s/W_p$ [Shapiro *et al.*, 2000; Hennino *et al.*, 2001; Margerin *et al.*, 2009], and (2) the horizontal-to-vertical kinetic energy ratio, H/V , [Hennino *et al.*, 2001; Margerin *et al.*, 2009].

8.2. Background: Testing equipartition and S-to-P energy density ratio

Shapiro *et al.* [2000] developed the equations to describe the ratio of S-to-P energy or the ratio of the energies of the curl to the divergence of ground displacement using the radiative transfer theory [Wu, 1985]. Radiative transfer theory quantitatively describes the arbitrary orders of scattering and intensity in a complex medium that cannot be accounted for by models of single scattering and diffusion [Shapiro *et al.*, 2000]. The S-to-P energy ratio is an equilibration ratio and does not necessarily imply equipartitioning, although equipartitioning implies equilibration [Paul *et al.*, 2005]. This equilibration will occur even when the energy flux distribution is strongly directional (i.e. direct wave).

The energy ratio, $R=W_s/W_p$, can be used to estimate when the wavefield reaches equilibrium and is locally equipartitioned [Shapiro *et al.*, 2000]. The ratio is calculated as,

$$R = \frac{\frac{\mu}{2}(\text{curl } \vec{u})^2}{(\frac{\lambda}{2} + \mu)(\text{div } \vec{u})^2} = \frac{1}{4} \left(\frac{\alpha}{\beta} \right)^2 \frac{4 \frac{\partial u_z^2}{\partial x} + 4 \frac{\partial u_z^2}{\partial y} + \left(\frac{\partial u_x}{\partial y} - \frac{\partial u_y}{\partial x} \right)^2}{\left(\frac{\partial u_x}{\partial x} - \frac{\partial u_y}{\partial y} \right)^2}$$

The spatial derivatives of the displacement are calculated for a square array of four stations as,

$$\frac{\partial u_i}{\partial x} = \frac{u_i^3 - u_i^1}{d}, \frac{\partial u_i}{\partial y} = \frac{u_i^2 - u_i^4}{d}, i = x, y, z$$

where u_i^n is the displacement at station, n , and d is the distance between opposite stations of the array, $\sim 71\text{m}$. For events recorded at only 3 stations the spatial derivatives are calculated as

$$\frac{\partial u_i}{\partial x} = \frac{u_i^3 - u_i^1}{d}, \frac{\partial u_i}{\partial y} = \frac{u_i^2 + u_i^3 - 2u_i^4}{d}, i = x, y, z$$

Their study uses the calculation of this energy ratio to characterize the state of equipartition in the lithosphere using a seismic array installed at Chilpancingo, Guerrero, Mexico. They apply their technique to coda of 13 local earthquakes in the vicinity of the array, which are band-passed from 0.1 to 0.5 Hz (2 to 10s). Earthquake coda are composed of waves multiply scattered by small-scale heterogeneities in the Earth [Aki, 1969], which results in a diffuse wavefield, the correlations of which can be used to retrieve the Green's function such as with ambient noise correlations. The study at Chilpancingo, Mexico [Shapiro *et al.*, 2000; Hennino *et al.*, 2001] and subsequent observations at the Pinyon Flats Observatory seismic array [Margerin *et al.*, 2009] show that the S-to-P energy ratio varies rapidly during the onset of the direct arrival of the earthquake and stabilizes for during the coda. The ratio does not vary more than about 25% of the mean value in the coda window, while the energy decreases by a factor of 10,000 [Shapiro *et al.*, 2000]. They also observe that conditions at the surface affect the equilibration of the energy ratio, W_s/W_p , and consequently the local equipartition. Lower energy ratios than are predicted by theory are observed in the Chilpancingo and Pinyon Flats

studies [Hennino *et al.*, 2001; Margerin *et al.*, 2009]. The discrepancy between the observed and predicted energy ratios is explained by the interference of incident and reflected wavefields at the surface [Margerin *et al.*, 2009]. Work by Margerin *et al.* [2009] to model energies in a layered model that can account for surface conditions, is able to account for the lower S-to-P energies as well as shows the depth dependency of the energy ratios (Figure 33).

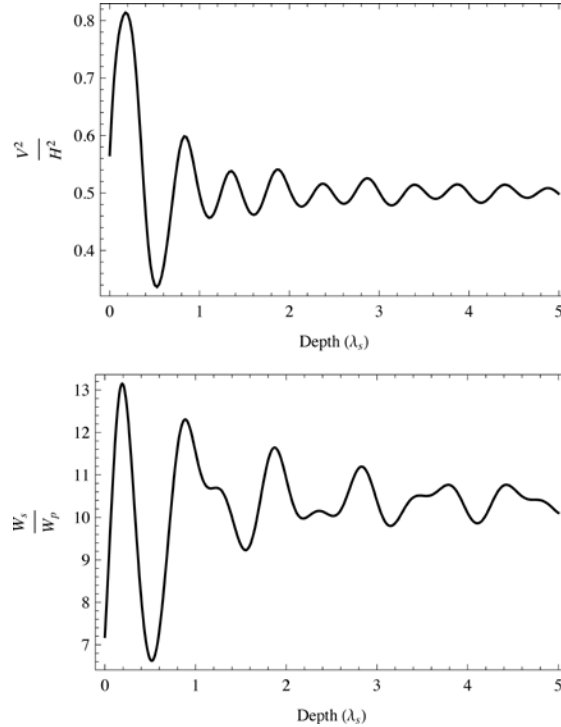


Figure 33 Depth dependence, measured as a function of the shear wavelength λ_s , of energy ratios for equipartitioned elastic waves calculated for a homogeneous elastic half-space. The depth kernels are calculated for the shear to compressional deformation energy ratio (Bottom) and the vertical to horizontal kinetic energy ratio (Top). (source: Margerin *et al.*, 2009)

8.3. Background: H/V Ratio and equipartition

The horizontal-to-vertical kinetic energy ratio, H/V, equilibrates like the S-to-P energy ratio and can also be used to test for equipartition [Hennino *et al.*, 2001; Margerin *et al.*, 2009]. First proposed by Nogoshi and Igarashi [1971], the H/V ratio is calculated as the ratio between the Fourier amplitude spectra of the horizontal (N and E) components to the vertical (Z)

component amplitude spectra. The H/V ratio is easier to calculate than the S-to-P ratio and can be calculated at individual stations. Site conditions and resonance frequency also can be estimated using the H/V ratio [e.g., Nakamura, 1989; Bonnefoy-Claudet *et al.*, 2006; Lermo and Chávez-García, 1993]. I use the H/V ratio to characterize the equipartition of the seismic wavefield at Tungurahua and characterize the differences in the wavefield at individual locations that affect the retrieval of the Green's function.

Although, the physical basis for the equilibration of the horizontal-to-vertical kinetic (H/V) energy ratio is not well constrained [Hennino *et al.*, 2001; Margerin *et al.*, 2009] some initial work has been done to relate the H/V ratio to the average energy density of the wavefield by calculating the H/V ratio as a function of the imaginary part of the Green's function [Sánchez-Sesma *et al.*, 2011a, b]. By relating the H/V ratio to the component energy densities one can estimate the various contributions of body and surface waves to the ratio.

The retrieval of the Green's function from correlations of ambient noise, as previously described, implies that the average energy densities of a diffuse field is proportional to the imaginary part of the Green's function [Sánchez-Sesma *et al.*, 2008, 2011a, b; Perton *et al.*, 2009]. Following the terminology of Sánchez-Sesma *et al.* [2008, 2011a, b], the auto-correlation of the displacement vector field, $u_i(\mathbf{x}, \omega)$, of a diffuse field measured at stations 1 can be written as

$$\left\langle u_i(\mathbf{x}_1, \omega) u_j^*(\mathbf{x}_1, \omega) \right\rangle = -2\pi E_s k^{-3} \text{Im} \left[G_{ij}(\mathbf{x}_1, \mathbf{x}_1, \omega) \right] \quad (4)$$

Where E_s is the average energy density of shear wave, the shear wavenumber is $k = \omega/\beta$, and the Green's function $G_{ij}(\mathbf{x}_1, \mathbf{x}_2, \omega)$ is the response at station 1 in direction i to a force acting at

the same location in direction j . The total energy density, $E(\mathbf{x}_1)$, measured at station 1 can be found by rewriting (4),

$$\begin{aligned} E(\mathbf{x}_1) &= \rho \omega^2 \langle u_m(\mathbf{x}_1) u_m^*(\mathbf{x}_1) \rangle \\ &= -2\pi\mu E_s k^{-1} \text{Im}[G_{ij}(\mathbf{x}_1, \mathbf{x}_1)], \end{aligned} \quad (5)$$

where $\mu = \beta^2 \rho$.

The H/V ratio can be written in terms of the energy densities $E_i(\mathbf{x}, \omega)$, $i = Z, N, E$ of each component (Z, N, and E),

$$[H/V](\omega) = \sqrt{(E_E(\mathbf{x}, \omega) + E_N(\mathbf{x}, \omega)) / E_Z(\mathbf{x}, \omega)}, \quad (6)$$

which can be rewritten in terms of the imaginary component of the Green's function using (5),

$$[H/V](\omega) = \sqrt{\frac{(\text{Im}[G_{EE}(\mathbf{x}, \mathbf{x}; \omega)] + \text{Im}[G_{NN}(\mathbf{x}, \mathbf{x}; \omega)])}{\text{Im}[G_{ZZ}(\mathbf{x}, \mathbf{x}; \omega)]}} \quad (7)$$

The development of this theory is important in understanding how the relative contributions of body and surface waves in a wavefield contribute to the amplitude and resonance frequency obtained from the H/V ratio. Various authors have debated whether to attribute the peak H/V amplitude to the dominance of Rayleigh wave motion (Lermo and Chávez-García, 1993; Fäh *et al.* 2001) or body waves (e.g., Nakamura, 1989; Bonnefoy-Claudet *et al.*, 2006). Sánchez-Sesma *et al.* [2011b] obtains the theoretical energy partition from the theoretical H/V ratio, calculated using (7) and given a model where a horizontal (tangential) and vertical (normal) force is applied at the surface of an elastic half-space with a Poisson ratio of 1/4. For a horizontal force, the theoretical partition between modes is 18% Rayleigh, 60% *SH*-, 16% *SV*-, and 6% *P*-waves. For a vertical force the theoretical partition

between modes is 67% Rayleigh, 26% SV-, and 7% P-waves. The vertical force produces a wavefield that is dominated by surface waves that are insensitive to deep structures at higher frequencies. The horizontal force case produces body waves that may interact with deeper layering [Sánchez-Sesma *et al.*, 2011b]. The contribution of different types of waves to the H/V ratio clearly depends on the type of source producing the wavefield, which may explain the contradictory results from previous research.

8.4. Methods: Data and initial processing

I use the H/V ratio, calculated from the ambient noise amplitude spectra, to characterize the local equipartition of the seismic wavefield and differences in the wavefield at individual locations that affect the retrieval of the Green's function at Tungurahua in 2010. I use the same dataset as used in the previous section, describing changes in the relative velocity, dV/V , which consists of the continuous seismic time-series records from 5 broad-band seismometers in 2010, deployed around the flanks of Tungurahua volcano, Ecuador by the Instituto Geofísico Escuela Politécnica Nacional (IGEPN), (see Figure 34). Processing the ambient noise recordings was done as previously for calculation of 6-hour correlation functions (see Chapter 5.1, pp.70). Each component of the daily seismic record was demeaned, detrended and band-passed filtered from 0.5-4 Hz and cut to 6-hour long segments. To reduce the effect of earthquakes that could mask the ambient noise signal, a temporal running-absolute-mean and sign-bit normalization [Bensen *et al.*, 2007] was applied to each 6-hour-long record.

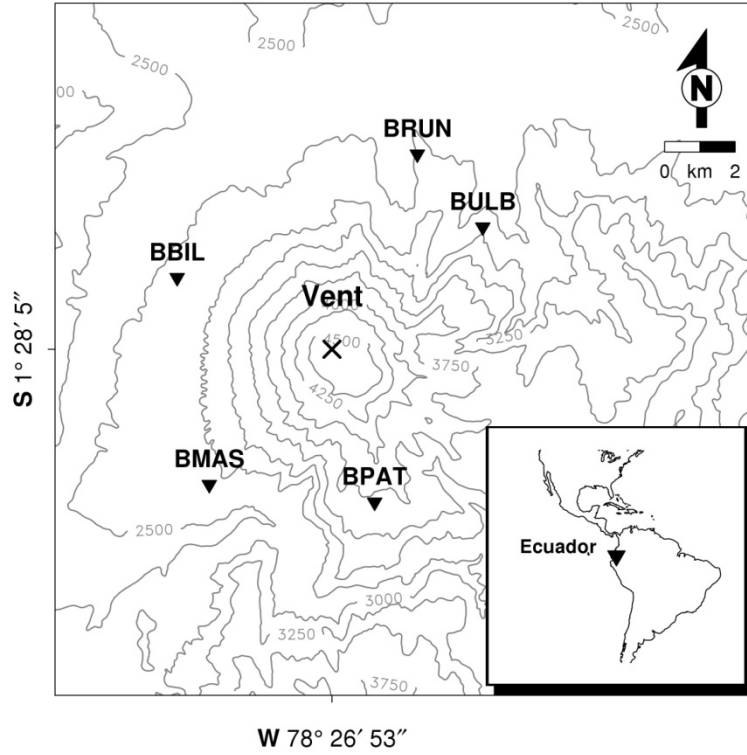


Figure 34. Map of station locations for the IGEPN broadband seismic array at Tungurahua Volcano, Ecuador deployed in 2010. Topographic contour spacing is every 50 meters. (Source: Keehoon Kim)

8.5. Methods: H/V Ratio

First, the Fourier amplitude spectra of each component (Z, N, E) of each 6-hour noise record was calculated (see Figure 38-Figure 39) for each of the five broadband stations (BBIL, BRUN, BPAT, BMAS, BULB) deployed on Tungurahua Volcano in 2010. Each power spectra is smoothed using a 0.01 Hz window and the H/V ratio is calculated (see Figure 38-Figure 39). H/V is calculated as the square root of the ratio of the average of the horizontal component power spectra and the vertical power spectra, $H/V = \sqrt{\langle N^2, E^2 \rangle / Z^2}$, where the brackets indicate the average of the horizontal component (N,E) power spectra and Z^2 is the vertical power spectra (SESAME, 2005). The peak H/V ratio is found from the maximum value of the frequency dependent H/V in each of the three bandwidths of interest: 0.5-4 Hz (wide-band),

0.5-2 Hz (low frequency) and 2-4 Hz (high frequency). Figure 45-Figure 47 show the peak H/V curve calculated at each station in 2010 and the spatially averaged peak H/V for each frequency band.

Chapter 9

SPECTROGRAM AND H/V RESULTS

9. Results

9.1. Spectrograms and spectral content of the ambient noise wavefield

Figure 38-Figure 39 show the spectrograms calculated for each 6-hour ambient noise record from the horizontal (N, E) and vertical (Z) components at the five broadband stations (BBIL, BRUN, BPAT, BMAS, BULB) deployed on Tungurahua Volcano in 2010. The power spectra are calculated for each 6-hour long record of ambient noise and smoothed using a 0.01 Hz window. During active eruptive episodes, the peak spectral content of the ambient noise field at Tungurahua shifts to lower frequencies, below ~ 2.5 Hz. This corresponds to the dominant frequency band of LP events recorded at Tungurahua (K. Kim, pers. comm., 2013). During quiescent periods with decreased volcanic activity, the power spectra have weaker peak amplitudes, with the exception of the spectra at BBIL, and are shifted to higher frequencies.

The spectra at station BULB are shown in Figure 35. During the three active eruptive episodes, the spectra calculated at station BULB (NE flank) show strong peaks at frequencies less than ~ 1.1 - 1.6 Hz. The vertical component shows four strong peaks at 0.9, 1.1, 1.2, and 1.6 Hz during all three active episodes. On the N-component spectrogram, three to four peaks at 0.7, 0.8, 0.9, 1.3 Hz are observed and two peaks, a broad peak from 0.6-0.8 Hz and a narrow peak at 1.1 Hz, are observed on the E-component spectrogram. During periods of low activity,

the spectral peaks have weaker amplitudes, are located at higher frequencies, and span a larger range of frequencies than the peaks occurring during the active episodes. On the vertical component there are amplitude peaks located at 1.5, 2, and 2.5 Hz. The amplitude of the peaks that follow the second eruptive episode is greater than those following the first eruptive episode. N-component shows a broad peak between 3.4-4Hz, while the E-component shows two broad peaks, from 1.3-1.5Hz, 2.5-2.7 Hz, and a narrower peak at 3.7 Hz.

A similar pattern of spectral peaks are observed at station BPAT (see Figure 36), located clockwise south from BULB, except the spectral bands are weaker on the vertical component and are almost absent from the horizontal components during the active eruptive episodes. Over the duration of each of the active episodes, the peak bands on the vertical component occur at 1 and 1.3 Hz and are not continuous. The peak bands on the horizontal components are weak and distributed across almost the full band width, from 0.8 to 3.7 Hz. On the N-component there are weak harmonics at 1, 2, and 3 Hz and a strong, broad peak at 3.4 and 3.7 Hz, which both continue into the quiescent periods, though shifted towards the higher frequencies by 0.1 Hz. On the E-component there are six bands at 1.6, 1.8, 2.2, 2.4, 2.8, and 3.3Hz during the active episodes and a peak at 3.5 Hz during the quiescent periods.

During the quiescent periods of low activity the spectral peaks are, in general, lower in amplitude and shifted slightly to higher frequencies at station BPAT. On the vertical component there are two sets of weak, broad peaks located between 1.3-1.6 Hz and 2-2.6 Hz. The amplitude of the peaks that follow the second eruptive episode is greater than those following the first eruptive episode. The N-component shows a broad peak between 3.4-4Hz, while the E-component shows two broad peaks, from 1.3-1.5Hz, 2.5-2.7 Hz, and a narrower peak at 3.7 Hz.

The set of spectral amplitude peaks calculated at station BMAS (SW flank, Figure 37) occur in the frequency band from 1-3.3 Hz, during both the active and quiescent times. During the active periods there are additional bands at lower frequencies and the spectral amplitudes are, in general, stronger. During the quiescent periods of low volcanic activity, a set of multiple peaks are present over a range of frequencies from 1.4 to 2.7 Hz, observed on the vertical component. During the active episodes the amplitudes of the peaks located at 1.6 and 1.8 Hz increase. Another set of peaks from 1.3-3.3 Hz with distinct bands at 1.4, 1.7, 2.5, 2.8 and 3.3 Hz are present on the N-component during the quiescent periods. During the three active episodes the amplitudes of the peaks at 1.4, 1.7, and 2.8 Hz increase, an additional amplitude peak appears at 1 Hz and the 3.3 Hz peak disappears. On the E-component, during the quiescent periods, a broad set of peaks from 1.3-2.7 Hz with distinct, higher amplitude bands at 1.4, 1.7, 2.1, and 2.5 Hz are observed, while during the active episodes there are four strong peaks at 0.9, 1.1, 1.2, and 1.6 Hz.

The spectrograms calculated for BBIL(Figure 38) show 1-2 dominant peaks during the quiescent periods that disappear during the active episodes and a broad set of low frequency (<2.5 Hz), generally lower amplitude peaks during the active episodes. On the vertical component during the quiescent period there are two strong peaks at 2.4 and 2.6 Hz that dominate the spectra. During the active episodes there are a set of lower amplitude peaks from 0.8-2.5 Hz. The N-component shows peaks at 1.5, 2.2, 2.6, and 2.8 Hz, while the E-component shows peaks at 1.6, 2.2, 2.3, and the strongest peak at 2.5 Hz during the quiescent periods. During the active episodes the bands of peaks are lower in amplitude and shift to the lower frequencies, from 0.8 to 2.2 Hz on the horizontal (N,E) components.

The spectra of BRUN, located next to a canyon, are shown in Figure 39. During the quiescent period, the vertical component of BRUN shows a strong peak shifted to the highest frequency in this study, which is quite different from the other stations, while during the eruptive episodes there are peaks at 1, 1.3, and 1.6 Hz. The N-component shows a set of peaks from 1.7 to 2.7 Hz, with the strongest amplitude at 1.7 Hz, and a strong peak at 3.4 Hz, during the quiescent periods. While on the E-component there are two strong peaks at 2 and 2.4 Hz, with some weaker peaks at 2.7, 3 and 3.5 Hz, during the quiescent periods. During the active episodes, the bands of peaks shift to the lower frequencies with a strong peak at 1.6 and 1.8 Hz, and a set of lower amplitude peaks that range from 0.7 to 2.1 Hz on the N component. On the E-component, there are strong peaks at 0.7, 1, 1.5, and 1.8 Hz, during the active episodes.

9.2. Results Figures: Spectrograms

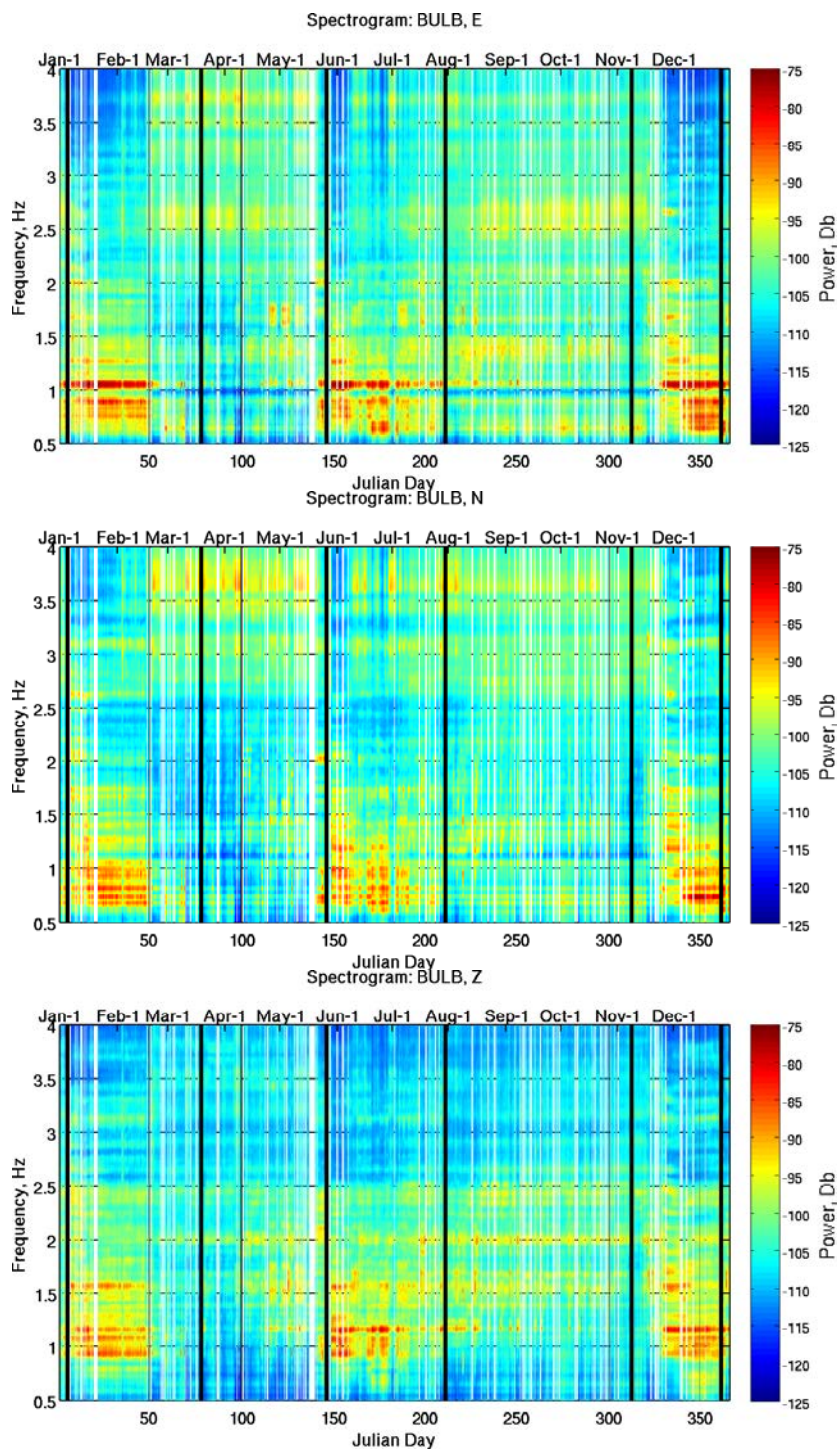


Figure 35. Spectrogram for BULB, calculated from each 6-hour ambient noise record for the two horizontal components, East-West (E, top panel), North-South (N, middle panel), and vertical (Z, bottom panel) component at Tungurahua Volcano in 2010. The horizontal axis indicates the day in 2010, the vertical axis the frequency, and the colors represent the smooth amplitudes of the power spectra in decibels (Db).

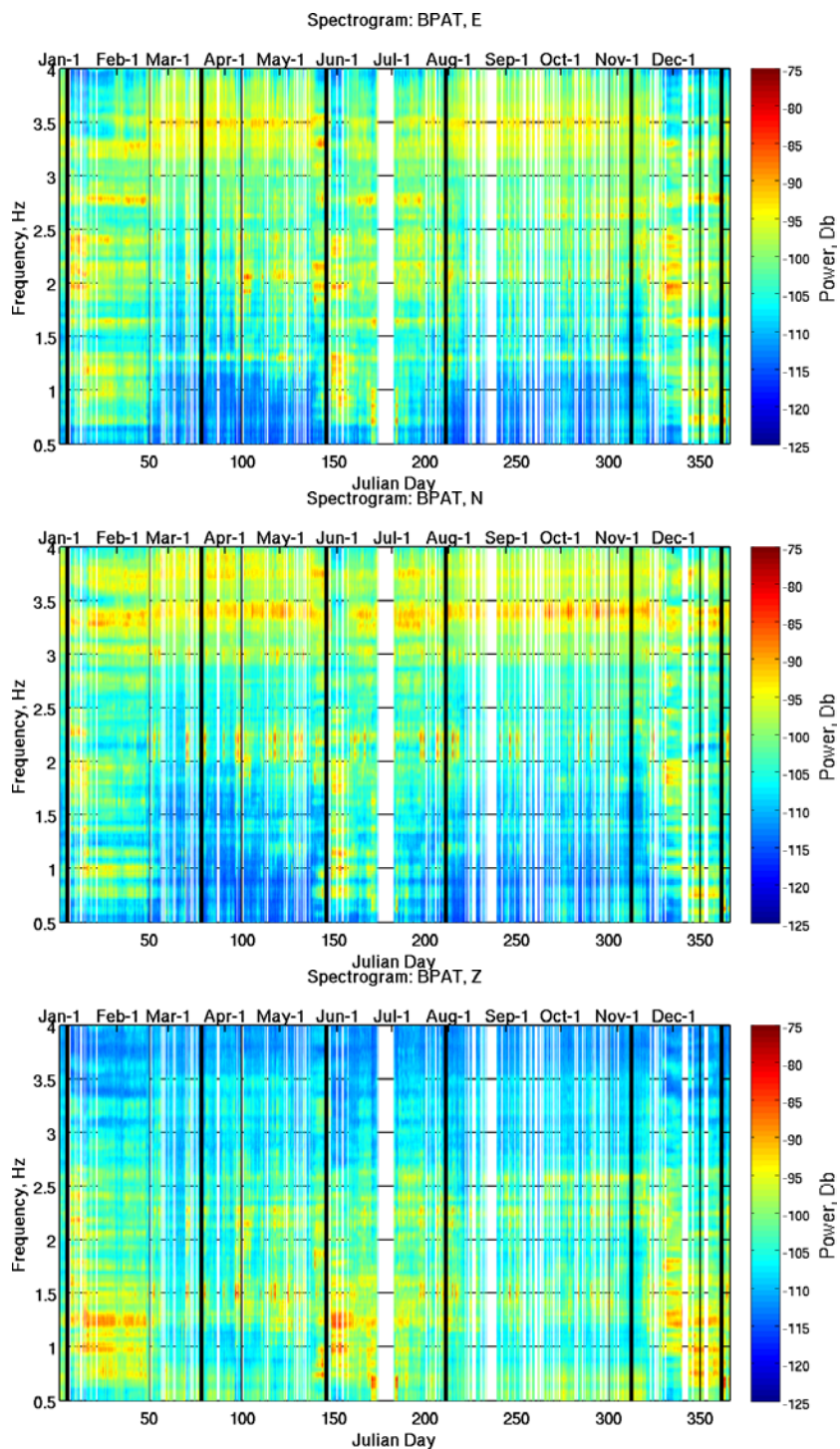


Figure 36. Spectrogram for BPAT, calculated from each 6-hour ambient noise record for the two horizontal components, East-West (E, top panel), North-South (N, middle panel), and vertical (Z, bottom panel) component at Tungurahua Volcano in 2010. The horizontal axis indicates the day in 2010, the vertical axis the frequency, and the colors represent the smooth amplitudes of the power spectra in decibels (Db).

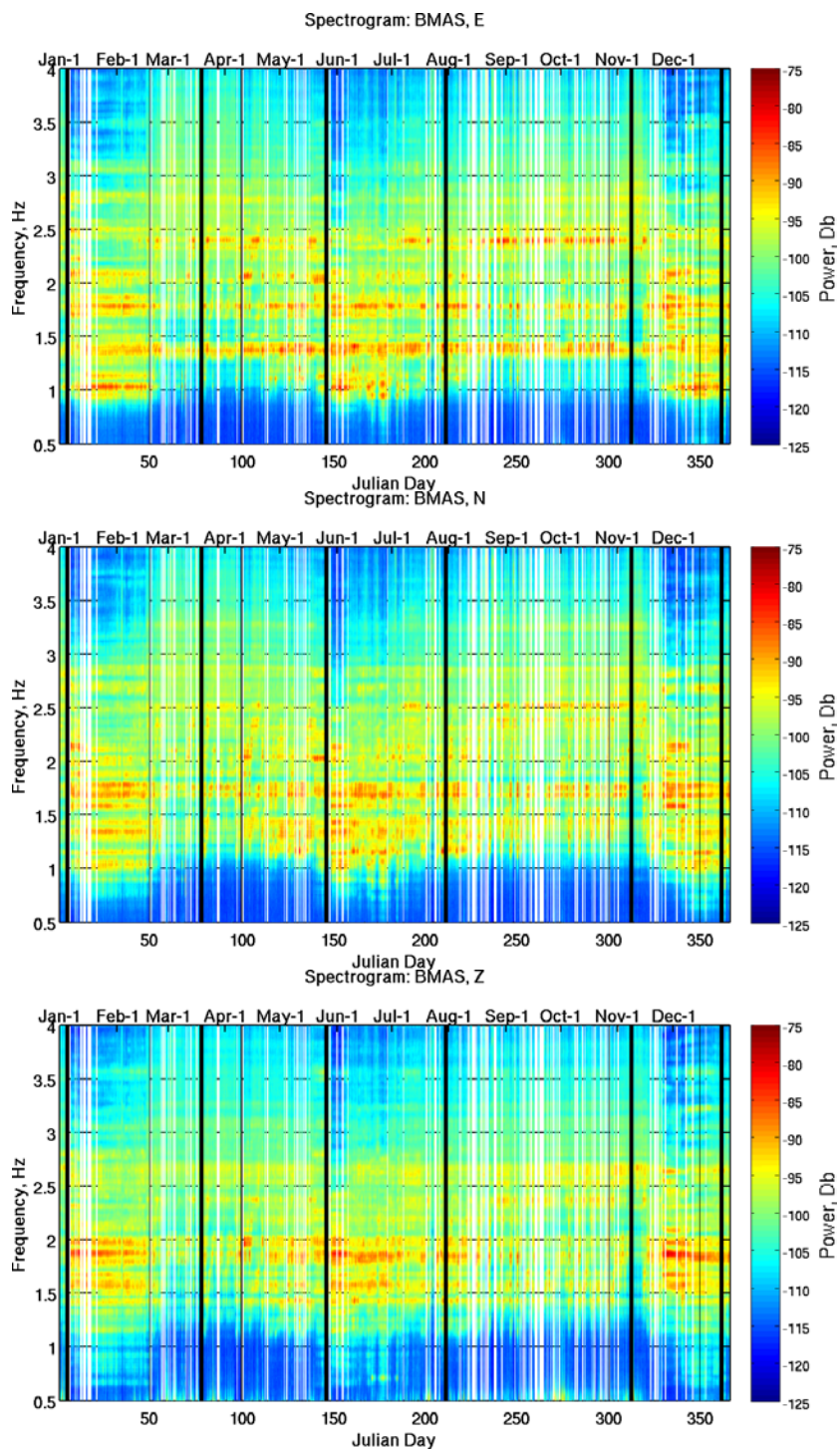


Figure 37. Spectrogram for BMAS, calculated from each 6-hour ambient noise record for the two horizontal components, East-West (E, top panel), North-South (N, middle panel), and vertical (Z, bottom panel) component at Tungurahua Volcano in 2010. The horizontal axis indicates the day in 2010, the vertical axis the frequency, and the colors represent the smooth amplitudes of the power spectra in decibels (Db).

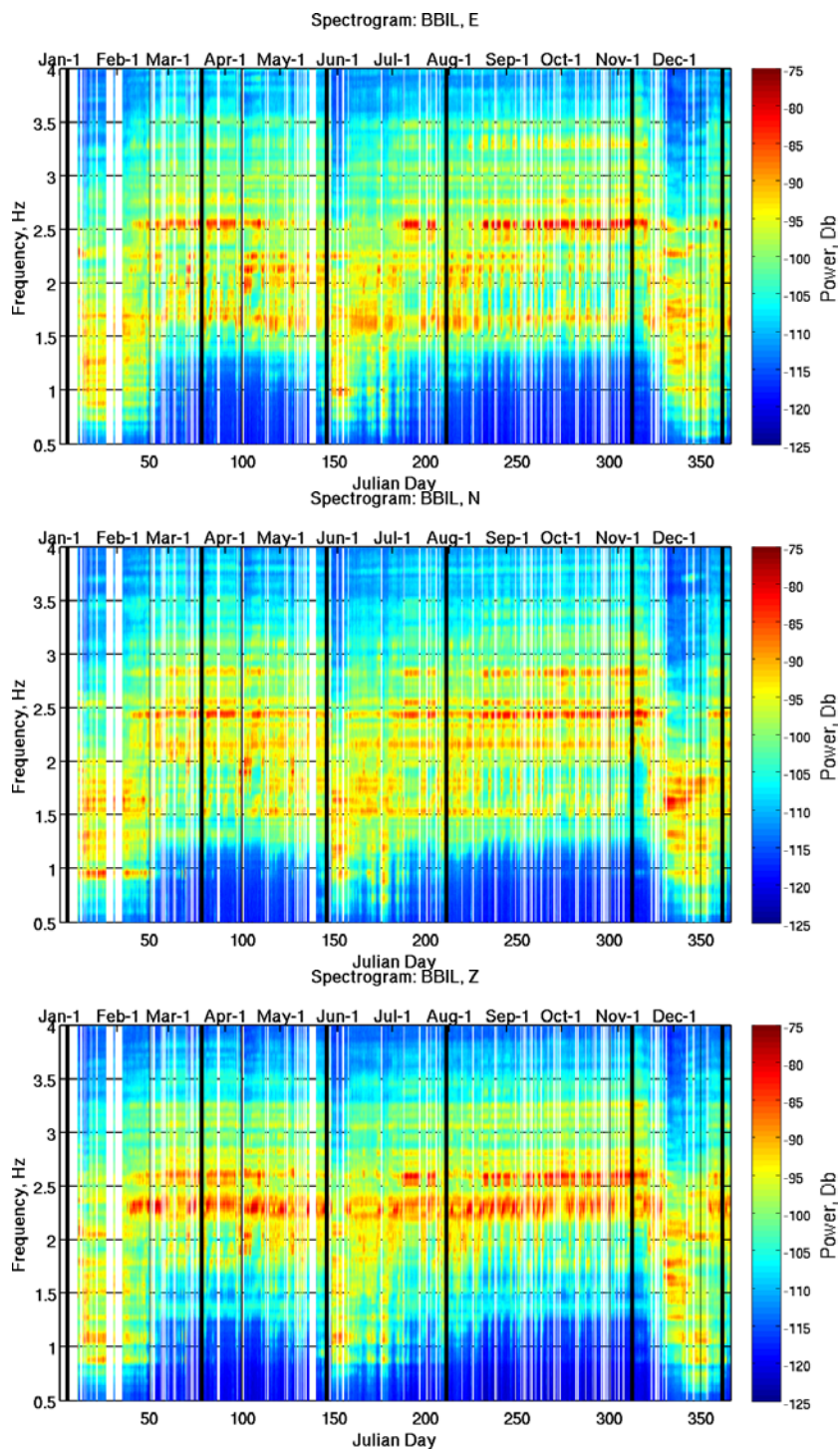


Figure 38 Spectrogram for BBIL, calculated from each 6-hour ambient noise record for the two horizontal components, East-West (E, top panel), North-South (N, middle panel), and vertical (Z, bottom panel) component at Tungurahua Volcano in 2010. The horizontal axis indicates the day in 2010, the vertical axis the frequency, and the colors represent the smooth amplitudes of the power spectra in decibels (Db).

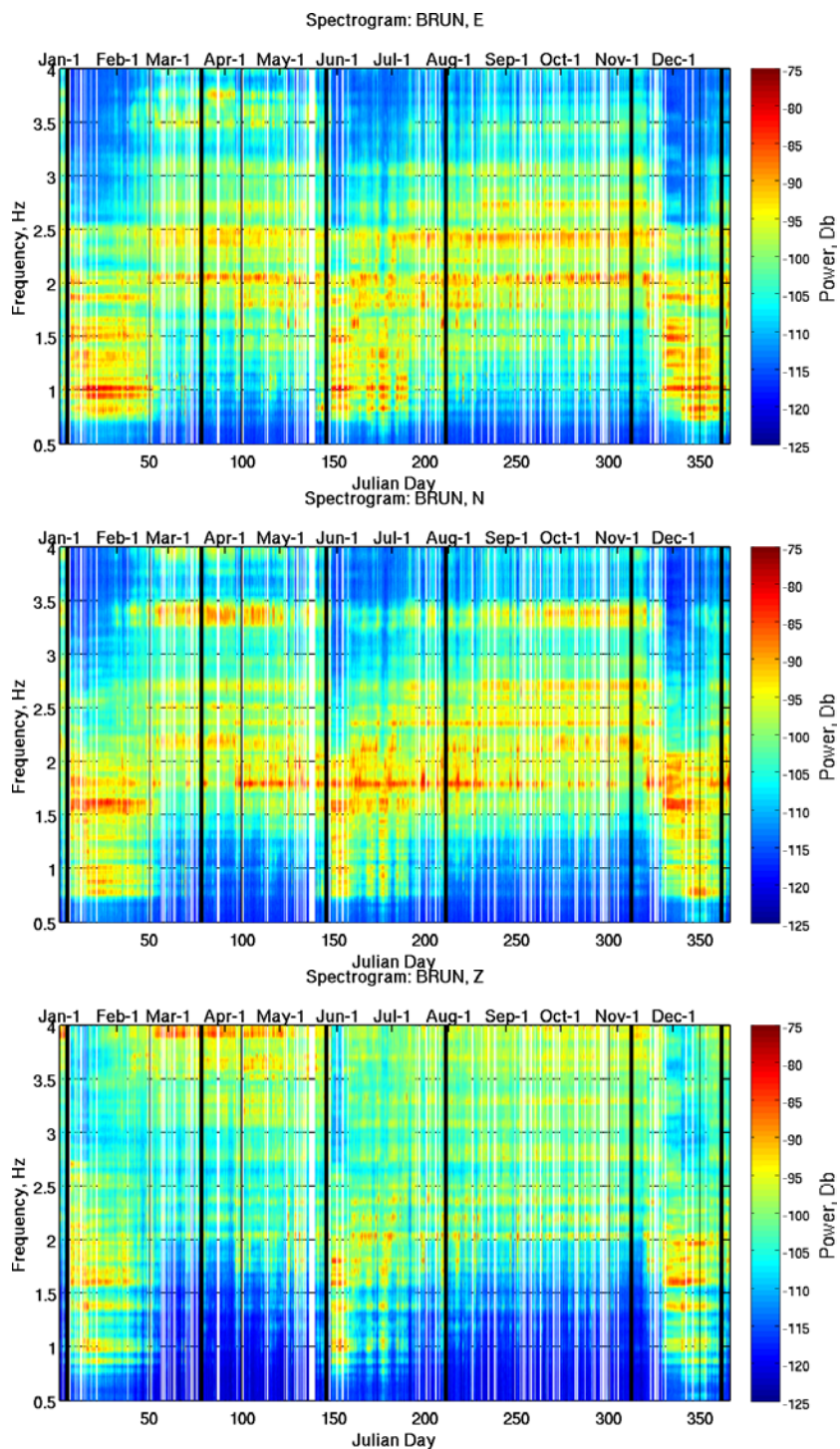


Figure 39. Spectrogram for BRUN, calculated from each 6-hour ambient noise record for the two horizontal components, East-West (E, top panel), North-South (N, middle panel), and vertical (Z, bottom panel) component at Tungurahua Volcano in 2010. The horizontal axis indicates the day in 2010, the vertical axis the frequency, and the colors represent the smooth amplitudes of the power spectra in decibels (Db).

9.3. Frequency dependent H/V ratio and temporally varying peak H/V ratio

From the horizontal and vertical component power spectra, calculated from each 6-hour record of ambient noise, the frequency dependent horizontal-to-vertical (H/V) kinetic energy ratio is calculated at each of the 5 stations in this study (see Figure 43-Figure 44, bottom panel). The peak H/V ratio is then calculated for each of the three frequency bands, wide-band (0.5-4 Hz), low frequency (0.5-2 Hz) and high frequency (2-4 Hz), and plotted (see Figure 43-Figure 44, top panel, and Figure 45-Figure 47). The parts of the H/V curve that are flat (stable) indicate times when the ambient noise field is in equilibrium for a particular band, a requirement of equipartition, while rapidly fluctuating parts of the H/V curve indicate that the wavefield is not in equilibrium and the condition of equipartition has not been achieved. Figure 45-Figure 47 show the peak H/V curves at each station and the spatially averaged H/V ratio calculated in the wide (0.5-4 Hz), low frequency (0.5-2 Hz) and high frequency (2-4 Hz) bands. In general, the peak H/V curves at stations BULB, BPAT, and BMAS are the most stable and flat in the high frequency (2-4 Hz) band, while fluctuating rapidly in the low frequency (0.5-2 Hz) and wide (0.5-4 Hz) bands. This is opposite to the characteristics of the peak H/V curve measured at stations BBIL and BRUN, which shows the greatest stability in the low frequency (0.5-2 Hz) band.

9.4. Stations BMAS, BULB, BPAT (see Figure 40-Figure 42).

At station BMAS, located on pyroclastic flow deposits, the frequency dependent H/V plot has bands of positive amplitudes at 1.5, 2, and 2.6 Hz, and bands of negative amplitude at 1 and 1.4 Hz for the duration of 2010. The peak H/V curves for the high frequency band (2-4 Hz) are the most stable, indicating that the wavefield in that band is closest to equilibrium. During the active eruptive periods the peak H/V value is elevated, but does not vary rapidly.

The low frequency (0.5-2 Hz) and wide (0.5-4Hz) bands vary rapidly over 2010, with the greatest variability in H/V values occurring at the end of eruptive periods and during quiescent periods. Though, during the start of eruptive episodes 1 and 2 the H/V curve shows a greater stability than at other times, which corresponds to the onset of eruptive activity and the greatest seismic amplitudes. During the third active eruption episode the H/V curves, in all frequency bands, show an increase after November 26, which corresponds to the peak in eruptive activity.

At station BULB, located on the NE flank, the frequency dependent H/V plot has bands of positive amplitudes at 1, 1.3, 1.6, 2, and 2.5Hz, and a band of negative amplitude at 0.8 Hz for the duration of 2010. A double band of positive amplitude occurs during the eruptive episodes at 3.2 Hz and a negative band occurs at 3.7 Hz during the quiescent periods and during the second active eruptive episode. The peak H/V curves measured at BULB follow a similar pattern to the curves measured at BMAS. The high frequency (2-4 Hz) band H/V curve is the most stable, while showing elevated values during the most active time of the eruptive period. The low frequency (0.5-2 Hz) and wide (0.5-4Hz) bands vary rapidly over 2010, with the greatest variability in H/V values occurring at the end of eruptive periods and during quiescent periods. The H/V curve shows a greater stability at the start of eruptive episodes 1 and 2.

The frequency dependent H/V plot at BPAT, located to the east of BMAS, appears quite distinct from the plots at the other four stations. BPAT shows a broad band of positive amplitudes below 1.7 Hz with peaks centered at ~0.5-0.7 Hz and 1.3-1.5Hz. Lower positive amplitude fringes occur at 2.2 to 2.5 Hz, while a broad trough of negative amplitude is present from 3-4 Hz. Like BULB and BMAS, the low frequency (0.5-2 Hz) and wide (0.5-4Hz) peak H/V curves show the greatest variability and the high frequency (2-4 Hz) peak H/V curve shows the most stability with no elevated values during peak eruptive activity.

9.5. BBIL and BRUN (see Figure 43 and Figure 44)

The amplitude bands on the plot of frequency dependent H/V at station BBIL are similar to those at BMAS, but shifted to higher frequencies. BBIL and BMAS are both located on more recent volcanic deposits. The plot at BBIL shows bands of positive amplitude at 2.4, 2.6, and 3.2 Hz and a negative trough at 1.6 Hz, for the duration of 2010. During the active eruptive episodes there is also a double positive amplitude peak at ~1 Hz.

The frequency dependent H/V plot at BRUN, located next to a canyon with steep topographic relief, appears quite distinct from the plots at the other four stations. The spectrogram shows a large broad positive amplitude peak from 3.5-4 Hz for the duration of 2010, with lower positive amplitude fringes occurring from 1.7 to 3.5 Hz during the most active periods of the three eruptive episodes. A wide band of negative amplitude occurs below 3.2 Hz during the quiescent periods and below 1.7 Hz during the eruptive episodes. BRUN appears to have the strongest site effects, especially in the higher frequency band, which could perhaps be attributed to its location, adjacent to a steep canyon.

The pattern of peak H/V values seen at BMAS, BULB and BPAT is reversed at BBIL and BRUN. At BBIL and BRUN the most stable peak H/V value is measured in the low frequency (0.5-2Hz) band, while showing the greatest variability in the high frequency (2-4 Hz) and wide bands. The low frequency (0.5-2 Hz) peak H/V values are also elevated slightly during times of peak eruptive activity. The low frequency (0.5-2 Hz) part of the ambient wavefield is better equilibrated at BRUN and BBIL than at the stations on the topographically rougher, older flanks.

In the low frequencies H/V is stable at the stations on the young, collapse scarp, BRUN and BBIL and the stations on the older flanks are noisy, while at the high frequencies the

reverse is true, H/V is stable at the stations on the old topographically rough flanks of Tungurahua. Wavelength at low frequencies is larger than the size of the scatterer on the rough, older flanks. The time required to reach a diffusive regime and equipartitioning depends strongly on the ratio of the size of the scatterer (characteristic dimension) to the wavelength.

9.6. H/V Figures

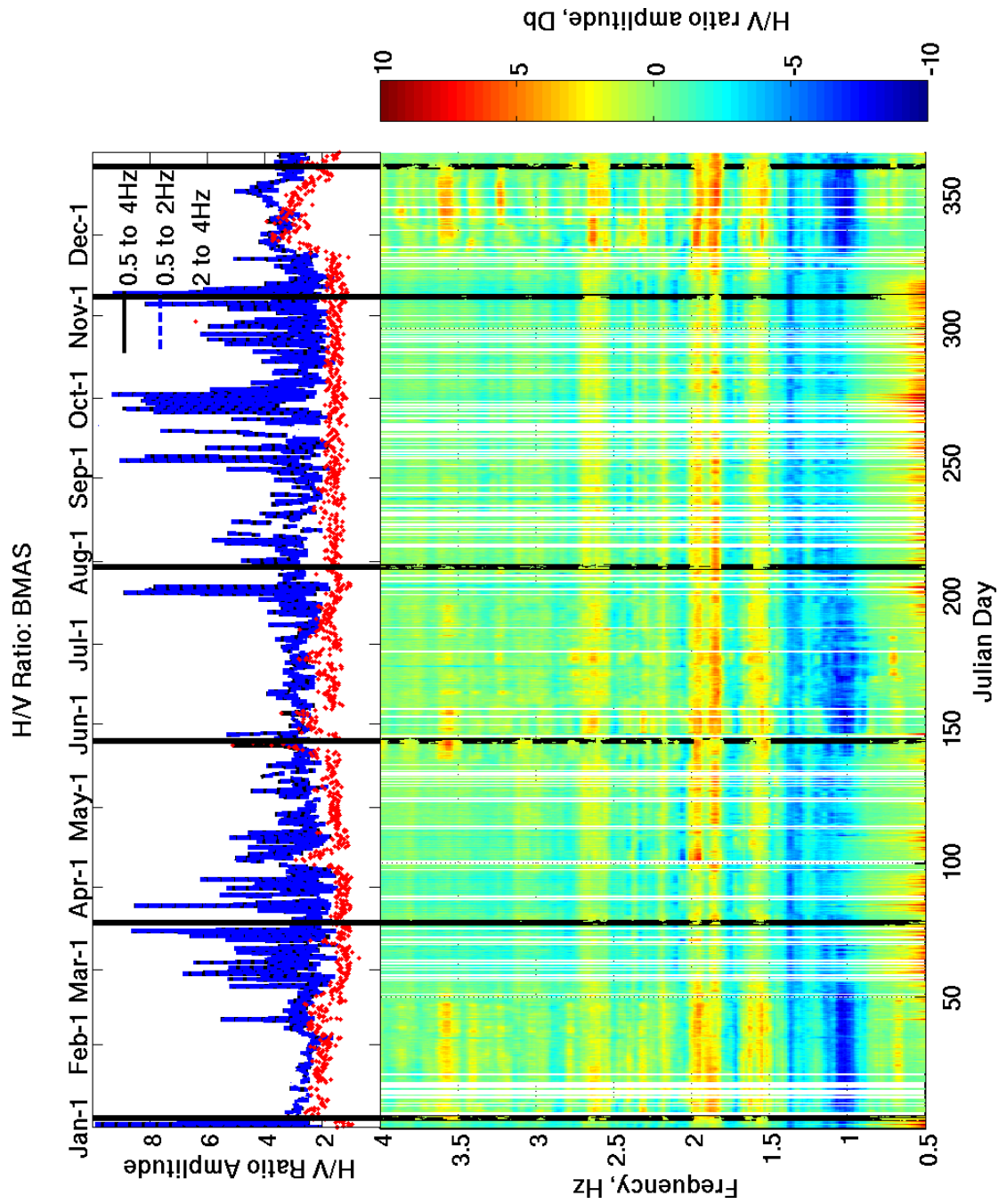


Figure 40. H/V at BMAS on Tungurahua Volcano, 2010. (Bottom panel) Frequency dependent H/V: The horizontal axis indicates the day in 2010, the vertical axis the frequency, and the colors represent the H/V amplitude values in decibels (Db). (Top panel) Peak H/V is shown for the wide (0.5-4 Hz) (black line), low frequency (0.5-2 Hz) (blue dashed line) and high frequency (2-4 Hz) (red dotted line) bands. The horizontal axis indicates the day in 2010 and the vertical axis the peak H/V value.

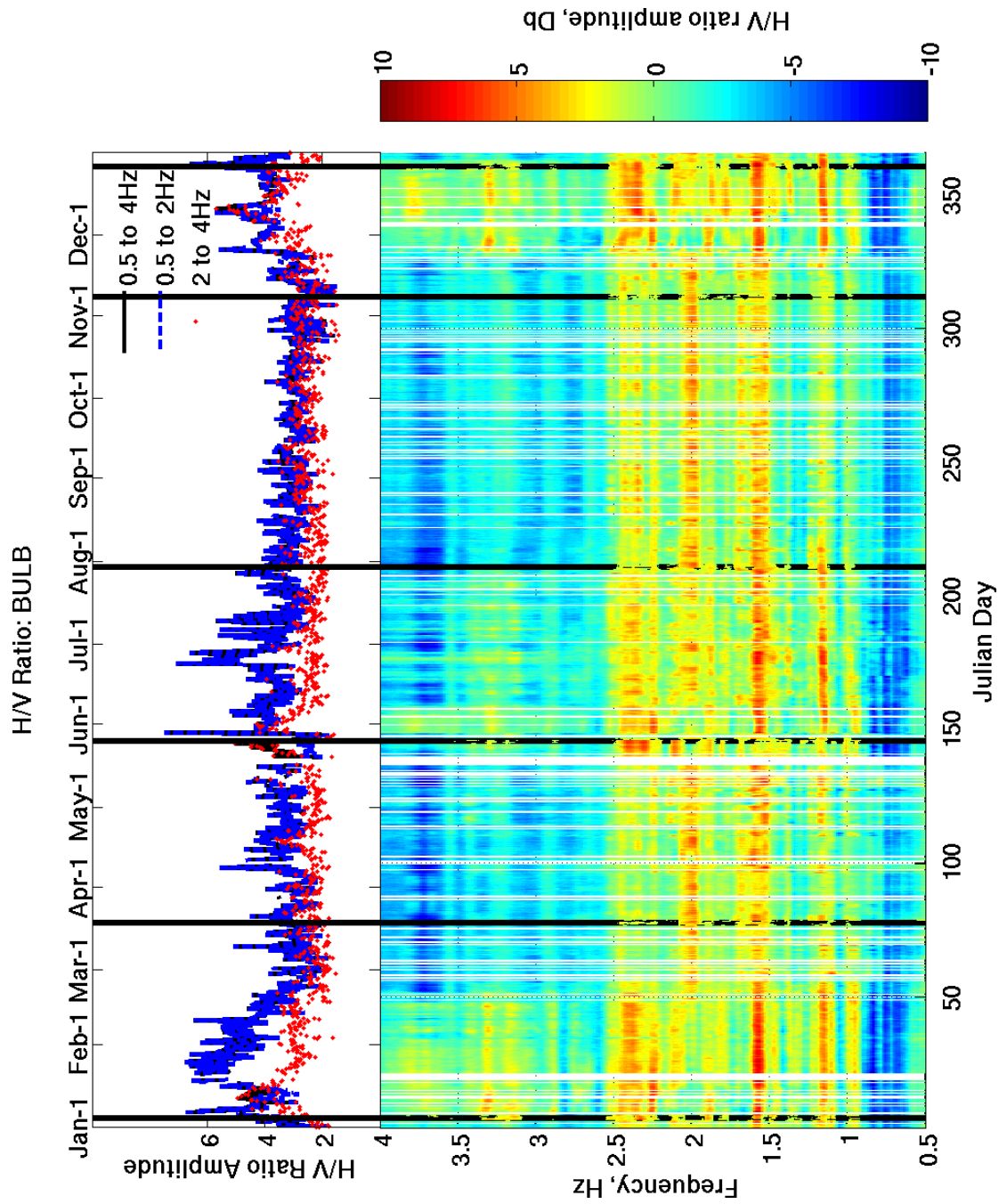


Figure 41. H/V at BULB on Tungurahua Volcano, 2010. (Bottom panel) Frequency dependent H/V: The horizontal axis indicates the day in 2010, the vertical axis the frequency, and the colors represent the H/V amplitude values in decibels (Db). (Top panel) Peak H/V is shown for the wide (0.5-4 Hz) (black line), low frequency (0.5-2 Hz) (blue dashed line) and high frequency (2-4 Hz) (red dotted line) bands. The horizontal axis indicates the day in 2010 and the vertical axis the peak H/V value.

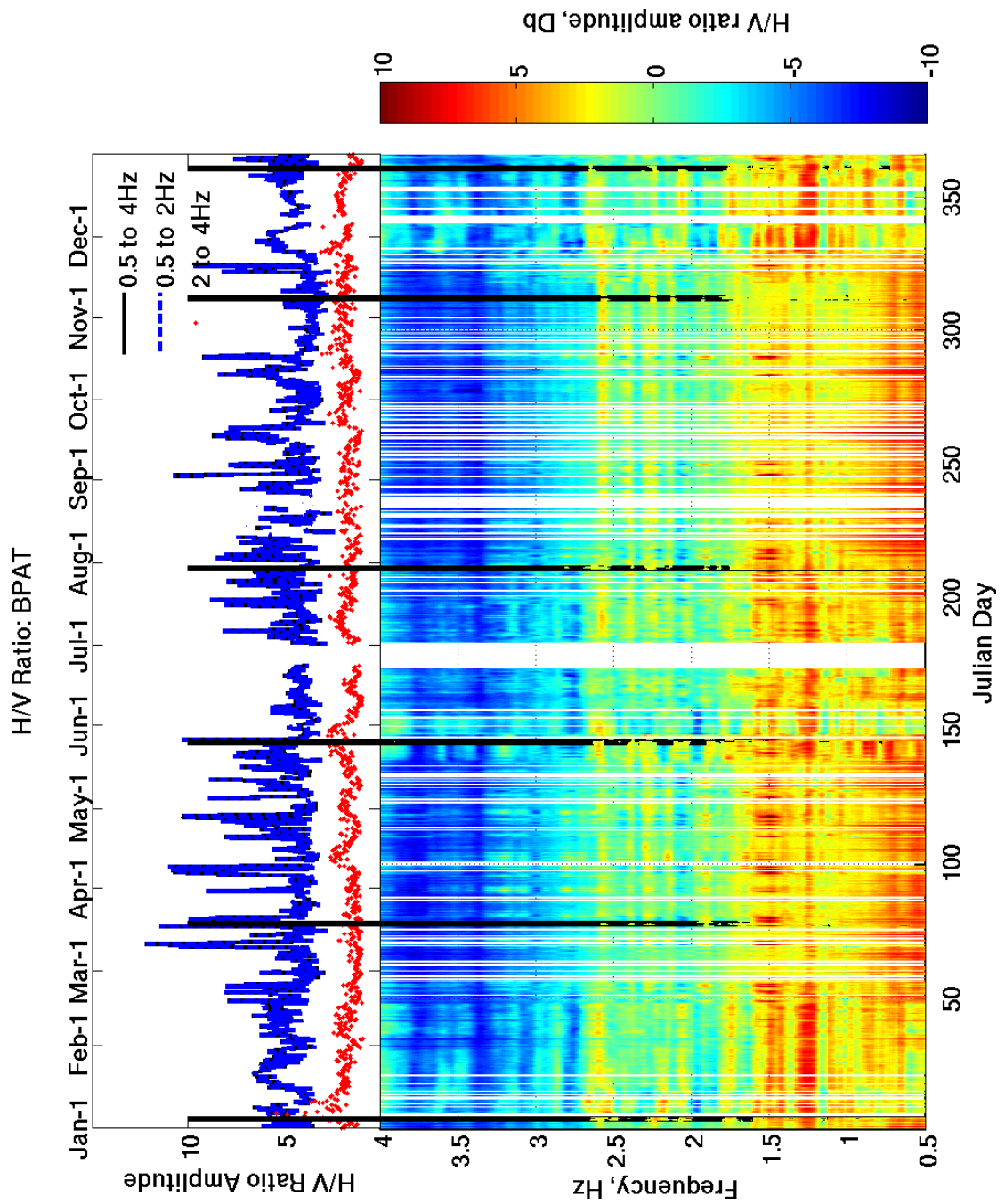


Figure 42. H/V at BPAT on Tungurahua Volcano, 2010. (Bottom panel) Frequency dependent H/V: The horizontal axis indicates the day in 2010, the vertical axis the frequency, and the colors represent the H/V amplitude values in decibels (Db). (Top panel) Peak H/V is shown for the wide (0.5-4 Hz) (black line), low frequency (0.5-2 Hz) (blue dashed line) and high frequency (2-4 Hz) (red dotted line) bands. The horizontal axis indicates the day in 2010 and the vertical axis the peak H/V value.

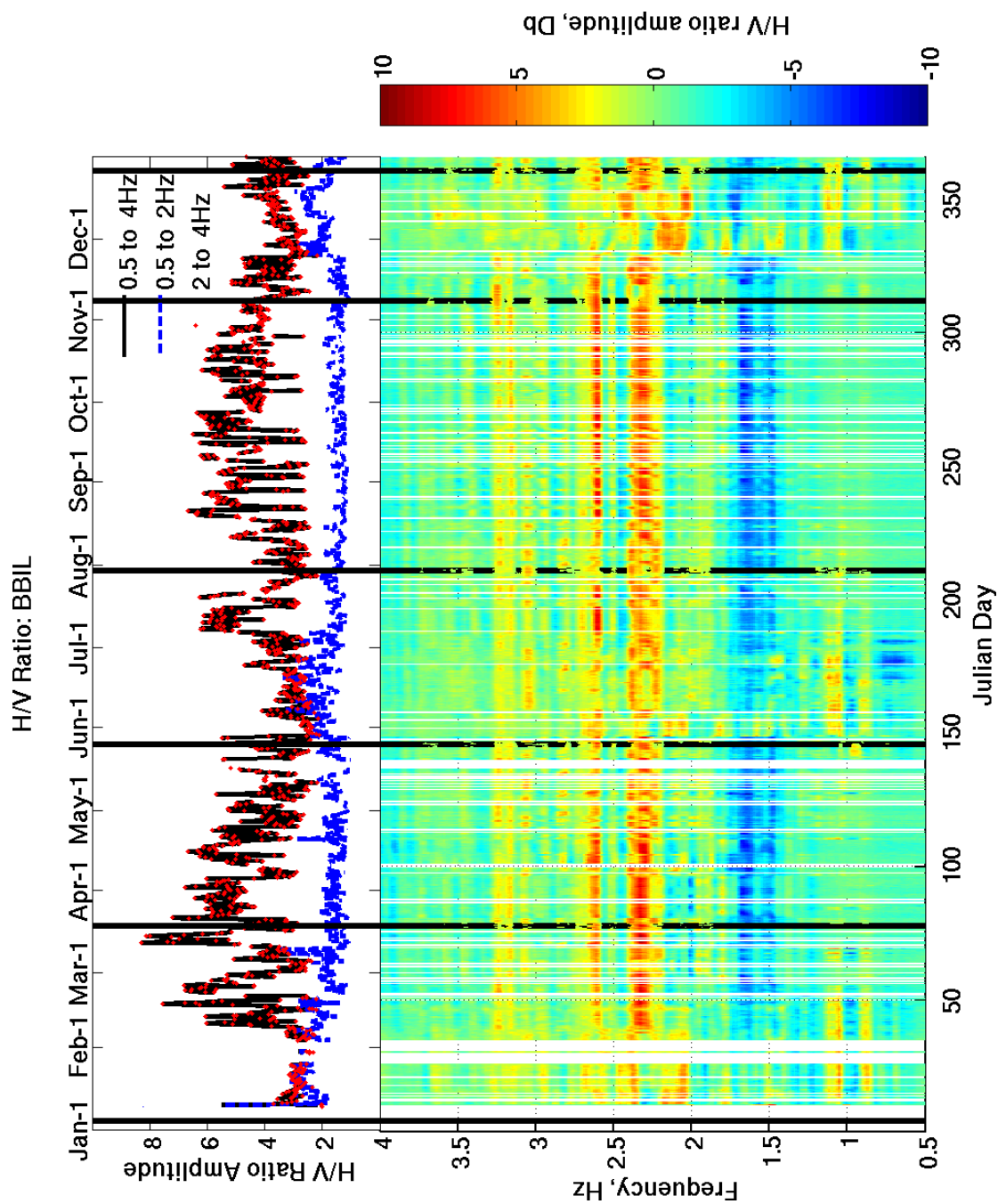


Figure 43. H/V at BBIL on Tungurahua Volcano, 2010. (Bottom panel) Frequency dependent H/V: The horizontal axis indicates the day in 2010, the vertical axis the frequency, and the colors represent the H/V amplitude values in decibels (Db). (Top panel) Peak H/V is shown for the wide (0.5-4 Hz) (black line), low frequency (0.5-2 Hz) (blue dashed line) and high frequency (2-4 Hz) (red dotted line) bands. The horizontal axis indicates the day in 2010 and the vertical axis the peak H/V value.

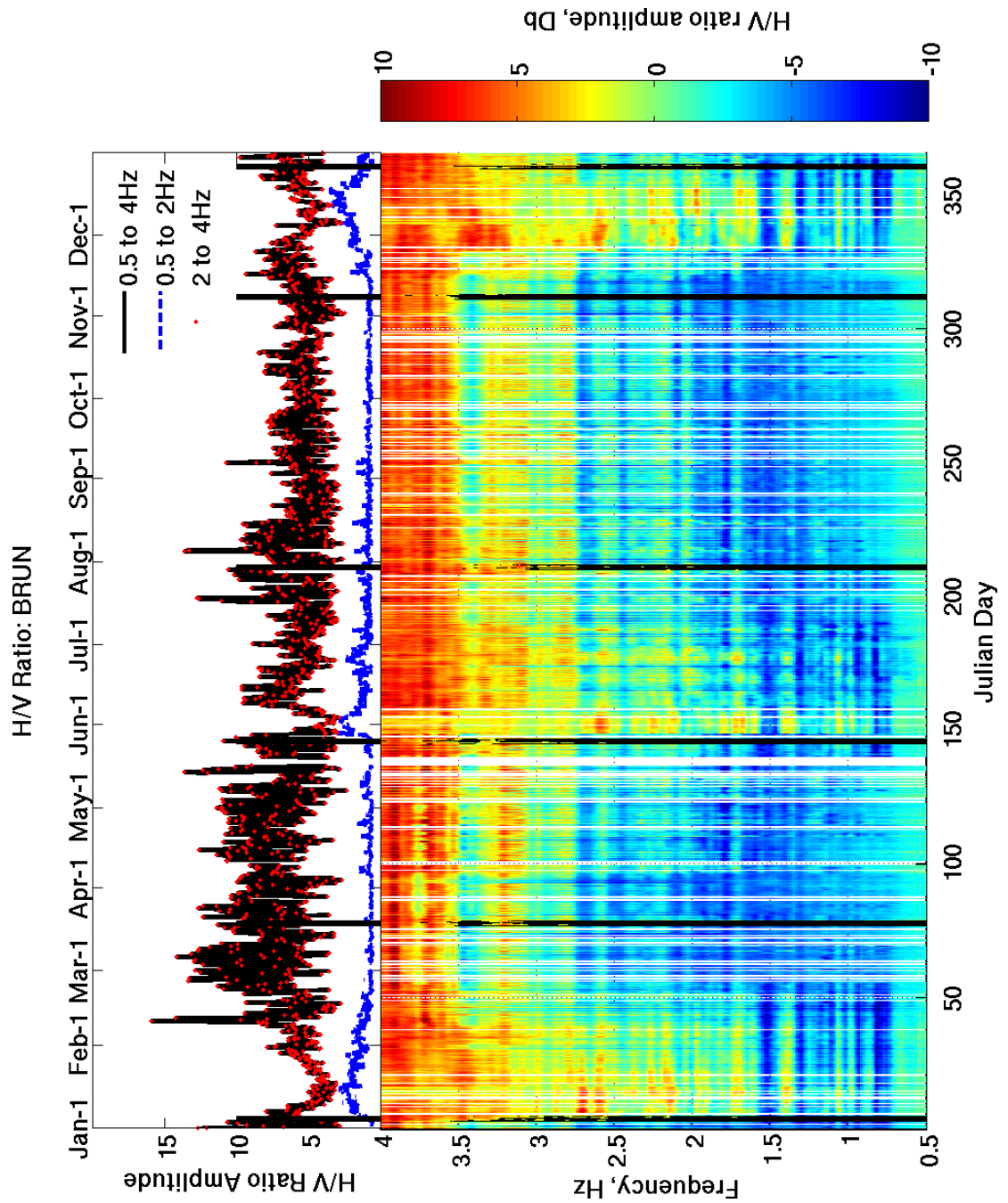


Figure 44. H/V at BRUN on Tungurahua Volcano, 2010. (Bottom panel) Frequency dependent H/V: The horizontal axis indicates the day in 2010, the vertical axis the frequency, and the colors represent the H/V amplitude values in decibels (Db). (Top panel) Peak H/V is shown for the wide (0.5-4 Hz) (black line), low frequency (0.5-2 Hz) (blue dashed line) and high frequency (2-4 Hz) (red dotted line) bands. The horizontal axis indicates the day in 2010 and the vertical axis the peak H/V value.

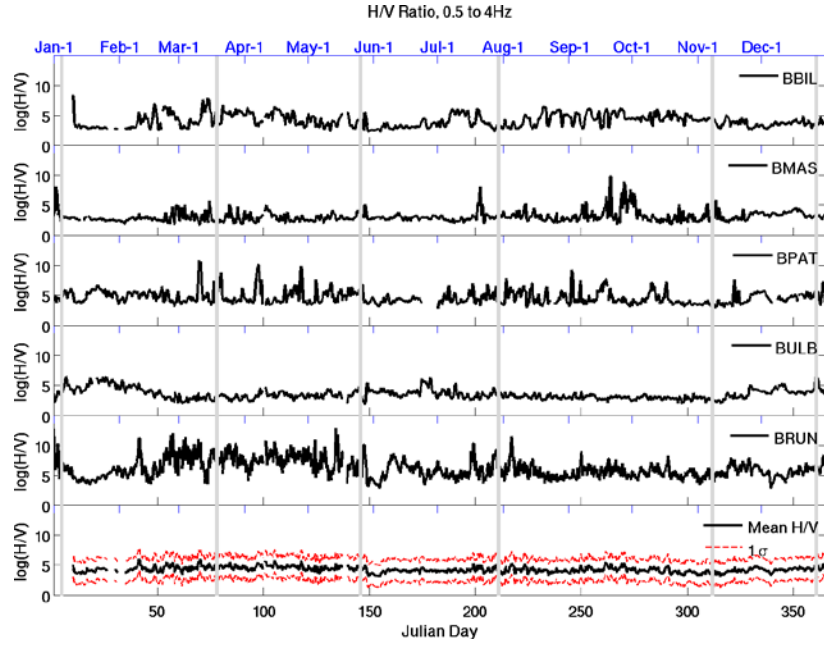


Figure 45. The wide band (0.5-4 Hz) peak H/V at each station located on Tungurahua Volcano, 2010. The bottom panel shows the mean peak H/V averaged over all the stations with 1σ error bar shown (red line). The horizontal axis indicates the day in 2010 and the vertical axis the peak H/V value.

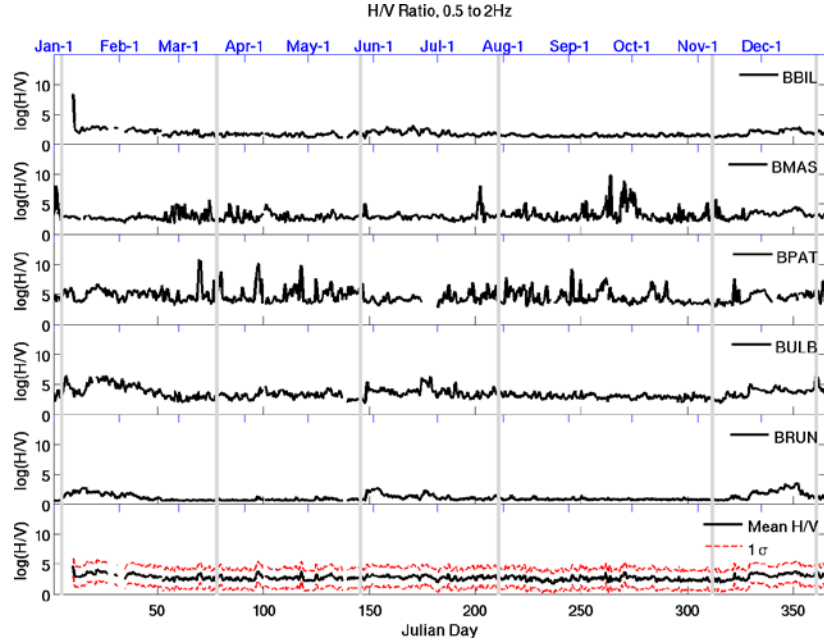


Figure 46. The low frequency band (0.5-2 Hz) peak H/V at each station located on Tungurahua Volcano, 2010. The bottom panel shows the mean peak H/V averaged over all the stations with 1σ error bar shown (red line). The horizontal axis indicates the day in 2010 and the vertical axis the peak H/V value.

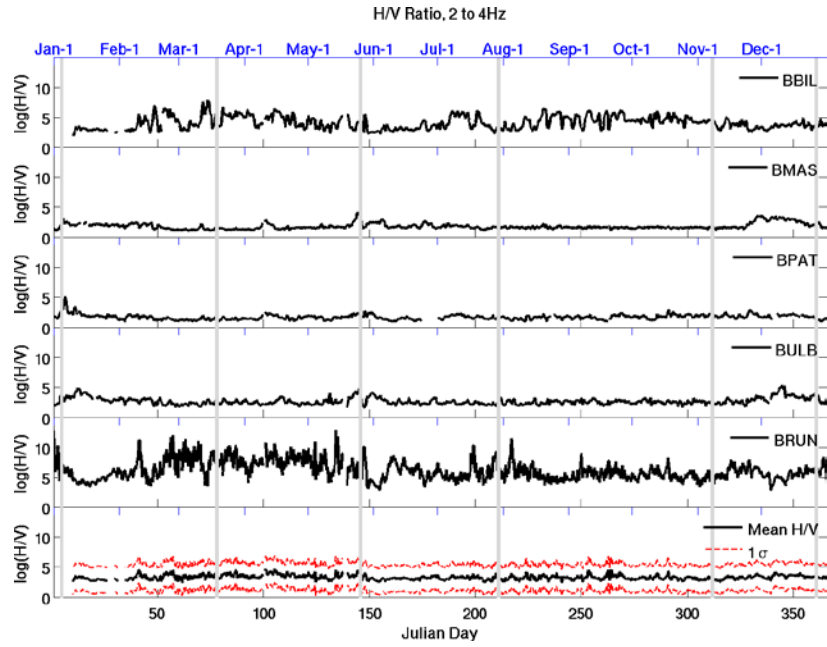


Figure 47. The high frequency band (2-4 Hz) peak H/V at each station located on Tungurahua Volcano, 2010. The bottom panel shows the mean peak H/V averaged over all the stations with 1σ error bar shown (red line). The horizontal axis indicates the day in 2010 and the vertical axis the peak H/V value.

Chapter 10

DISCUSSION AND CONCLUSIONS

10. Discussion

10.1. Spectral content of the ambient noise wavefield

During active eruptive episodes, the peak spectral content of the ambient noise field at Tungurahua shifts to lower frequencies, below ~2.5 Hz. This shifted band corresponds to the dominant frequency band of long period (LP) events recorded at Tungurahua (K. Kim, pers. comm., 2013). During quiescent periods with decreased volcanic activity, the power spectra have weaker peak amplitudes, with the exception of the spectra at BBIL, and are shifted to higher frequencies. The difference in peak spectral content reflects the changes in the source of the ambient noise field at Tungurahua. During active erupting episodes the wavefield is dominated by seismic sources generated by the eruptive activity, which also results in the stronger amplitude coherent arrivals that characterize the correlation functions of the eruptive episodes.

10.2. H/V and equipartition at Tungurahua

In general, the stability of the peak H/V curve depends on the location of the seismometer used (site effects) and on the frequency band in which the peak H/V ratio is measured. The peak H/V curves at stations BULB, BPAT, and BMAS are the most stable and flat in the high frequency (2-4 Hz) band, while fluctuating rapidly in the low frequency (0.5-2

Hz) and wide (0.5-4 Hz) bands. This is opposite to the characteristics of the peak H/V curve measured at stations BBIL and BRUN that shows the greatest stability in the low frequency (0.5-2 Hz) band.

The frequency dependence of the H/V stability may be due, in part, to the effect of topography. When incident wavelengths at a given frequency are comparable to the wavelength of the topography, scattering of the wavefield can increase and the partition of energies enhanced. This enhanced equilibration of the wavefield allows equipartition to be achieved more quickly in the frequency band in which scattering is enhanced. The stations where H/V is stable at higher frequencies (2-4 Hz), BULB, BPAT, and BMAS, are located on the older, topographically rougher flanks of Tungurahua, while the stations where H/V is stable at lower frequencies (0.5-2 Hz), BBIL and BRUN, are located on the younger, topographically smoother flanks. The rougher topography scatters the shorter wavelengths of the high frequency band (2-4 Hz) preferentially to the longer wavelengths of the low frequency band (0.5-2 Hz), and vice versa for the smoother topography. This results in a more rapid equilibration of the high frequency component of the wavefield at BPAT, BMAS, and BULB, while the low frequency component equilibrates more rapidly in the vicinity of BRUN and BBIL. The fact that BRUN is located next to a canyon does not appear to significantly affect the equilibration of the low frequency wavefield, although, it does enhance the variability and amplitude of the peak H/V ratio in the high frequency (2-4 Hz) and wide bands (0.5-4 Hz).

While the stability of the H/V ratio changes at different locations and frequency bands, the spatial average of the H/V ratio at all station locations is flat. This emphasizes the fact that averaging over multiple locations allows one to approximate equipartition conditions for a region, even while the characteristics of the ambient noise field at individual locations can vary

significantly from the average. It would be prudent to take into account the characteristics of the ambient noise field at individual locations in assessing the quality of correlation functions at each station (or station pair) and any measurements of elastic properties calculated from the correlation functions, i.e. phase or group velocity, dV/V , anisotropy, attenuation, etc.

The only temporal variations observed in the stability of the peak H/V curves at each of the stations is a slight increase in the amplitude of the peak H/V ratio during the active eruptive episodes. The increase of H/V during eruptions may be due to the additional seismic sources in the conduit system that contributes additional energy to the ambient noise wavefield during eruptions. Bonnefoy-Claudet *et al.* [2006] found that for a distribution of sources located near the receivers the value of the amplitude of the H/V ratio increased, while for sources located farther from the receivers the H/V ratio amplitude decreased.

10.3. H/V and site effects

Nakamura [1989] observed that the seismic waveforms recorded at the same site are similar even when the source and path are different. This indicates that surface conditions at the observation station, in addition to source and path effects, are critical factors in characterizing the vibration characteristics of the surficial layers. This information is important in estimating the intensity of shaking at a particular location for use in seismic hazard analysis. The transfer function for horizontal motion of the surface layers appears similar to the frequency dependent H/V ratio calculated from microtremor (ambient noise) [Nakamura, 1989]. The peak value of the H/V ratio gives an estimate of the peak site amplification factor and the frequency at which the peak H/V ratio is measured can be used to estimate of the dominant resonance of the surface layer [Nakamura, 1989; Konno and Ohmachi, 1998]. A value close to 1 for the peak H/V ratio is characteristic of hard rock and compact soils, while a

higher value is consistent with unconsolidated deposits [Nakamura 1989, Konno and Ohmachi, 1998]. The higher peak H/V values, >2.5 , at the five stations is consistent more unconsolidated materials that compose the bulk of the surficial deposits at Tungurahua, i.e., pyroclastic flow, tephra and volcanic breccias.

Bonnefoy-Claudet *et al.* [2006] found that for a distribution of sources located near the receivers the value of the amplitude of the H/V ratio increased while for sources located farther from the receivers the H/V ratio amplitude decreased. A near source will also increase the amplitude of the power spectra at the higher frequencies (>2 Hz) especially on the vertical component [Nakamura, 1989]. The vertical component of BRUN, located next to a canyon, shows a dramatic increase in amplitude of the power spectra at the high frequencies. The canyon is as strong scatterer and acts as a secondary, near source, amplifying the signal. This is consistent with previous work that showed the edge of a canyon acts to amplify wave displacement, especially on the vertical component and this amplification is frequency dependent [Bouchon *et al.*, 1996; Tadeu *et al.*, 2001].

The distribution of sources also affects the shape of the frequency dependent H/V. Far sources, located within the surface sedimentary layers or bedrock, will produce a double peaked H/V curve with the first peak at the frequency of the fundamental mode Rayleigh wave and the second due to resonating head S-waves. A near source located within the surface layers produces a single peak. [Bonnefoy-Claudet *et al.*, 2006] The multiple peaks on the H/V figures calculated at Tungurahua indicate that the site geometry is more complicated than a simple two layer model used by Bonnefoy-Claudet *et al.* [2006], which exhibit at most two peaks in the H/V curve. This may also imply that there are multiple types of sources, near and far, that contribute to the ambient noise wavefield at Tungurahua.

10.4. Conclusions

The spectra and equipartition of the ambient noise wavefield exhibits striking changes due to source and site effects at Tungurahua. The background ambient noise field spectrum is characterized by low amplitudes that peak in a range from ~ 1 -3.7 Hz. During the active eruptive episodes the peak amplitudes increase and shift to below ~ 2.5 Hz. The low frequency band corresponds to the dominant frequency band of the long-period (LP) earthquakes that are generated during eruptions at Tungurahua.

The difference in peak spectral content reflects the changes in the source of the ambient noise field at Tungurahua. During active erupting episodes the wavefield appears to be dominated by seismic sources generated by the eruptive activity, which results in the stronger amplitude coherent arrivals that characterize the correlation functions of the eruptive episodes. The slight increase in the amplitude of the stable, peak H/V curves at each station during the active eruptive periods indicates the dominant source has changed from a diffuse and/or far field source to a near source, e.g. earthquakes generated by changes in the erupting conduit system. Distributions of sources located near to receivers increases the amplitude of the H/V ratio [Bonnefoy-Claudet *et al.*, 2006]. The changes in dV/V measured during the eruptive periods in the previous work may be due to source changes, possibly generated by the conduit system. This hypothesis is consistent with the conclusions of Haney *et al.* [2009] that changes in the relative velocity at Pavlof Volcano result from a change in the geometry and properties of the conduit system. Further work is needed to identify the location of the sources.

In addition to the source effects, site conditions and topography also appear to strongly influence the equipartition of the wavefield. At stations located on the older, topographically rougher flanks of Tungurahua the peak H/V is most stable at higher frequencies (2-4 Hz), while

at the stations located on the younger, topographically smoother flanks, the peak H/V is most stable at lower frequencies (0.5-2 Hz). The rougher topography scatters the shorter wavelengths of the high frequency band (2-4 Hz) preferentially to the longer wavelengths of the low frequency band (0.5-2 Hz), and vice versa for the smoother topography, resulting in a more rapid equilibration of the wavefield that is preferentially scattered.

The vertical component of BRUN, located next to a deep canyon, shows a dramatic increase in amplitude of the power spectra at the high frequencies. The canyon is as strong scatterer and acts as a secondary, near source, amplifying the signal. This is consistent with previous work that showed the edge of a canyon acts to amplify wave displacement, especially on the vertical component and this amplification is frequency dependent [Bouchon *et al.*, 1996; Tadeu *et al.*, 2001]. In spite of the effect that the canyon has on vertical component power spectra it does not appear to significantly affect the equilibration of the low frequency wavefield, although, it does enhance the variability and amplitude of the peak H/V ratio in the high frequency (2-4 Hz) and wide bands (0.5-4 Hz).

Although, the stability of the H/V ratio, and level of local equipartition, changes at different locations and for different frequency bands, the spatial average of the H/V ratio at all station locations stable. While this allows one to calculate relative velocity change for the entire region, one must take into account the effects of source and topography to be able to accurately determine relative velocity changes at individual stations or for shorter correlation times used to continuously monitor a volcano.

BIBLIOGRAPHY

- Atwater, T. (1970), Implications of plate tectonics for the Cenozoic evolution of western North America, *Geol. Soc. Amer. Bull.*, 81, 3513-3536.
- Atwater, T., and J. Stock (1998), Pacific-North America plate tectonics of the Neogene southwestern United States - an update, in *International Geological Review*, Clarence Hall Symposium volume, edited by W. G. Ernst, pp. 375-402.
- Bacon, C., P. E. Bruggman, R. Christiansen, M. A. Clynne, J. D. Donnelly-Nolan, and W. Hildreth (1997), Primitive Magmas at Five Cascade Volcanic Fields: Melts from Hot, Heterogeneous Sub-Arc Mantle, *The Canadian Mineralogist*, 35, 397-423.
- Barmin, M.P., M.H. Ritzwoller, and A.L. Levshin, (2001), A fast and reliable method for surface wave tomography, *Pure Appl. Geophys.*, 158(8), 1351 - 1375.
- Battaglia, J., J.-P. Métaxian, and E. Garaebiti, (2012), Earthquake-volcano interaction imaged by coda wave interferometry, *Geophys. Res. Lett.*, 39, L11309, doi: 10.1029/2012GL052003.
- Bensen, G.D., M.H. Ritzwoller, M.P. Barmin, A.L. Levshin, F. Lin, M.P. Moschetti, N.M. Shapiro, and Y. Yang (2007), Processing seismic ambient noise data to obtain reliable broad-band surface wave dispersion measurements, *Geophys. J. Int.*, 169, 1239-1260, doi: 10.1111/j.1365-246X.2007.03374.x.
- Bensen, G.D., M.H. Ritzwoller, and N.M. Shapiro (2008), Broad-band ambient noise surface wave tomography across the United States, *J. Geophys. Res.*, 113, B05306, doi: 10.1029/2007JB005248.
- Bleistein, N., (1984). Mathematical Methods for Wave Phenomena, *Academic Press*, Orlando.
- Bonnefoy-Claudet, S., C. Cornou, P-Y Bard, F. Cotton, P. Moczo, J. Kristek, D. Fäh (2006), H/V ratio *Geophys. J. Int.*,: a tool for site effects evaluation. Results from 1-D noise simulations, vol. 167, pp 827-837, doi: 10.1111/j.1365-246X.2006.03154.x.
- Bouchon, M., C. A. Schultz, and M. N. Toksöz (1996), Effect of three-dimensional topography on seismic motion, *J. Geophys. Res.*, 101(B3), pp. 5835–5846, doi:10.1029/95JB02629.
- Braile, L.W., R.B. Smith, J. Ansorge, M.R. Baker, M.A. Sparlin, C. Prodehl, M.M. Schilly, J.H. Healy, St. Mueller, and K.H. Olsen (1982). The Yellowstone-Snake River Plain Seismic Profiling Experiment: Crustal Structure of the Eastern Snake River Plain. *J. Geophys. Res.*, 87, 2597-2609
- Brenguier, F., D. Clarke, Y. Aoki, N.M. Shapiro, M. Campillo, V. Ferrazzini, (2011), Monitoring volcanoes using seismic noise correlations, *C. R. Geoscience*, 343, pp. 633-638, doi: 10.1016/j.crte.2010.12.010.

- Brenguier, F., M. Campillo, C. Hadziioannou, N. M. Shapiro, R. M. Nadeau, and E. Larose (2008a), Postseismic relaxation along the San Andreas Fault at Parkfield from continuous seismological observations, *Science*, *321* (5895), 1478-1481. doi:10.1126/science.1160943.
- Brenguier, F., N. M. Shapiro, M. Campillo, V. Ferrazzini, Z. Duputel, O. Coutant, A. Nercessian (2008b), Towards forecasting volcanic eruptions using seismic noise, *Nature Geoscience*, *1*(2), pp. 126-130, doi:10.1038/ngeo104.
- Brenguier, F., N. M. Shapiro, M. Campillo, A. Nercessian, and V. Ferrazzini (2007), 3-D surface wave tomography of the Piton de la Fournaise volcano using seismic noise correlations, *Geophys. Res. Lett.*, *34*, L02305, doi:10.1029/2006GL028586.
- Brueseke, M.E., Hart, W.K., Heizler, M.T., (2008). Diverse mid-Miocene silicic volcanism associated with the Yellowstone-Newberry thermal anomaly. *Bull Volcanol.* *70*, 343-360.
- Camp, V.E. and M.E. Ross (2004), Mantle dynamics and genesis of mafic magmatism in the intermontane Pacific Northwest. *J. Geophys. Res.* *109*, B08204. Doi:10.1029/2003JB002838.
- Carlson, R.L. and W.K. Hart (1987), Crustal genesis of the Oregon plateau. *J. Geophys. Res.* *92*, 6191-6207.
- Chaput, J. A., D. Zandomenighi, R. C. Aster, H. Knox, and P. R. Kyle (2012), Imaging of Erebus volcano using body wave seismic interferometry of Strombolian eruption coda, *Geophys. Res. Lett.*, *39*, L07304, doi:10.1029/2012GL050956.
- Christiansen, R.L., G.R. Foulger, and J.R. Evans (2002), Upper-mantle origin of the Yellowstone hotspot. *Geol. Soc. Am. Bull.*, *114*, 1245-1256.
- Christiansen, R.L. and E.H. McKee (1978), Late Cenozoic volcanic and tectonic evolution of the Great Basin and Columbia Intermontane regions, in *Geol. Soc. Amer. Memoir.*, edited by R.B. Smith, and G.P. Eaton, 283-311.
- Conrey, R.M., D.R. Sherrod, P.R. Hooper, and D.A. Swanson (1997), Diverse, primitive magmas in the Cascade arc, northeast Oregon and southern Washington, *Canadian Mineralogist* *35*, 367-396, 1997.
- Cross, T.A. and R. H. Pilger (1982), Controls on subduction geometry, location of magmatic arcs, and tectonic arc and back-arc regions. *Geol. Soc. Am. Bull.* *93*, 545-562.
- Crotwell, H.P., Owens, T.J., 2005, Automated Receiver Function Processing, *Seismo. Res. Lett.*: Electronic Seismologist November/December, 2005.
- Crowell, J.C. (1968) Movement histories of faults in the Transverse ranges and speculations on the tectonic history of California in Dickinson, W.R., and Grantz, A., Editors, *Proceedings of the conference on geologic problems of San Andreas fault system: Stanford Univ. Pubs., Geol. Sci.* v. 11, p. 323-341.

- DeNosaquo, K.R., R.B. Smith, and A.R. Lowry (2009), Density and lithospheric strength models of the Yellowstone-Snake River Plain volcanic system from gravity and heat flow data. *J. Volcanol. Geotherm. Res.* 188, 108-127.
- Draganov, D., X. Campman, J. Thorbecke, A. Verdel, and K. Wapenaar (2009), Reflection images from ambient seismic noise, *Geophysics*, 74(5), pp. A63-A67, doi: 10.1190/1.3193529.
- Draper, D.S. (1991), Late Cenozoic bimodal magmatism in the northern Basin and Range Province of southeastern Oregon, *J. Volcanol. Geotherm. Res.*, 47: 299-328.
- Duputel, Z., V. Ferrazzini, F. Brenguier, N.M. Shapiro, M. Campillo, A. Nercessian, (2009), Real time monitoring of relative velocity changes using ambient seismic noise at the Piton de la Fournaise volcano (La Réunion) from January 2006 to June 2007, *J. Volcanol. Geotherm. Res.*, 184, pp.164-173, doi: 10.1016/j.jvolgeores.2008.11.024.
- Eagar, K.C., Fouch, M.J., James, D.E., Carlson, R.L., Group, H.L.P.S.W., 2011, Crustal structure beneath the High Lava Plains of eastern Oregon and surrounding regions from receiver function analysis, *J. Geophys. Res.*, 116, B02313, doi:10.1029/2010JB007795.
- Gao, H., E. D. Humphreys, H. Yao, and R. D. van der Hilst, (2011), Crustal and lithosphere structure of the Pacific Northwest with ambient noise tomography, *Earth Planet. Space. L.* 304, 202-211.
- Geist, D., and M. Richards (1993). Origin of the Columbia Plateau and Snake River plain: Deflection of the Yellowstone plume. *Geology* 21, 789-792.
- Greeley, R. (1982), The Snake River Plain, Idaho: Representative of a new category of volcanism: *J. Geophys. Res.*, v.87, p. 2705-2712.
- Fäh, D., F. Kind, D. Giardini (2001), A theoretical investigation of average H/V ratio, *Geophys. J. Int.*, vol. 145, pp. 535-549,
- Hadziioannou, C., E. Larose, A. Baig, P. Roux, and M. Campillo, (2011), Improving temporal resolution in ambient noise monitoring of seismic wave speed, *J. Geophys. Res.*, 116, B07304, doi: 10.1029/2011JB008200.
- Hadziioannou, C., E. Larose, O. Coutant, P. Roux, and M. Campillo, (2009), Stability of monitoring weak changes in multiply scattering media with ambient noise correlation: Laboratory experiments, *J. Acoust. Soc. Am.*, 125(6), pp. 3688-3695, doi:10.1121/1.3125345.
- Hales, T. C., D. L. Abt, E. D. Humphreys, and J. J. Roering (2005), A lithospheric instability origin for Columbia River flood basalts and Wallowa Mountains uplift in northeast Oregon, *Nature*, 438, 842-845.

- Hall, M.L., P. Samaniego, J.L. Le Pennec, J.B. Johnson, (2008), Ecuadorian Andes volcanism: A review of Late Pliocene to present activity, *J. Volcanol. Geotherm. Res.*, 176, 1-6, doi: 10.1016/j.jvolgeores.2008.06.012.
- Hall, M.L., C. Robin, B. Beate, P. Mothes, M. Monzier, (1999), Tungurahua Volcano, Ecuador: structure, eruptive history and hazards, *J. Volcanol. Geotherm. Res.*, 91, 1-21.
- Haney, M. M., K. van Wijk, L. A. Preston, and D. F. Aldridge (2009), Observation and modeling of source effects in coda wave interferometry at Pavlof volcano, *The Leading Edge* 28, pp. 554-560, doi:10.1190/1.3124930.
- Hart, W., J. Aronson, and S. Mertzman (1984), Areal Distribution and Age of Low-K, High-Alumina Olivine Tholeiite Magmatism in the Northwestern Great-Basin, *Geol. Soc. Amer. Bull.*, 95(2), 186-195.
- Hennino, R. N. Trégourès, N.M. Shapiro, L. Margerin, M. Campillo, B.A. van Tiggelen, and R.L. Weaver, (2001). Observation of equipartition of seismic waves, *Phys. Rev. Lett.*, vol. 86(15), pp. 3447-3450, doi: 10.1103/PhysRevLett.86.3447.
- Humphreys, E., Dueker, K., Schutt, D.L., Smith, R.B., (2000). Beneath Yellowstone: Evaluating plume and nonplume models using teleseismic images of the upper mantle. *GSA Today* 10, 1-7.
- IGEPN Resúmen Mensual, December 2009; January, February, March, June, July, October, November, December, 2010; January 2011, <http://www.igepn.edu.ec/index.php/volcan-tungurahua/informes.html>.
- James, D.E., M.J. Fouch, R.W. Carlson, and J.B. Roth, (2011), Slab fragmentation, edge flow and the origin of the Yellowstone hotspot track, *Earth Planet. Sci. Lett.*, doi: 10.1016/j.epsl.2011.09.007
- Jordan, B.T., A.L. Grunder, R.A. Duncan, and A.L. Deino (2004), Geochronology of age progressive volcanism of the Oregon High Lava Plains: implications for the plume interpretation of Yellowstone. *J. Geophys. Res.* 109, B10202. doi:10.1029/ 2003JB002776.
- Kawase, H., F. J. Sánchez-Sesma, S. Matsushima (2011), The optimal use of horizontal-to-vertical spectral ratios of earthquake motions for velocity inversions based on diffuse-field theory for plane waves, *Bull. Seism. Soc. Amer.*, vol. 101 (5), pp. 2001-2014, doi: 10.1785/0120100263.
- Kennett, B.L.N., 1991. IASPEI 1991 Seismological Tables. Bibliotech, Canberra, Australia.
- Konno, K., and T. Ohmachi (1998), Ground-motion characteristics estimated from spectral ratio between horizontal and vertical components of microtremor, *Bull. Seism. Soc. Amer.*, vol. 88 (1), pp. 228-241.
- Lawrence, J.F. and G. Prieto (2011), Attenuation Tomography of the Western United States from Ambient Seismic Noise, *J. Geophys. Res.* 116, B06302, doi:10.1029/ 2010JB007836.

- Lawrence, R. D. (1976), Strike-slip faulting terminates the Basin and Range province in Oregon, *Geol. Soc. Amer. Bull.*, 87, 846-850.
- Lees, Jonathan M, Keehoon Kim, Mario Calixto Ruiz, John J Lyons, Alexander Lincoln Steele, (2012). V31G-08: Energetic Explosions at Tungurahua Volcano, Ecuador, May/June 2010: VLP, LP and Tremor Signals presented at the American Geophysical Union, Fall Meeting, San Francisco, 2012
- Lees, J. M., Gordeev, E. I. and Ripepe, M. (2004), Explosions and periodic tremor at Karymsky volcano, Kamchatka, Russia. *Geophysical Journal International*, 158: 1151–1167. doi: 10.1111/j.1365-246X.2004.02239.x
- Lermo, J. and F.J. Chávez-García (1993), Site effect evaluation using spectral ratios with only one station, *Bull. Seism. Soc. Amer.*, vol. 83, pp. 1574-1594.
- Levshin, A.L., Yanovskaya, T.B., Lander, A.V., Bukchin, B.G., Barmin, M.P., Ratnikova, L.I. And Its, E.N., 1989. *Seismic Surface Waves in a Laterally Inhomogeneous Earth*, ed. Keilis-Borok, V.I. Kluwer, Norwell, Mass.
- Levshin, A.L. and Ritzwoller, M.H. 2001. Automated detection, extraction, and measurement of regional surface waves, *Pure appl. Geophys.*, 158(8), 1531-1545
- Lin, F., M.H. Ritzwoller, J. Townend, M. Savage, S. Bannister (2007), Ambient noise Rayleigh wave tomography of New Zealand, *Geophys. J. Int.*, 18 pages, doi:10.1111/j.1365-246X.2007.03414.x.
- Lin, F., M.P. Moschetti, and M.H. Ritzwoller (2008), Surface wave tomography of the western United States from ambient seismic noise: Rayleigh and Love wave phase velocity maps, *Geophys. J. Int.*, doi:10.1111/j.1365-246X.2008.03720.x.
- Lipman, P. W., H. J. Protska, and R. Christiansen (1972), Cenozoic volcanism and plate-tectonic evolution of the western United States I. Early and Middle Cenozoic, *Philosophical Transactions of the Royal Society London, Series A*, 271, 217-248. Lipman *et al.*, 1972
- Lobkis, O.I. and R.L. Weaver, (2003), Coda-wave interferometry in finite solids: Recovery of P-to-S conversion rates in an elastodynamic billiard, *Phys. Rev. Lett.*, 90(25), 254302, doi: 10.1103/PhysRevLett.90.254302.
- Lobkis, O.I. and R.L. Weaver (2001), On the emergence of the Green's function in the correlations of a diffuse field, *J. Acoust. Soc. Am.*, 110(6), 3011-3017.
- Madsen, J. K., D. J. Thorkelson, R. M. Friedman, and D. D. Marshall (2006), Cenozoic to Recent configuration in the Pacific Basin: Ridge subduction and slab window magmatism in western North America, *Geosphere*, 2, 11–34, doi:10.1130/GES00020.1.

- Margerin., L., M. Campillo, B.A. van Tiggelen, R. Hennino, (2009). Energy partition of seismic coda waves in layered media: theory and application to Pinyon Flats Observatory. *Geophys. J. Int.*, vol. 177, pp. 571-585, doi: 10.1111/j.1365-246X.2008.04068.x
- McKee, E.H., Duffield, W.A., and Stern, R.J., 1983, Late Miocene and early Pliocene basaltic rocks and their implications for crustal structure, northeastern California and south-central Oregon: *Geological Society of America Bulletin*, v. 94, p. 292–304, doi: 10.1130/0016-7606.
- McQuarrie, N. and B.P. Wernicke, (2005), An animated tectonic reconstruction of southwestern North America since 36 Ma, *Geosphere*, v.1, no. 3, pp. 147-172, doi: 10.1130/GES00016.1.
- Meigs, A., Scarberry, K., Grunder, A., Carlson, R., Ford, M.T., Fouch, M., Grove, T., Hart, W.K., Iademarco, M., Jordan, B., Milliard, J., Streck, M.J., Trench, D., and Weldon, R., (2009), Geological and geophysical perspectives on the magmatic and tectonic development, High Lava Plains and northwest Basin and Range, in O'Connor, J.E., Dorsey, R.J., and Madin, I.P., eds., *Volcanoes to Vineyards: Geologic Field Trips through the Dynamic Landscape of the Pacific Northwest: Geological Society of America Field Guide 15*, p. 435–470, doi: 10.1130/2009.fl d015(21).
- Meier, U, N.M. Shapiro, F. Brenguier, (2010), Detecting seasonal variations in seismic velocities within Los Angeles basin from correlations of ambient seismic noise, *Geophys. J. Int.*, 181, pp. 985-996, doi: 10.1111/j.1365-246X.2010.04550.x.
- Molina, I., H. Kumagai, J-L. Le Pennec, M.Hall (2004), Three-dimensional P-wave velocity structure of Tungurahua Volcano, Ecuador, *J. Volcanol. Geotherm. Res.*, vol. 147, 144-156.
- Moschetti, M.P., M.H. Ritzwoller, F-C. Lin, Y. Yang (2010a), Crustal shear wave velocity structure of the western United States inferred from ambient seismic noise and earthquake data. *J. Geophys. Res.* 115, B10306. doi:10.1029/2010JB007448.
- Moschetti, M.P., M.H. Ritzwoller, F-C. Lin, Y. Yang (2010b), Seismic evidence for widespread western-US deep-crustal deformation caused by extension. *Nature*, 464, doi: 10.138/nature08951.
- Moschetti, M.P., M.H. Ritzwoller, and N.M. Shapiro (2007), Surface wave tomography of the western United States from ambient seismic noise: Rayleigh wave group velocity maps, *Geochem., Geophys., Geosys.*, 8, Q08010, doi:10.1029/2007GC001655
- Nakahara, H. and L. Margerin (2011), Testing equipartition for S-wave coda using borehole records of local earthquakes, *Bull. Seism. Soc. Amer.*, vol.,101 (5), pp. 2243-2251, doi: 10.1785/0120100353.
- Nakamura, Y. (1989), A method for dynamic characteristics estimation of subsurface using microtremor on the ground surface, *Quarterly Report Railway Tech. Res. Inst.*, vol., 30 (1), pp. 25-33.

- Nishimura, T., N. Uchida, N., H. Sato, M. Ohtake, S. Tanake, and H. Hamaguchi (2000), Temporal changes of the crustal structure associated with the M6.1 earthquake on September 3, 1998 and the volcanic activity of mount Iwate, Japan, *Geophys. Res. Lett.*, 27(2), pp 269-272, doi: 10.1029/1999GL005439.
- Nogoshi, M. and T. Igarashi (1971), On the amplitude characteristics of microtremor (part 2), *Zisini*, 2, 24, pp. 26-40 (in Japanese with English abstract).
- Nur, A. (1973), Dilatancy, pore fluids, and premonitory variations of ts/tp travel times, *Bull. Seism. Soc. Amer.*, vol., 62, no. 5, pp. 1217-1222.
- Obrebski, M., Allen, R.M., Xue, M., Hung, S., (2010). Slab-plume interaction beneath the Pacific Northwest. *Geophys. Res. Lett.*, 10.1029/2010GL043489.
- Paul, A., M. Campillo, L. Margerin, E. Larose, A. Derode (2005), Empirical synthesis of time-asymmetrical Green functions from correlation of coda waves, *J. Geophys. Res.*, vol. 110(B9), B08302.
- Perton, M., F.J. Sánchez-Sesma, A. Rodriguez-Castellanos, M. Campillo, R.L. Weaver, (2009), Two perspectives on equipartition in diffuse elastic fields in three dimensions, *J. Acoust. Soc. Am.*, vol. 126(3), pp. 1125-1130, doi: 10.1121/1.3177262.
- Pierce, K.L., Morgan, L.A., Saltus, R.W., (2000), Yellowstone Plume Head: Postulated Tectonic Relations to the Vancouver Slab, Continental Boundaries, and Climate. *USGS Open-File Report 00-498*.
- Pierce, K.L. and L.A. Morgan (1992), The track of the Yellowstone hotspot: Volcanism, faulting, and uplift, in: Link, P.K., M.A. Kuntz, and L.B. Platt (eds.), Regional geology of eastern Idaho and western Wyoming, *Geol. Soc. Am. Memoir* 179.
- Porritt, R.W., R.M. Allen, D.V. Boyarko, and M.R. Brudzinski (2011), Investigation of Cascadia segmentation with ambient noise tomography. *Earth Planet. Sci. Lett.*, 309, 67-76.
- Poupinet, G., W.L. Ellsworth, J. Frechet (1984), Monitoring variations in the crust using earthquake doublets: An application to the Calaveras Fault, California, *J. Geophys. Res.*, 89 (B7), pp. 5719-5731,
- Ratdomopurbo, A. and G. Poupinet (1995), Monitoring a temporal change of seismic velocity in a volcano: application to the 1992 eruption of Mt. Merapi (Indonesia), *Geophys. Res. Lett.*, 22(7), pp. 775-778, doi: 10.1029/95GL00302.
- Rhie, J. & Romanowicz, B., (2004). Excitation of earth's incessant free oscillations by Atmosphere-Ocean-Seafloor coupling, *Nature*, 431, 552-556.
- Roux, P. (2009), Passive seismic imaging with directive ambient noise: application to surface waves and the San Andreas Fault in Parkfield, CA, *Geophys. J. Int.*, vol. 179, pp. 367-373, doi: 10.1111/j.1365-246X.2009.04282.x.

- Roux, P., K.G. Sabra, and W.A. Kuperman.(2005). Ambient noise cross correlation in free space: Theoretical approach. *J. Acoust. Soc. Am.*, vol. 117(1), pp. 79-84
- Sabra, K.G., P. Roux, P. Gerstoft, W. A. Kuperman, and M.C. Fehler, (2006), Extracting coherent coda arrivals from cross-correlations of long period seismic waves during the Mount St. Helens 2004 eruption, *Geophys. Res. Lett.*, 33, L06313, doi: 10.1029/2005GL025563.
- Sabra, G.G, P. Gerstoft, P. Roux, W. A. Kuperman, and M. C. Fehler. 2005. Extracting time-domain Green's function estimates from ambient seismic noise . *Geophysical Research Letters*, vol. 32, L03310, doi:10.1029/2004GL021862
- Saito, M. 1988. DISPER80: A subroutine package for the calculation of seismic normal-model solutions, in *Seismological Algorithms*, pp. 293-319, ed. Doornbos, D.J., Academic Press, New York.
- Sánchez-Sesma, F.J., M. Rodríguez, U. Iturrarán-Viveros, F. Luzón, M. Campillo, L. Margerin, A. García-Jerez, M. Suarez, M.A. Santoyo, A. Rodríguez-Castellanos (2011), A theory for microtremor H/V spectral ratio: application for a layered medium, *Geophys. J. Int.*, vol. 186, pp. 221-225, doi: 10.1111/j.1365-246X.2011.05064.x.
- Sánchez-Sesma, F.J., R. L. Weaver, H. Kawase, S. Matsushima, F. Luzón, M. Campillo (2011), *Bull. Seism. Soc. Amer.*, vol. 101 (4), pp. 1704-1709, doi: 10.1785/0120100196.
- Savov, I.P., W.P. Leeman, C-T Lee, S.B. Shirey (2009), Boron isotopic variations in NW USA rhyolites: Yellowstone, Snake River Plain, Eastern Oregon, *J. Volc. Geotherm. Res.*, doi:10.1016/j.jvolgeores.2009.03.008.
- Scarberry, K., Meigs, A., Grunder, A.L., (2009). Faulting in a propagating continental rift: Insight from the late Miocene structural development of the Abert Rim fault, southern Oregon, USA. *Tectonophys*, 10.1016/j.tecto.2009.09.025.
- Scholz, C. H., L.R. Sykes, Y.P. Aggarwal (1973), Earthquake prediction: A physical basis, *Science*, vol. 181, pp. 803-810.
- Sens-Schönfelder, C. and U. Wegler, (2006), Passive image interferometry and seasonal variations of seismic velocities at Merapi Volcano, Indonesia, *Geophys. Res. Lett.*, 33, L21302, doi: 10.1029/2006GL027797.
- SESAME European research project (2005), H/V measurements, in Guidelines for the implementation of the H/V spectral ratio technique on ambient vibrations – measurements, processing and interpretations, *SESAME European research project, deliverable D23.12,2005*, <http://www.geopsy.org/documentation/geopsy/hv.html>, Accessed: 3/21/2013
- Shapiro, N.M. M. Campillo, L. Stehly, and M.H. Ritzwoller (2005), High resolution surface wave tomography from ambient seismic noise, *Science*, 307(5715), 1615-1618, 11 March 2005.

- Shapiro, N.M., M. Campillo, L. Margerin, S. K. Singh, V. Kostoglodov, J. Pacheco, (2000). The energy partitioning and the diffusive character of the seismic coda, *Bull. Seism. Soc. Am.*, vol. 90 (3), pp. 655-665.
- Smith, R.B., M. Jordan, B. Steinberger, C.M. Puskas, J. Farrell, G.P. Waite, S. Husen, W. Chang, and R. O'Connell (2009), Geodynamics of the Yellowstone hotspot and mantle plume, Seismic and GPS imaging, kinematics, and mantle flow, *J. Volcanol. Geotherm. Res.* 188, 26-56.
- Smith, R.B., Braile, L.W. (1993), Topographic signature, space-time evolution, and physical properties of the Yellowstone-Snake River Plain volcanic system: the Yellowstone hotspot. In: Snoke, A.W., Steidtmann, J., Roberts, S.M. (Eds.), *Geology of Wyoming: Geological Survey of Wyoming Memoir No. 5.*, Wyoming State Geological Survey, Laramie, WY, pp. 694–754.
- Sneider, R. (2006), The theory of coda wave interferometry, *Pure Appl. Geophys.*, 163, pp. 455-473, doi: 10.1007/s00024-005-0026-6.
- Sneider, R. (2004), Extracting the Green's function from the correlation of coda waves: A derivation based on stationary phase, *Phys. Rev. E.*, 69, 046610 (8 pgs.), doi: 10.1103/PhysRevE.69.046610.
- Stachnik, J.C., K. Dueker, D.L. Schutt, and H. Yuan, (2008), Imaging Yellowstone plume-lithosphere interactions from inversion of ballistic and diffusive Rayleigh wave dispersion and crustal thickness data. *Geochem. Geophys. Geosys.*, G3 9(6), Q06004. doi:10.1029/2008GC001992.
- Tadeu, A., P. Santos, J. António (2001), Amplification of elastic waves due to a point source in the presence of complex surface topography, *Computers & Structures*, vol. 79 (18), pp. 1697-1712, doi: 10.1016/S0045-7949(01)00098-0.
- Takahahshi, E., Nakajima, K., Wright, T.L. (1998), Origin of the Columbia River basalts: Melting model of a heterogeneous mantle plume head. *Earth Planet. Sci. Lett.* 162, pp. 63–80.
- Tarantola, A. and Valette, B. 1982. Generalized non-linear problems solved using the least-squares criterion, *Rev. Geophys. Sp. Phys.*, 20, 219-232.
- Till, C.B., T.L. Grove, R.W. Carlson, J.M. Donnelly-Nolan, W.K. Hart, M.J. Fouch, L.S. Wagner, S. Hanson-Hedgecock, (2013), Depths and temperatures of <10.5 Ma Mantle Melting and the Lithosphere-Asthenosphere Boundary below southern Oregon and northern California, *Geochem. Geophys. Geosys.*, doi: 10.1002/ggge.20070.
- Trench, D., A. J. Meigs, and A. L. Grunder (2012), Termination of the northwestern Basin and Range province into a clockwise rotating region of transtension and volcanism, southeast Oregon, *Journal of Structural Geology*, 39, pp52-65.

- Venzke E, Wunderman R W, McClelland L, Simkin, T, Luhr, JF, Siebert L, Mayberry G, and Sennert S (eds.) (2002-2012). Tungurahua, Smithsonian / USGS Weekly Volcanic Activity Reports in Global Volcanism, 1968 to the Present. Smithsonian Institution, Global Volcanism Program Digital Information Series, GVP-4, <http://www.volcano.si.edu/world/volcano.cfm?vnum=1502-08=&volpage=weekly#Jan2010>, accessed: 1/9/2013 11:25 AM
- Wapenaar, K. (2004), Retrieving the elastodynamic Green's function of an arbitrary inhomogeneous medium by cross correlation, *Phys. Rev. Lett.*, 93, 254301-1.
- Wagner, L.S., D.W. Forsyth, M.J. Fouch, and D.E. James (2010), Detailed three-dimensional shear wave velocity structure of the northwestern United States from Rayleigh wave tomography. *Earth Planet. Sci. Lett.* 299, 273-284.
- Warren, L.M., J.A. Snoke, D.E. James (2008), S-wave velocity structure beneath the High Lava Plains, Oregon, from Rayleigh-wave dispersion inversion. *Earth Planet. Sci. Lett.* 274, 121-131
- Weaver, R. L. (2010) Equipartition and retrieval of Green's function, *Earthq. Sci.*, vol. 22, pp. 397-402, doi: 10.1007/s11589-010-0738-2
- Weaver, R.L. (1985) Diffuse elastic waves at a free surface., *J. Acoust. Soc Am.*, vol. 78, pp 131-136.
- Weaver, R. L., C. Hadziioannou, E. Larose, M. Campillo, (2011), On the precision of noise correlation interferometry, *Geophys. J. Int.*, 185, pp1384-1392, doi: 10.1111/j.1365-246X.2011.05015.x.
- Weaver, R.L. and O.I. Lobkis, (2004), Diffuse waves in open systems and the emergence of the Greens' function," *J. Acoust. Soc. Am.*, 116, 2731-4
- Weeraratne, D.S., Forsyth, D.W., Fischer, K.M., and Nyblade, A.A. 2003. Evidence for an upper mantle plume beneath the Tanzanian craton from Rayleigh wave tomography, *J. Geophys. Res.*, 108, 2427, doi: 688 10.1029/2002JB002273.
- Wells, R. E., and P. L. Heller (1988), The relative contribution of accretion, shear, and extension to Cenozoic tectonic rotation in the Pacific Northwest, *Geol. Soc. Amer. Bull.*, 100, 325-338.
- Wegler, U., and C. Sens-Schönfelder (2007), Fault zone monitoring with passive image interferometry, *Geophys. J. Int.*, 168, pp. 1029-1033, doi:10.1111/j.1365-246X.2006.03284.x.
- Wegler, U., B.-G. Lühr, R. Snieder, A. Ratdomopurbo (2006), Increase of shear wave velocity before the 1998 eruption of Merapi volcano (Indonesia), *Geophys. Res. Lett.*, 33, L09303, doi:10.1029/2006GL025928.

- Wernicke, B. P. (1992), Cenozoic extensional tectonics of the U.S. Cordillera, in *The Cordilleran orogen: Conterminous U.S.: Geology of North America*, edited by B. C. e. a. Burchfiel, pp. 553-581, Geological Society of America, Boulder, Colorado.
- Wu, R.S. (1985), Multiple scattering and energy transfer of seismic waves: separation of scattering effect from intrinsic attenuation, I, theoretical modeling, *Geophys. J. R. Astr. Soc.*, vol. 82, pp. 57-80.
- Xue, M., Allen, R.M., (2010). Mantle structure beneath the western U.S. and its implications for convection processes. *J. Geophys. Res.*, 10.1029/2008JB006079.
- Yang, Y., M.H. Ritzwoller, F.-C. Lin, M.P. Moschetti, and N.M. Shapiro (2008), Structure of the crust and uppermost mantle beneath the western United States revealed by ambient noise and earthquake tomography, *J. Geophys. Res.* 113, B12310, doi: 10.1029/2008JB005833.
- Yang, Y., M.H. Ritzwoller, A.L. Levshin, and N.M. Shapiro (2007), Ambient noise Rayleigh wave tomography across Europe, *Geophys. J. Int.*, 168(1), pages 259.
- Yang, Y., W. Shen and M.H. Ritzwoller, (2011) Surface wave tomography in a large-scale seismic array combining ambient noise and teleseismic earthquake data, *Earthquake Science*, 24, 55-64.